Light Transport in Inhomogeneous Scattering Media: Perturbation Theory and Biomedical Application

Vom Fachbereich Physik der Universität Hannover

zur Erlangung des Grades

Doktor der Naturwissenschaften

Dr. rer. nat.

genehmigte Dissertation

von

Dipl. Phys. Martin Ostermeyer

geboren am 15.3.1965 in Hannover

1999

Zusammenfassung der Arbeit

Die biomedizinische Optik hat sich in den letzten Jahren stürmisch entwickelt. Im für viele diagnostische wie auch therapeutische Anwendungen besonders interessanten nahinfraroten Spektralbereich wird die Lichtausbreitung in biologischem Gewebe von Streuung dominiert und kann als ein Diffusionsprozeß von Photonen beschrieben werden. Während die Theorie für homogene Modellsysteme inzwischen gut verstanden ist, stellt die Optik in den aus medizinischer Sicht besonders relevanten inhomogenen Medien gegenwärtig ein Forschungsschwerpunkt im Bereich der biomedizinischen Optik dar. Als Anwendungen sind neben der Detektion und Therapie von Tumoren insbesondere die tomographische Darstellung physiologischer Parameter, wie etwa der Blut– und Zelloxygenierung, zu nennen.

In dieser Arbeit wird eine umfassende Theorie der Lichtausbreitung in inhomogenen stark streuenden Medien entwickelt. Sie beschreibt kontinuierlich eingestrahltes Licht, wie auch die Ausbreitung von sogenannten diffusen Photonen–Dichtewellen bei amplitudenmodulierter Einstrahlung. Es werden zwei komplementäre störungstheoretische Ansätze verfolgt. Die erste Methode beruht auf der Lösung der differentiellen Form der Strahlungs–Diffusionsgleichung für ein sphärisches Objekt. Es werden grundlegende Eigenschaften von kleinen streuenden und absorbierenden Störungen diskutiert und deren Einfluß auf Messungen untersucht. Die zweite Methode basiert auf der integralen Formulierung der Diffusionstheorie. Zur Beschreibung von Inhomogenitäten wird dazu der Formalismus der 'virtuellen Quellen' eingeführt, die mittels der Greenschen Funktion des ungestörten Mediums auf das Lichtfeld wirken. Mit der formalen Lösung läßt sich erstmals ein detailliertes und zugleich physikalisch intuitives Verständnis der Wirkung von makroskopischen Störungen erlangen. Die eigentliche Lösung ist jedoch ein iterativer Prozeß. Mit der dazu entwickelten numerischen Implementation lassen sich nun Gewebe mit Objekten beliebig komplexer Geometrie flexibel und schnell modellieren.

Abschließend wird die optische Detektion von Hirnblutungen bei Unfallopfern untersucht. Da eine dünne Schicht klarer Gehirnflüssigkeit zwischen Schädel und Gehirn die Anwendung der Diffusionstheorie nicht zuläßt, wird die Lichtausbreitung hier mit Monte Carlo Simulationen modelliert. Die Ergebnisse zeigen, daß Blutungen trotz unterschiedlicher anatomischer Verhältnisse durch Absorptionsmessungen bei Optodenabständen größer als 4 cm sicher nachweisbar sein sollten. Daraufhin wurde ein tragbarer optischer Sensor für den Einsatz direkt am Unfallort entwickelt. Die hohe Sensitivität und der große Dynamikbereich erlauben bei gesunden Probanden einen Optodenabstand von 5,5 cm, bei dem die erfolgreiche Detektion von schädelnahen Hämatomen bei Unfallopfern sicher scheint. Ein klinischer Test steht unmittelbar bevor.

Schlagwörter: Gewebeoptik, Störungstheorie, Hirnblutungen

Abstract

Biomedical optics has developed rapidly in recent years. In the near infrared spectral range, which is of special interest for diagnostic as well as therapeutic applications, light propagation in biological tissues is dominated by scattering, and can be described as a diffusion process of photons. While by now the theory for homogeneous model systems is well understood, the optics of the medically most relevant inhomogeneous media is currently an active area of biomedical research. Prominent applications are the therapy and detection of tumors and the tomographic reconstruction of physiological parameters like blood and cell oxygenation.

In this work a comprehensive theory of light propagation in inhomogeneous strongly scattering media is developed. It describes the propagation of continuous light as well as diffuse photon density waves due to amplitude modulated illumination. Two complementary approaches are used. The first method is based on a solution of the differential form of the photon diffusion equation for a spherical object. Basic properties of small absorbing and scattering perturbations and their influence on measurements are investigated. The second method utilizes the integral formulation of diffusion theory. To describe inhomogeneities the concept of virtual sources is introduced. The virtual sources affect the light field through the Green's functions of the unperturbed medium. With the formal solution it is possible for the first time to gain a detailed and at the same time physically intuitive understanding of the effects of macroscopic perturbations. The actual solution, however, is an iterative process. With the numerical implementation it is now possible to rapidly model tissues with inclusions of arbitrary complexity.

Finally the optical detection of traumatic brain hematoma in accident victims is investigated. The light propagation is modeled with Monte Carlo simulations because a clear layer of cerebrospinal fluid between skull and brain prevents the use of diffusion theory. The results show that despite anatomical variations brain hematomas should be securely detectable with absorption measurements using optode separations greater than 4 cm. Based on these results a portable optical probe for application directly at the accident site is developed. The high sensitivity and dynamic range allow for an optode separation of 5.5 cm on healthy volunteers. For this separation the successful detection of shallow hematomas seems certain. A clinical test is impendent.

Key words: tissue optics, perturbation theory, brain hematoma

Acknowledgements

Beop-Min Kim, PhD for too much to mention, but especially for a rewarding collaboration on the prostate project and the exposure to the Korean cuisine.

Prof. Alexander Oraevsky, PhD for a fruitful collaboration and for many discussions about the russian and american way of life. The excitement with which he approaches science and life in general was always inspiring.

David Levy, MD, who has greatly inspired my interest in medical issues. In M. D. Andersons pathology he showed me that freshly excised organs are not only yucky, but in fact rather interesting. I am still grateful that he didn't try the optical prostrate measurements on me, but rather took me to mountain bike tours.

Jon Schwartz for his constant support in the lab. He is one of the most polite and helpful persons I know.

Shao Lin, Rinat Esenaliev, PhD, Jeff Ellards, and Tom Rodriguez for keeping up the spirit in the lab.

David Boas, PhD and Maureen O'Leary, PhD for many very fruitful discussions about tissue optics, their great hospitality, and a terrific week of nerdy software development.

Volkart Abraham for 'discovering' me on a SPIE meeting.

Dr. Holger Lubatschowski for recruiting me on that same meeting. He involved me in the hematoma project and supported me in every possible way. He has my highest respect for leading the 'medi' group in a unique way: I have never before experienced such an atmosphere of mutual trust.

Christoph Schmitz and Stefan Lohmann, the ultimate couple, for the continued very open discussion of the really important physical issues in life. Thanks for all your support, scientifically and socially, and here I only have to exclude the repeated recitation of Helge Schneider songs.

Sebastian Bartel for his help with the Monte Carlo simulations. It was a pleasure to work on the polarization project with a student as brilliant as him. Special thanks for proving that it is possible to be fussier than I am.

Gerd Hörbe for being himself and for remarkable acoustic effects, Dr. Andreas Olmes for the proof that project management really does work, Guido Wokurka for strategic advice and good friendship, and Carsten Ziolek for some nice electronic sparrings.

Mrs. Krämer and Mrs. Griese for smoothing the way and generally for putting up with me.

All members of the institute for the pleasant atmosphere and a thousand little and not so little things, but especially Uwe Oberheide, Michael Zacher, Thomas Hantzko, Thomas Kleine–Besten, Christine Ruff, Maike Busemann, Martin Brand, Martin Raible, Alexander Heisterkamp, Stefan Hiller, Kai Bongs, Dr. Rudi Gaul, Mr. Heidekrüger, and Matthias Scholz.

Prof. Dr. Weinrich for initiating and fostering the hematoma project.

Dr. Eckhard Ludwig and Dr. Stefan Zander, who taught me some basics of neurology and spent much of their free time with me on the hematoma project. Special thanks to Dr. Zander for proof reading the medical part of this thesis and to Dr. Stefan Randzio for providing the CT scans.

My wife Heidrun Kupka for unconditional support and a great deal of endurance during some tough times in Houston as well as in Hannover.

My family for their back up and especially my parents and my brother Eckhard for providing a firm home base during our stay in the US.

Navigating the Electronic Version of this Document

This document is available in electronic form as a PDF file. One of the advantages of this format for online viewing is the availability of hyperlinks, which allow for elegant navigation through the document.

In order to help the reader to recognize hyperlinks they are often emphasized, for example by using special fonts or colors, understriking, or bounding boxes. While this is convenient when reading the electronic document, all of these methods have the disadvantage that they yield unsatisfying results if the document is printed. I therefore chose *not* to emphasize hyperlinks.

But then, how can a reader recognize a hyperlink? As a rule, whenever the reader feels it would be convenient to have a hyperlink, there usually is one. Specifically, hyperlinks are available in the following contexts:

- References in the text or in the table of contents to chapters or sections

- References in the text to figures, tables, and equations

- References to specific pages

- Citations are hyperlinks to the bibliography

- Back references from the bibliography to all citations in the text

Generally the number associated with the linked target (e.g. page number, equation number) is the active element of the hyperlink, except for the table of contents, where the title of the chapter or section is the active element. Depending on the program used for viewing, a change of the cursor indicates an active hyperlink.

Contents

Chapter 1

Introduction

During the last years the use of light, and especially lasers, in medicine and biology has increased significantly. Medical lasers are now available with a wide range of parameters, be it wavelength, power, or pulse length. They continually become smaller and more economic and are used for an ever growing variety of applications, ranging from precise surgical ablation with ultrashort pulses over photodynamic therapy of tumors to the spectroscopic imaging of metabolic information.

The success of these applications ultimately depends on the understanding of the interaction of light with biological tissues. Consequently considerable research efforts have been devoted to this complex field, and by now biomedical optics has established itself as a scientific discipline of its own right. A central task of biomedical optics is to describe how light propagates in tissue. This is the prerequisite for any further analysis of the thermal, mechanical, or photo-chemical processes of laser tissue interactions in therapeutic applications, and it naturally is the main point of interest in diagnostic applications. Biomedical optics is complicated by the fact that in tissue light is not only absorbed and diffracted, but generally also strongly scattered. The random nature of scattering causes light to quickly loose its original direction. This leads to a broad
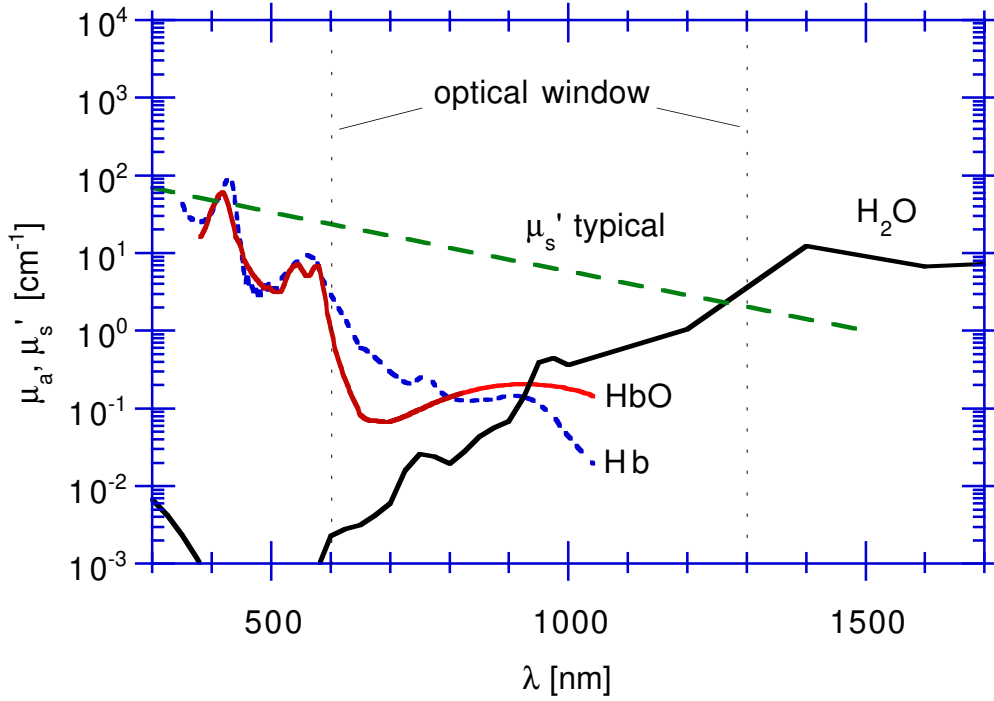
Figure 1.1:   In the visible and near infrared spectral range water [1] and hemoglobin are the dominant absorbers in biological tissues. The curves for oxy-hemoglobin (HbO) and deoxy-hemoglobin (Hb) [2] are scaled for 3% blood volume and 45% hematocrit, which are typical values for tissue. Also shown is the typical wavelength dependence of the reduced scattering coefficient μ'_s, which is a measure for the macroscopic effects of the forward directed small angle scattering in tissue (a precise definition will be given in section 2.3). Note that the absolute value of μ'_s can differ by about an order of magnitude, depending on the tissue type.

distribution even if the light enters the tissue as a collimated or focused beam. Therefore conventional ray optics is not applicable to tissues. Instead it is appropriate to model the light propagation as a transport process of radiation.

The details of the light transport depend on the relative strength of absorption and scattering. In tissue this varies strongly with the wavelength. Figure 1.1 shows the spectrum of the absorption coefficient μ_a for the two most important chromophores in tissue, hemoglobin and water. Both have a low absorption in

the near infrared spectral range, especially between about 600 nm and 1300 nm. This region is commonly referred to as the 'optical window', because here light can penetrate deep into the tissue. Clearly this is very convenient for both therapeutic and diagnostic applications.

The figure also shows that in the optical window the scattering dominates the absorption. On one hand this is a serious drawback because the strong scattering prevents focusing of light into the tissue and effectively renders conventional transillumination imaging impossible. On the other hand there is also an advantage: In the strong scattering regime light propagation can be described with a diffusion theory. The simplicity of this description has led to various applications in biomedical optics. Unfortunately simple analytic solutions for diffusion theory exist only for homogeneous media.

However, biological tissues are optically inhomogeneous not only on the microscopic scale, which is the cause for the light scattering, but also on a mesoscopic and macroscopic scale. The encountered structures range from agglomerations of organs on a centimeter scale, over cellular structures like blood vessels in the surrounding tissue on a millimeter scale, to cells in their extracellular fluid on the scale of a few micrometers. Especially the chromophores are not evenly distributed. Hemoglobin is the dominant absorber in the visible and near infrared spectral range. It is well known that blood is distributed in a fractal tree of vessels with diameters ranging from about 10 μm for capillaries up to almost a centimeter for big veins.

To some extend the averaging nature of diffuse light transport allows to neglect the smaller inhomogeneities and to model tissue as a homogeneous medium with the average optical properties of the real tissue. Larger inhomogeneities, however, are the main obstacle for an accurate theoretical description of light propagation in tissues. At the same time they are often the focus of interest in biomedical applications. An important example are tumors. For their treat-

ment it is necessary to predict the light distribution in and around the tumor in order to plan the dosimetry. This type of calculation is known as forward modeling, since the distribution of the light field is calculated from the known (or assumed) distribution of optical properties in the tissue. In order to detect tumors it is necessary to know how different optical properties inside the medium affect the measurements on the outside. The actual reconstruction of the optical properties mapping is known as the inverse problem. However, inverse algorithms are always based on forward models and depend on their accuracy. It is thus apparent that an accurate forward theory is of the highest practical interest for both diagnostic and therapeutic applications.

The aim of this work is to give a comprehensive account of the forward theory for the propagation of steady state and amplitude modulated light in inhomogeneous tissues.

After a brief summary of transport and diffusion theory for homogeneous media in chapter 2 the following chapters discuss different aspects of inhomogeneous tissue optics.

In chapter 3 an analytic multipole solution of the differential diffusion theory for a spherical inclusion is used to formulate a perturbation theory for small inhomogeneities. It is used to investigate the sensitivity of reflection mode measurements to the presence of perturbations. Thereby the concept of the sensitivity map for absorbing perturbations is extended to scattering perturbations, the differences are discussed.

In chapter 4 we develop a new perturbation approach that is based on the integral formulation of the diffusion theory. The concept of virtual sources is introduced. This approach has several advantages. Extended objects of arbitrary geometry can be modeled. An iteration scheme allows to account for the inherent nonlinearity of the problem and thus allows to model situations

with strong perturbations, were the usual first order approximations fail. Most important, the virtual source formalism for the first time provides an intuitive understanding of light propagation in media with scattering perturbations.

Chapter 5 discusses the implementation of the virtual source formalism as a numerical algorithm. This yields valuable information for the accuracy of forward as well as inverse algorithms. The resulting software package is a versatile tool for the rapid three dimensional modeling of tissues with inclusions of arbitrary complexity.

In chapter 6 we discuss a practical biomedical application: the optical detection of brain hematomas. In this case the perturbation concepts we have developed so far cannot be applied, because diffusion theory fails in the non–scattering layer of cerebrospinal fluid between skull and brain. Nevertheless the use of Monte Carlo simulations as a numerical forward model allows to determine the appropriate measurement modality. Based on these results a prototype of the optical hematoma detector is build and tested.

Chapter 2

Light Propagation in Biological Tissues

In this work the propagation of light in biological tissues is approximated with transport theory, also called radiative transfer theory. This theory simplifies the light propagation as well as the description of the medium light interacts with.

It is possible to include coherence and polarization effects in transport theory [3]. We have shown that polarization causes fascinating effects with potential diagnostic applications [4, 5] and are currently refining the theoretical description [6]. However, for this work we restrict ourselves to *scalar* transport theory which neglects the wave nature of light completely (except for a wavelength dependence of the optical properties of the tissue) and thus treats light as a stream of uncorrelated, unpolarized, point-like photons. This approximation allows to use the same tools that were developed for other particle transport processes like kinetic gas theory and neutron scattering in nuclear reactor theory. Although the underlying particle picture of transport theory is naturally discrete and discontinuous, its basic equation, the radiative transfer equation

(RTE), is a macroscopic, continuous energy balance equation that averages over many scattering events.

A consequence of this macroscopic and averaging nature of the RTE is that the scattering medium can be described with only four averaged bulk optical properties: the absorption coefficient μ_a, the scattering coefficient μ_s, the refractive index n, and the scattering phase function $p(\hat{s}, \hat{s}')$, which accounts for the angle dependence of a scattering process between the incoming and outgoing directions. Thus the scattering coefficient and the scattering phase function account for the microscopic inhomogeneities that cause the scattering, but macroscopically the medium is considered to be homogeneous and continuous.

For some simple scattering media this is a very good description. An important example are suspensions of latex or glass spheres or of lipid emulsions with spherical droplets. They are used routinely as optical phantoms to mimic biological tissues in the laboratory. For these media the bulk optical properties can be calculated with Mie theory [7]. This is a satisfactory situation since the macroscopic effects of light transport can be *deduced* from the microscopic properties of the medium with a chain of rigorous theories that are ultimately based on Maxwell's equations.

Unfortunately, light propagation in biological tissues cannot be treated that rigorously, because they are too complex. Beuthan *et al* [8] attempted to calculate the scattering properties of cells using Fraunhofer diffraction of the measured phase profile as well as Rayleigh-Gans scattering of cell components. These calculations underestimated typical real scattering coefficients of tissue by about an order of magnitude. This is not surprising in light of a study by Schmitt *et al* [9], who have recently shown that on the cellular and sub cellular scale the spatial variation of the refractive index in tissues is of turbulent nature. Thus the basic optical properties cannot be deduced from the phys-

iologically most interesting microscopic makeup of the tissue, but have to be *measured* as bulk quantities. In this sense radiative transfer theory for tissues is essentially a heuristic theory.

In the introduction we have pointed out that biological tissues are inhomogeneous on a wide range of length scales. Thus the question arises what scale we should use to define the 'macroscopic' optical properties? At the same time this determines the resolution of the description, i.e. the minimal extension we can attribute to an inhomogeneity. The answer is a rather practical one: It depends on the volume our experimental setup samples and on the spatial resolution and accuracy we want to (and can principally) achieve.

In this work we are interested in diagnostic applications in the near infrared optical window, where light can penetrate deep into the tissue. At 800 nm the $1/e$–penetration depth is about 4 mm. Reasonable diagnostic measurements are limited to about 5 to 8 cm source detector separation, the resolution limit is on the order of some millimeters. Typical for measuring bulk optical properties *in vivo* are about 2 cm separation, the sampled tissue volume is then on the order of a cubic centimeter. Considering this, the near infrared *in vivo* optical parameters in tissues are practically defined only down to a length scale of some millimeters. This means that variations below this length scale are averaged out and we can treat a medium with such variations as macroscopically homogeneous in the practical sense of transport theory. Consequently, variations above this length scale should be considered as inhomogeneities.

After this careful definition of homogeneous and inhomogeneous biological media we can now turn to a discussion of the light propagation in such media. In this chapter we first give a summary of transport theory and then outline the derivation of the homogeneous diffusion theory. We discuss the basic solutions for infinite and semi–infinite media. This lays the foundation for the discussion of inhomogeneous light propagation in the following chapters.

2.1 Radiative Transfer Theory

The fundamental quantity of radiation transfer is the radiance $L(\mathbf{r}, \hat{\mathbf{s}}, t)$, also referred to as specific intensity. Radiance is the power density that reaches the position $\mathbf{r}$ from a direction $\hat{\mathbf{s}}$ at time t, its units are power per area per solid angle $[\mathrm{W/sr/cm^2}]$.

Light transport can be described by the radiative transfer equation(RTE):

$$\frac{1}{c}\frac{\partial}{\partial t}L(\mathbf{r}, t, \hat{\mathbf{s}}) = -\hat{\mathbf{s}}\cdot\boldsymbol{\nabla}L(\mathbf{r}, t, \hat{\mathbf{s}}) - \mu_t L(\mathbf{r}, t, \hat{\mathbf{s}}) + \mu_s \int d\hat{\mathbf{s}}' p(\hat{\mathbf{s}}, \hat{\mathbf{s}}') L(\mathbf{r}, t, \hat{\mathbf{s}}') + S(\mathbf{r}, t, \hat{\mathbf{s}}).$$

$$(2.1)$$

Here c is the speed of light in the medium and $\mu_t = \mu_s + \mu_a$ is the total interaction coefficient, where μ_s and μ_a are the scattering and absorption coefficient. $S(\mathbf{r}, t, \hat{\mathbf{s}})$ is the source distribution. $p(\hat{\mathbf{s}}, \hat{\mathbf{s}}')$ is the normalized phase function, which represents the probability of scattering from direction $\hat{\mathbf{s}}$ into direction $\hat{\mathbf{s}}'$, or vice versa.

The radiative transfer equation is an energy balance equation [10, 3]. This can be seen best if the whole equation is integrated over a small volume dV. Then the change of the radiance on the left hand side is the net sum of losses and gains on the right hand side of the equation. They are from left to right: loss due to flow out of the volume, loss due to absorption and due to scattering out of the direction $\hat{\mathbf{s}}$, gain due to scattering from all other directions $\hat{\mathbf{s}}'$ into direction $\hat{\mathbf{s}}$, and gain due to light sources in the volume.

The phase function p is a quantity that is directly related to the microscopic structure of the medium. For simple scatterers it can be calculated e.g. with Mie theory [7]. For biological tissues, however, a heuristic model has to be used. Jacques *et al* [11] have shown experimentally that the Henyey–Greenstein phase function, which was originally proposed for light scattering in interstellar

clouds [12], describes scattering in biological tissues adequately. The Henyey–Greenstein phase function is defined as

$$p_{HG}(\hat{\mathbf{s}}' \cdot \hat{\mathbf{s}}) = p_{HG}(\cos\theta) = \frac{1 - g^2}{4\pi(1 + g^2 - 2g\cos\theta)} \tag{2.2}$$

where θ is the scattering angle. The mean cosine of the scattering angle

$$g = \int d\hat{\mathbf{s}} \; \cos\theta \, p_{HG}(\cos\theta) \tag{2.3}$$

is in turn the only parameter that defines the Henyey–Greenstein phase function. Note that the phase function is normalized, i.e. $\int d\hat{\mathbf{s}} \, p_{HG}(\hat{\mathbf{s}}' \cdot \hat{\mathbf{s}}) = 1$.

Analytical solutions to the RTE are only known for the simplest geometries and are of little practical use [3, 13]. Numerically, the RTE can be solved with discrete ordinate methods, where not only the spatial coordinates and the time, but also the solid angle are discretized [13]. However, in this work we will specialize on two methods that are widely used in biomedical optics to obtain approximate solutions of the RTE: diffusion theory and Monte Carlo simulation. Both are complimentary in several ways.

2.2 Monte Carlo Simulation

Monte Carlo simulation is a statistical method to obtain approximate solutions of the RTE. The basic idea is to simulate the propagation of single photons as close to the physical process as possible. The distance between consecutive scattering events, the scattering angle at each scattering event, and the pathlength before the photon is absorbed are determined by random variables. The sampling of the random variables is thereby chosen in such a way that for many scattering events the optical properties are on average reproduced. The light distribution in the medium can be obtained as a histogram of absorbed photons. Also, the path histories of photons can be analyzed.

One advantage of the method is the great flexibility. It is for example easy to model inhomogeneities, including clear regions, or Fresnel reflection at refractive index mismatches. The other advantage is that Monte Carlo simulations yield exact solutions of the RTE in the sense that no approximations beyond those of radiative transport theory are made. The drawback is that the solution is only a statistical one and that the method is slow. Often a large number of simulated photons is required to give a sufficiently low variance. The reason is that the statistical error of the results is inverse proportional to the square of the number of simulated photons. Depending on the optical properties of the medium it takes about a day to simulate 10^6 photon packets on workstations, with supercomputers 10^8 are tractable, which gives about a tenfold decrease in the statistical errors. This is still many orders of magnitude below the number of photons typical light sources emit in a second. Because of the high computational costs Monte Carlo simulations are usually used only if diffusion theory cannot be applied. We will encounter such a case in chapter 6, where the diffusion approximation fails because of a clear layer of cerebrospinal fluid between skull and brain.

The Monte Carlo code we use is based on the MCML–code by Wang and Jacques [14, 15], which simulates light propagation in multi–layered media. To reduce the computational cost it implements a variance reduction technique [16] and uses so called weighted photon packets instead of single photons. A photon packet is started with a certain photon weight. While propagating the packet through the medium a fraction of the weight is dropped at each interaction site according to the ratio of absorption and scattering. The dropped weight is stored in a collection grid for histogramming the light distribution. The advantage is that on average the photon packages penetrate deeper into the medium as single photons before they are terminated, and this improves the statistic away from the source. We rewrote the code for parallel processing on a Cray T3E supercomputer and added time resolved collection of the

photons. We also store the individual photon paths in order to analyze the light propagation specifically between a source and a detector. In chapter 6 we use the resulting sensitivity maps to analyze the measurement of brain hematomas.

2.3   Diffusion Theory

The main advantage of diffusion theory is that it is much simpler than radiative transfer theory. Analytic solutions can be obtained for practically relevant cases, see section 3.1. The Green's function formalism can be used to develop a general perturbation theory (see section 4). Even numerically the diffusion equation is much more tractable than the RTE. However, diffusion theory is only an approximation to the radiative transfer theory. It describes light transport accurately only in the strong scattering regime where the scattering coefficient is much larger than the absorption coefficient ($\mu_a \ll (1-g)\mu_s$). It also fails near sources and boundaries and it cannot describe clear regions in the medium as we will see in chapter 6.

In the strong scattering regime photons survive many scattering events before they are absorbed. Scattering is a random process, and after many scattering events the direction of a photon has lost any correlation to the direction it was launched in. The angular distribution of the radiance is then almost isotropic and can be described by the first few moments of a multipole expansion. This is known as the P_N or spherical harmonic method [13, 17, 18]. We will outline the general procedure only briefly and then proceed with a simplified method to derive the diffusion equation.

For the P_N approximation the radiance, the source distribution, and the phase function are expanded in a series of spherical harmonic functions $Y_{l,m}(\hat{\mathbf{s}})$ and

inserted into the RTE. The RTE is then multiplied with $Y_{l',m'}^{*}(\hat{\mathbf{s}})$ and inte-grated over $\hat{\mathbf{s}}$. Using the orthogonality relations for the spherical harmonic functions the RTE is transformed into a set of $(2N+1)^2$ coupled first order differential equations. Truncation of the expansion at the Nth moment results in the P_N approximation. The P_1 approximation is also known as the diffusion approximation and the resulting four coupled equations can be combined in the diffusion equation.

Instead of dealing with spherical harmonics we use the integral definition of the first two angular moments for radiance, source distribution, and phase function. The fluence rate ϕ is the isotropic part of the radiance and is obtained by integration of the radiance over the whole solid angle

$$\phi(\mathbf{r},t) = \int_{4\pi} d\hat{\mathbf{s}} \; L(\mathbf{r},t,\hat{\mathbf{s}}). \tag{2.4}$$

The net flux vector $\mathbf{J}$

$$\mathbf{J}(\mathbf{r},t) = \int_{4\pi} d\hat{\mathbf{s}} \; L(\mathbf{r},t,\hat{\mathbf{s}}) \, \hat{\mathbf{s}} \tag{2.5}$$

is the first angular moment of the radiance. Both have units of $[\mathrm{W/cm^2}]$. In the diffusion approximation the expansion is aborted here and the radiance is represented as

$$L(\mathbf{r},t,\hat{\mathbf{s}}) = \frac{1}{4\pi}\phi(\mathbf{r},t) + \frac{3}{4\pi}\mathbf{J}(\mathbf{r},t) \cdot \hat{\mathbf{s}}. \tag{2.6}$$

The first moments of the source distribution S_0 and S_1 are defined in the same way as fluence rate and net flux. The phase function, however, is normalized, therefore

$$p_0 = \int_{4\pi} d\hat{\mathbf{s}} \; p(\hat{\mathbf{s}},\hat{\mathbf{s}}') \; \equiv 1, \tag{2.7}$$

and the first moment is the average cosine g

$$p_1 = \int_{4\pi} d\hat{\mathbf{s}} \; p(\hat{\mathbf{s}},\hat{\mathbf{s}}') \, \hat{\mathbf{s}} \; \equiv g. \tag{2.8}$$

Equation (2.6) is now inserted in the radiative transfer equation (2.1). Integrating the whole equation over $\hat{\mathbf{s}}$ gives

$$\frac{1}{c}\frac{\partial}{\partial t}\phi(\mathbf{r},t) \;+\; \mu_a\phi(\mathbf{r},t) \;+\; \boldsymbol{\nabla}\mathbf{J}(\mathbf{r},t) \;=\; S_0(\mathbf{r},t), \tag{2.9}$$

while multiplying the equation with $\hat{\mathbf{s}}$ and then integrating over $\hat{\mathbf{s}}$ gives

$$\frac{1}{c}\frac{\partial}{\partial t}\mathbf{J}(\mathbf{r},t) \;+\; (\mu_a + \mu_s')\mathbf{J}(\mathbf{r},t) \;+\; \frac{1}{3}\boldsymbol{\nabla}\phi(\mathbf{r},t) \;=\; \mathbf{S}_1(\mathbf{r},t), \tag{2.10}$$

where

$$\mu_s' = \mu_s(1-g) \tag{2.11}$$

is defined as the *reduced scattering coefficient.* Combining Eqs. (2.9, 2.10) and defining $\tilde{D} = 1/(\mu_a + \mu_s')$ we obtain

$$\frac{1}{c}\frac{\partial}{\partial t}\phi(\mathbf{r},t) + \mu_a\phi(\mathbf{r},t) - \boldsymbol{\nabla}(\tilde{D}\boldsymbol{\nabla}\phi(\mathbf{r},t)) - S_0(\mathbf{r},t) \;= \tag{2.12}$$
$$-3\boldsymbol{\nabla}(\tilde{D}\mathbf{S}_1(\mathbf{r},t)) + \frac{3\tilde{D}}{c}\left(\frac{\partial}{\partial t}S_0(\mathbf{r},t) - \mu_a\frac{\partial}{\partial t}\phi(\mathbf{r},t) - \frac{1}{c}\frac{\partial^2}{\partial t^2}\phi(\mathbf{r},t)\right).$$

The terms on the right hand side are all dropped. The term with the dipole moment of the source S_1 is omitted because it is of little practical use. While many applications involve collimated light sources, the dipole moment is not sufficient to describe this directionality. Instead, a collimated source is mimicked with a point source that is placed one reduced scattering length $1/\mu_s'$ away from the actual collimated source (see section 2.3.2.2). The remaining terms can be neglected because they are usually small. To see this we fourier transform the equation to change from time domain to frequency domain. The time derivatives are thus replaced by $-i\omega$, where $f = \omega/(2\pi)$ is the modulation frequency of an amplitude modulated source. We get a common factor $3\tilde{D}\omega/c$ in the remaining terms. For typical reduced scattering coefficients of tissue in the near infrared spectral range $\mu_s' \approx 10$ cm^{-1} this factor is small if $f \ll 3$ GHz and the remaining terms can therefore be neglected.

Before we write down the diffusion equation we have to address a rather peculiar issue. The coefficient $\tilde{D} = 1/(3(\mu_a + \mu_s'))$ in Eqs. (2.9–2.12) has long

been known as the diffusion coefficient. Because diffusion theory is limited to strongly scattering media, i.e. $\mu_a \ll \mu_s'$, the absorption coefficient was sometimes dropped, but this was thought to be a further approximation to diffusion theory. However, Furutsu *et al* [19] and Yamada [20] have derived the diffusion equation with a diffusion coefficient which is independent of absorption:

$$D = \frac{1}{3\mu_s'}. \tag{2.13}$$

Recently, this has been verified with Monte Carlo simulations [21] and also experimentally [22]. We therefore adopt Eq. (2.13) as the definition of the diffusion coefficient. While this change in the definition of D will have only small quantitative effects for most experiments if $\mu_a \ll \mu_s'$, it has qualitative consequences for the theory of absorbing and scattering inhomogeneities as we will see in section 4.4.

Up to now we have only implicitly assumed that the optical properties can vary spatially. Now we write the spatial dependence explicitly and finally get the diffusion equation for inhomogeneous media in the frequency domain

$$-\boldsymbol{\nabla}D(\mathbf{r})\cdot\boldsymbol{\nabla}\phi(\mathbf{r},\omega) - D(\mathbf{r})\nabla^2\phi(\mathbf{r},\omega) + \mu_a(\mathbf{r})\,\phi(\mathbf{r},\omega) - \frac{i\omega}{c(\mathbf{r})}\,\phi(\mathbf{r},\omega) = S_0(\mathbf{r},\omega). \tag{2.14}$$

From Eq. (2.10) we also get Fick's law

$$\mathbf{J}(\mathbf{r},\omega) = -D(\mathbf{r})\,\boldsymbol{\nabla}\phi(\mathbf{r},\omega). \tag{2.15}$$

We will discuss the diffusion equation for inhomogeneous media extensively in chapter 4 and show that the first term in Eq. (2.14) is responsible for the dipole characteristic of a scattering perturbation.

For the rest of this chapter we will concentrate on a homogeneous medium, where the optical properties and especially the diffusion coefficient $D = 1/(3\mu_s')$ are constant. Then the first term in Eq. (2.14) vanishes and the resulting diffusion equation for homogeneous media can be brought in the form of a

Helmholtz equation

$$\left(\nabla^2 + k^2\right)\phi(\mathbf{r}, \omega) = -3\mu'_s\, S_0(\mathbf{r}, \omega), \tag{2.16}$$

where k is the wave vector with the definition

$$k^2 = -3\mu'_s\left(\mu_a - \frac{i\omega}{c}\right). \tag{2.17}$$

2.3.1 Diffuse Photon Density Waves

In an infinite medium the Green's function for the Helmholtz equation, i.e. the solution of the equation $\left(\nabla^2 + k^2\right)\phi(\mathbf{r}, \omega) = -\delta(\mathbf{r} - \mathbf{r}_s)$ is

$$G(|\mathbf{r} - \mathbf{r}_s|, \omega) = \frac{1}{4\pi|\mathbf{r} - \mathbf{r}_s|}e^{ik|\mathbf{r} - \mathbf{r}_s|}, \tag{2.18}$$

where $\mathbf{r}_s$ is the position of a mathematical point source. Since in the diffusion equation the source term is scaled by $3\mu'_s = 1/D$ it is practical to define the impulse response to a physical point source for the diffusion equation as

$$\hat{G}(|\mathbf{r} - \mathbf{r}_s|, \omega) = 3\mu'_s G(|\mathbf{r} - \mathbf{r}_s|, \omega). \tag{2.19}$$

In the following we will mostly use $\hat{G}$ instead of G because it simplifies the formulas. Note that $\hat{G}$ has units of $[\text{cm}^{-1}]$.

The nature of the solution of a Helmholtz equation depends on the constant k. From Eq. (2.17) we see that k is purely imaginary for steady state light ($\omega = 0$) and the solution is then a simple diffusion process similar to heat diffusion. For amplitude modulated light $k = k_r + ik_i$ is complex and the solution is a damped wave. Noting that the fluence is proportional to the photon number density $N = \phi/(ch\nu)$, where $h\nu$ is the photon energy, the wave can be recognized as a diffuse photon density wave (DPDW). It is important to stress that DPDWs have nothing to do with the wave nature of light since in radiative transfer theory this is completely neglected. Also they do not describe the movement

of individual photons but their collective behavior, just as thermal waves do not describe the brownian motion of single molecules.

For a detailed analysis of DPDWs see e.g. Tromberg *et al* [23], here we give only the basic properties. The imaginary part k_i determines the attenuation and the real part k_r the phase.[1]

Two regimes can be distinguished. In the low frequency regime, where $\omega \ll \mu_a c$, the imaginary part of the wave vector k_i approaches the DC effective attenuation coefficient $\mu_{eff} = \frac{1}{\delta}$, where

$$\delta = \sqrt{\frac{D}{\mu_a}} = \frac{1}{\sqrt{3\mu_a \mu'_s}} \tag{2.20}$$

is the penetration depth.[2] And $k_r \approx \omega/(2\mu_a c \delta)$ so that the phase velocity becomes $v_p = \omega/k_r \approx 2\mu_a c \delta$. Since both the attenuation and the phase velocity are approximately independent from ω this regime is called the dispersionless limit. In the high frequency regime $\omega \gg \mu_a c$ and $k_r \approx k_i \approx \sqrt{\omega/(cD)}$ thus the phase velocity as well as the attenuation are proportional to $\sqrt{\omega}$ and we have dispersion. We see that DPDWs are strongly damped. In the low frequency regime the wave or AC part has the same strong attenuation as the DC part but in the high frequency regime the AC attenuation even increases with frequency and over the distance of one wavelength the amplitude drops to 0.2% of the initial value. Typical values for the wavelength $\lambda = 2\pi/k_r$ are 5 cm for 500 MHz modulation frequency.

---

[1] Note that Tromberg *et al* define the wave vector differently. Their k_i is our k_r and vice versa.

[2] The old definition of the diffusion coefficient $\tilde{D} = 1/(3(\mu_a + \mu'_s))$ yields the (now obsolete) definiton of the penetration depth $\tilde{\delta} = \frac{1}{\sqrt{3\mu_a(\mu_a + \mu'_s)}}$.

2.3.2 Exterior Boundaries to Non–Scattering Media

A main advantage of optical methods is the prospect for non–invasive and minimal invasive applications, where light sources as well as detectors are attached to the surface of the body. From an optical point of view this situation is described as a boundary between a scattering medium and a non–scattering (clear) medium. There can also be a mismatch of the refractive indices of the tissue and the adjacent medium. Because of the high water content of tissue the refractive index is usually close to that of water. Most researchers use $n_{tissue} = 1.4$ in the near infrared spectral region. However, one should be aware that the refractive index does vary for different tissue types. Li and Xie [24] have measured values from $n_{tissue} = 1.34$ to 1.49 at 633 nm. In endoscopic applications the adjacent clear medium is usually a fluid, either water or a body fluid with high water content. The refractive index mismatch to the tissue is small and Fresnel reflection of light at the boundary can usually be neglected. We speak of a matched boundary. But in most cases the boundary is the outside surface of the body and the adjacent clear medium is air. The relative refractive index is then about $n_{rel} = n_{tissue}/n_{air} \approx 1.4$ and there is a significant reflection at the boundary.

Several studies have been devoted to the analysis of a boundary to a clear medium in terms of diffusion theory [25, 26, 27, 28, 29, 30, 21]. Solutions for other geometries than the semi–infinite half space have been summarized by Arridge *et al* [31]. Here we follow mostly Haskell *et al* [29] to derive the boundary conditions for a semi–infinite medium.

The basic assumption is that photons that once escape the scattering medium cannot re–enter the medium and are lost for the diffusion process. For a matched boundary this means that $L(\mathbf{r}, \hat{\mathbf{s}})|_{\hat{\mathbf{s}} \cdot \hat{\mathbf{n}} > 0} = 0$, where $\hat{\mathbf{n}}$ is the surface normal vector, pointing from the scattering to the clear medium, and $\mathbf{r}$ is

a point on the boundary. Diffusion theory has no means to treat individual directions $\hat{\mathbf{s}}$, therefore the radiance is integrated over the hemispheres, yielding the hemispherical fluxes[3]

$$J_{\mathbf{n}\pm}(\mathbf{r}) = \int_{\hat{\mathbf{s}}\cdot\hat{\mathbf{n}} \gtrless 0} d\hat{\mathbf{s}}\, L(\mathbf{r},\hat{\mathbf{s}})(\hat{\mathbf{s}}\cdot\hat{\mathbf{n}}). \tag{2.21}$$

Using the diffusion approximation of the radiance Eq. (2.6) this becomes

$$J_{\mathbf{n}\pm}(\mathbf{r}) = \frac{1}{4}\phi(\mathbf{r}) \pm \frac{1}{2}\mathbf{J}(\mathbf{r})\cdot\hat{\mathbf{n}}. \tag{2.22}$$

Note that the definition of the spherical fluxes is independent of the presence of a boundary. In a homogeneous medium the relations $\phi(\mathbf{r}) = 2(J_{\mathbf{n}+}(\mathbf{r})+J_{\mathbf{n}-}(\mathbf{r}))$ and $\mathbf{J}(\mathbf{r})\cdot\hat{\mathbf{n}} = J_{\mathbf{n}+}(\mathbf{r}) - J_{\mathbf{n}-}(\mathbf{r})$ hold.

At a matched boundary the hemispherical flux into the scattering medium $J_{\mathbf{n}-}(\mathbf{r})$ must be zero and the boundary condition thus becomes

$$\phi(\mathbf{r}) - 2\mathbf{J}(\mathbf{r})\cdot\hat{\mathbf{n}} = 0 \tag{2.23}$$

For a mismatched boundary a fraction of the outgoing radiance in direction $\hat{\mathbf{s}}$ is reflected back into the scattering medium according to the Fresnel reflection coefficient for unpolarized light $R(\hat{\mathbf{s}}\cdot\hat{\mathbf{n}})$[29]. In diffusion theory we can again only set the integrated quantities in relation

$$\int_{\hat{\mathbf{s}}\cdot\hat{\mathbf{n}}>0} d\hat{\mathbf{s}}\, L(\mathbf{r},\hat{\mathbf{s}})(\hat{\mathbf{s}}\cdot\hat{\mathbf{n}}) = \int_{\hat{\mathbf{s}}\cdot\hat{\mathbf{n}}<0} d\hat{\mathbf{s}}\, R(\hat{\mathbf{s}}\cdot\hat{\mathbf{n}})L(\mathbf{r},\hat{\mathbf{s}})|\hat{\mathbf{s}}\cdot\hat{\mathbf{n}}|, \tag{2.24}$$

and Eq. (2.6) yields

$$\frac{1}{2}\phi(\mathbf{r}) + \mathbf{J}(\mathbf{r})\cdot\hat{\mathbf{n}} = R_\phi\frac{1}{2}\phi(\mathbf{r}) + R_j\mathbf{J}(\mathbf{r})\cdot\hat{\mathbf{n}}, \tag{2.25}$$

where R_ϕ and R_j are the reflection coefficients for fluence and flux. With $\cos\theta = \hat{\mathbf{s}}\cdot\hat{\mathbf{n}}$ they are given by

$$R_\phi = 2\int_0^{\pi/2} d\theta\, \sin\theta\, \cos\theta R(\cos\theta) \tag{2.26}$$

$$R_j = 3\int_0^{\pi/2} d\theta\, \sin\theta\, \cos^2\theta R(\cos\theta) \tag{2.27}$$

---

[3] The boundary conditions involve only spatial dependencies and are therefore identical for steady state, time domain and frequency domain. For simplicity we give the derivation for the steady state.

and can be combined to an effective reflection coefficient

$$R_{eff} = \frac{R_\phi + R_j}{2 - R_\phi + R_j} \tag{2.28}$$

for the hemispherical fluxes, so that

$$J_{\mathbf{n}-} = R_{eff} J_{\mathbf{n}+}. \tag{2.29}$$

The boundary condition for a mismatched boundary, commonly known as the partial current boundary condition, is then

$$\phi(\mathbf{r}) - 2\,A\,\mathbf{J}(\mathbf{r}) \cdot \hat{\mathbf{n}} = 0, \tag{2.30}$$

where

$$A = \frac{1 + R_{eff}}{1 - R_{eff}} \tag{2.31}$$

is the extrapolation factor, the name will be motivated below. In this form the extrapolation factor has first been given by Haskell *et al* [29], Contini *et al* [21] have given a cumbersome analytical expression as well as a convenient polynomial fit. Figure 2.1 shows the extrapolation factor A and the effective reflection coefficient R_{eff} as well as the inaccurate extrapolation factors A_f and A_g that have been used in the past [25, 26, 28].

An exact solution for a point source subject to the partial current boundary condition has been given by Haskell *et al* [29]. However, it is somewhat awkward because it involves an exponentially decaying line source of infinite length. Therefore an approximation, the extrapolated zero boundary condition, is commonly preferred because it gives a simpler solution.

2.3.2.1 The Extrapolated Zero Boundary Condition

We use the common convention that the z-axes of the coordinate system points into the depth of the scattering medium, i.e. $\hat{\mathbf{n}} = -\hat{\mathbf{e}}_z$ and the boundary is at
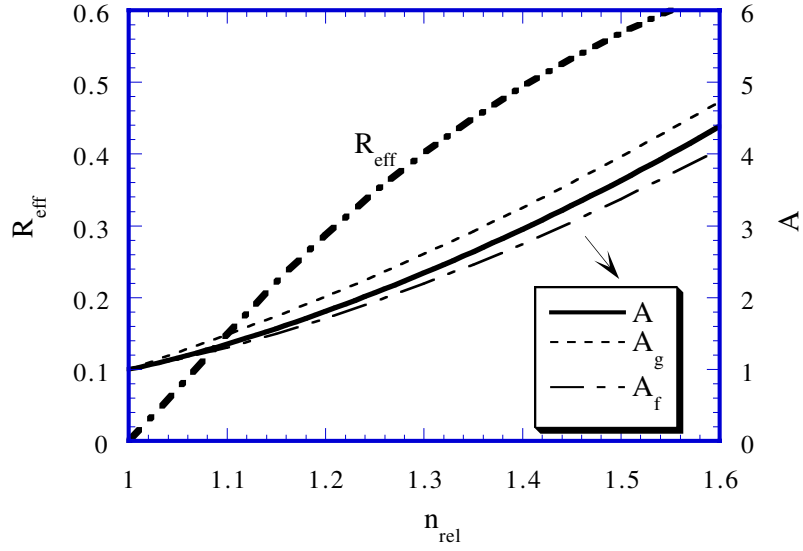
Figure 2.1: Effective reflection coefficient R_{eff} and extrapolation factor A. The inaccurate extrapolation factors A_g used by Groenhuis et al [25], and A_f used by Keijzer et al [26] and Farrell et al [28] are plotted for comparison.

$z = 0$. With $J_z = -D\partial\phi/\partial z$ the partial current boundary condition Eq. (2.30) is then

$$\phi(z = 0) + 2AD\frac{\partial\phi}{\partial z}(z = 0) = 0. \tag{2.32}$$

To simplify this boundary condition it is assumed that in the neighborhood of the boundary the fluence varies linearly in the z–direction. The fluence is then linearly extrapolated to the outside of the medium and becomes zero at the extrapolation distance $l_e = 2AD$. Note that the extrapolation distance is determined by the effective reflectivity of the boundary via the extrapolation factor A, as well as by the reduced scattering coefficient of the medium via $D = 1/(3\mu_s')$. Thus the extrapolated zero boundary condition is

$$\phi(z = -l_e) = 0 \qquad \text{with} \qquad l_e = 2AD. \tag{2.33}$$

This Dirichlet boundary condition is trivially solved with the method of image sources (see Figure 2.2): any source in the scattering medium is mirrored at the extrapolated boundary. More precisely, a semi–infinite scattering medium with
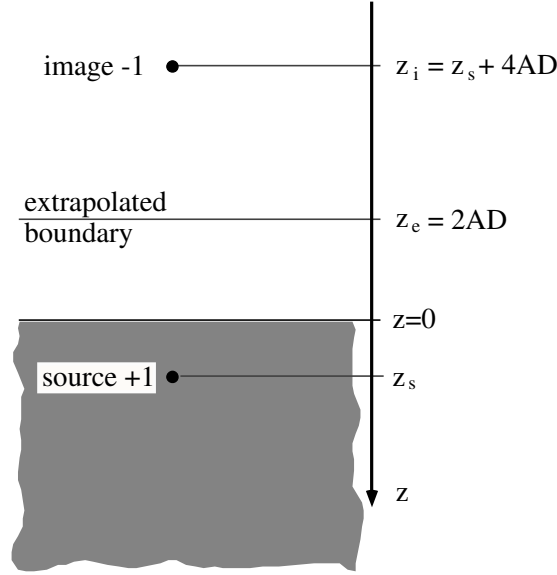
Figure 2.2:   Image source configuration for the extrapolated zero boundary condition.

a point source at $\mathbf{r}_s = (x, y, z_s)$ is replaced by an infinite medium with a point source at $\mathbf{r}_s$ and a negative image source at $\mathbf{r}_i = (x, y, -z_s - 2l_e)$. For these sources in a now infinite medium the Green's function of the homogeneous diffusion equation applies and thus the Green's function for the semi–infinite medium is

$$\hat{G}_{semi}(\mathbf{r}, \mathbf{r_s}) = \hat{G}(|\mathbf{r} - \mathbf{r_s}|) - \hat{G}(|\mathbf{r} - \mathbf{r_i}|). \tag{2.34}$$

We will use this Green's function in chapter 3 and 4 for the treatment of perturbations in inhomogeneous semi–infinite media.

2.3.2.2   Collimated Light Sources

With the Green's function we have a solution for a diffuse point source. However, the light sources most often used in biomedical optics, free laser beams and optical fibers, are best described as collimated pencil beams. For the case of isotropic scattering ($g = 0$) the description with Green's functions is

straightforward: the collimated beam is attenuated exponentially due to scattering and absorption, and the scattered part directly forms the source distribution for the diffusion problem. For the strongly forward peaked scattering in tissues ($g \approx 0.9$) the situation is more complicated. Photons that leave the collimated beam due to the first scattering event are not yet diffuse, and when they have become diffuse they have already left the collimated beam by about a reduced scattering length $1/\mu'_s$. These complications are usually avoided by mimicking the collimated beam with a single diffuse point source, placed one reduced scattering length away from the entrance of the collimated beam. This approximation gives good results at distances greater than a few reduced scattering lengths. In non–invasive applications the light enters the medium at the surface. This means that the point source is at a depth $z_s = 1/\mu'_s = 3D$ and the image source is consequently at $z_i = -4AD - 3D$, according to Fig. 2.2.

2.3.2.3   Detection of Diffuse Light

After considering light sources we now turn to light detection. Within the diffusion approximation, the power received by a detector is

$$P = \frac{1}{4\pi} \int_{A_{det}} d\mathbf{r} \int d\hat{\mathbf{s}} \, T(\hat{\mathbf{s}}) \left[\phi(\mathbf{r}) + 3\mathbf{J}(\mathbf{r}) \cdot \hat{\mathbf{s}} \right] (\hat{\mathbf{s}} \cdot \hat{\mathbf{n}}) \tag{2.35}$$

where A_{det} is the active area and $T(\hat{\mathbf{s}})$ is the aperture function of the detector. Often the aperture function $T(\hat{\mathbf{s}})$ is symmetric around the surface normal vector. Then the component of the flux perpendicular to the surface normal vector gives no contribution to the integral and thus $\mathbf{J}(\mathbf{r})$ can be replaced by $J_{\mathbf{n}}(\mathbf{r})$. According to the partial current boundary condition in Eq. (2.30) the fluence and the normal component of the net flux are proportional, $\phi = 2AJ_{\mathbf{n}}$. Therefore the detected power can be expressed either in terms of the fluence or of the normal component of the net flux [29]. For some reason it is common in the literature [28, 31, 32, 27, 33, 21] to use the normal component of the net flux as the detector signal, although this complicates the formulas. We prefer

the simpler forms obtained with the fluence and thus adopt that the detector signal is proportional to the Green's function of the semi–infinite medium Eq. (2.34).

It is instructive to address the common case of detection with multimode optical fibers. The radius of the fiber is usually small enough to assume that the integrand is independent of $\mathbf{r}$. The aperture function is approximately unity within the acceptance angle θ_{max}, that is $\hat{s} \cdot \hat{\mathbf{n}} < \theta_{max}$. Then Eq. (2.35) becomes

$$
\begin{aligned}
P &= A_{det} \frac{1}{2} \phi \left[\int_0^{\theta_{max}} d\theta \sin\theta \cos\theta + \frac{3}{2A} \int_0^{\theta_{max}} d\theta \sin\theta \cos^2\theta \right] \\
&= A_{det} \phi \underbrace{\frac{1}{4} \left(\sin^2\theta_{max} + \frac{1}{A}(1 - \cos^3\theta_{max}) \right)}_{\beta}.
\end{aligned}
\tag{2.36}
$$

For direct coupling of the fiber to the medium the acceptance angle is $\theta_{max} = \arcsin(NA/n_{medium})$, where NA is the numerical aperture in air. We assume $n_{medium} = 1.4 \rightarrow A \approx 3$ and consider two common fiber types:

- A 1000 μm fiber with a high numerical aperture $NA = 0.4$ is typical for detection systems with large area detectors like photo multipliers. We get $\beta = 0.03$, $A_{det} = 8 \cdot 10^{-3}$ cm^2 and thus

$$
P = 2.4 \cdot 10^{-3}[\text{cm}^2] \cdot \phi.
\tag{2.37}
$$

- A 100 μm fiber with a numerical aperture $NA = 0.25$ is typical for detection systems with fast small area photo diodes. We get $\beta = 0.012$, $A_{det} = 8 \cdot 10^{-5}$ cm^2 and

$$
P = 1 \cdot 10^{-6}[\text{cm}^2] \cdot \phi.
\tag{2.38}
$$

Chapter 3

Perturbation Theory for Spherical and Small Objects

As we have outlined in the introduction of chapter 2, inhomogeneities are of prime interest in biomedical optics. We saw that biological tissues are optically inhomogeneous on a large range of scales. With the use of transport theory and the diffusion approximation we sacrifice the microscopic variations by using average optical properties, but the variations on the range of millimeters and centimeters remain. In the scattering dominated regime, i.e. in the near infrared spectral range, this means that the diffusion equation (2.14) has to be solved for spatially varying $D(r)$ and $k(r)$.

One way to tackle this problem is to resort to numerical brute force approaches like finite element and finite difference methods. These powerful and well established techniques are the methods of choice if the medium is very inhomogeneous. They have, however, some drawbacks. As all purely numerical methods they cannot offer the physical understanding an analytical description provides. Moreover, the computational cost for calculations in three dimensional geometries is high, and biological systems usually lack symmetry

properties that would allow to reduce the dimensionality.

An elegant way to avoid these drawbacks is to describe light propagation in terms of *perturbation theory*. This approach is appropriate if the system can be approximated as a background medium with some included objects of different optical properties. The light field is splitted into the solution for the unperturbed background medium ϕ_0 and a perturbation ϕ^{pert} that is caused by the presence of the objects. Note that this approach does not work always. It fails if the perturbation is too strong, i.e. if the optical properties of the objects are too different from the background and/or if the objects are too large. It can also happen that the ansatz to split the fluence in background and perturbation part is simply not practical because the background, or unperturbed, medium is too complicated. Then neither the solution for the background part nor for the perturbation part can be readily obtained. We will encounter such a situation in chapter 6, where a clear layer in the background medium even precludes the use of the diffusion approximation. This will force us to resort to Monte Carlo simulations.

However, for rather homogeneous organs like breast, prostrate, or muscle, perturbation theory does work and is often the method of choice to analyze the light propagation. For example, all tomographic reconstruction strategies are based upon a perturbation ansatz.

We start this chapter with a discussion of an analytical solution of the diffusion equation for a spherical object in a homogeneous medium. By itself, this solution has only limited practical value because inclusions in biological tissues are usually not spherically. We will therefore take the limits for small objects and weak perturbations to obtain a simple solution for pointlike perturbations and discuss the basic differences for absorption and scattering changes. The solution for pointlike perturbations is then used to address the spatial sensitivity of reflection mode measurements for absorbing and scattering inho-

mogeneities. A design study for an optical probe for the detection of buried absorbers concludes the chapter.

3.1   Analytical Solution for a Spherical Object

Analytical solutions of the inhomogeneous diffusion equation are only available for simple piece wise homogeneous geometries. In this section we discuss the solution for a spherical object in an otherwise homogeneous infinite medium, illuminated by a single point source. Inside, the sphere has constant optical properties μ_{a1}, μ'_{s1}, but they are different from the μ_{a0}, μ'_{s0} on the outside. It is convenient to define the differences $\Delta\mu_a = \mu_{a1} - \mu_{a0}$ and $\Delta\mu'_s = \mu'_{s1} - \mu'_{s0}$.

Since the optical properties are constant inside each region, the *homogeneous* diffusion equation (2.16) is valid in each region. The solution is then determined by the boundary conditions at the interface of the two media and by the restriction that the fluence must vanish at infinity.

Outside the sphere the general solution is a superposition of the incoming fluence ϕ_0 and the scattered fluence ϕ^{Pert}, while inside the sphere we have ϕ^{Ins}. All three functions are now expanded in a suitable system of basis functions. The spherical symmetry suggests a multipole expansion of the Helmholtz equation as it is known from Electrodynamics [34]. The expansion coefficients are determined using boundary conditions at the surface of the sphere. For the radial part spherical Bessel and Hankel functions are used. For the angular part, Boas *et al* [35] and Hielscher *et al* [36] have originally used the most general approach of a spherical harmonics expansion. However, using the azimuthal symmetry around the axes between source and center of the sphere, one can immediately use Legendre polynomials [37].

The center of the sphere is set at the origin of the coordinate system, the illuminating point source of strength S is at the position $\mathbf{r_s}$, and the detector is at $\mathbf{r}$. From Eq. (2.19) in section 2.3.1 we recall that the incoming fluence ϕ_0 is simply described by the impulse response $\hat{G}$ scaled by the source strength S

$$\phi_0 \;=\; S\hat{G}(|\mathbf{r} - \mathbf{r_s}|, \omega) \;=\; \frac{S}{4\pi D_0 |\mathbf{r} - \mathbf{r_s}|} \exp(ik_0 |\mathbf{r} - \mathbf{r_s}|), \qquad (3.1)$$

where k_0 is the wave vector (see Eq. (2.17)), and $D_0 = 1/(3\mu'_{s0})$ is the diffusion coefficient for the surrounding medium (see Eq. (2.13)). Note that the frequency dependence is hidden in the wave vector k_0. We then get the multipole expansion

$$\phi_0 = S\frac{ik_0}{D_0} \sum_{l=0}^{\infty} j_l(k_0 r_<) h_l^{(1)}(k_0 r_>) \frac{(2l+1)}{4\pi} P_l(\cos\alpha) \qquad (3.2)$$

where j_l are spherical Bessel functions, $h_l^{(1)}$ are spherical Hankel functions of the first kind, P_l are Legendre polynomials, α is the angle between $\mathbf{r}$ and $\mathbf{r_s}$, $r_<$ is the smaller and $r_>$ is the larger of $|\mathbf{r}|$ and $|\mathbf{r_s}|$. For the evaluation of the boundary conditions at the surface of the sphere we have $r_< = |\mathbf{r}|$ and $r_> = |\mathbf{r_s}|$.

The perturbed fluence ϕ^{Pert} and the fluence inside the sphere ϕ^{Ins} are expanded with the same angular part. ϕ^{Pert} has to be an outgoing wave, thus the radial part must be described with spherical Hankel functions of the first kind and we get

$$\phi^{Pert} = \sum_{l=0}^{\infty} A_l \, h_l^{(1)}(k_0 r) \frac{(2l+1)}{4\pi} P_l(\cos\alpha), \qquad (3.3)$$

where the A_l are expansion coefficients for the perturbed fluence. For ϕ^{Ins} standing wave solutions have to be used for the radial part, i.e. spherical Bessel and Neumann functions. The condition that ϕ^{Ins} has to be finite inside the sphere rules out spherical Neumann functions and we get

$$\phi^{Ins} = \sum_{l=0}^{\infty} B_l \, j_l(k_1 r) \frac{(2l+1)}{4\pi} P_l(\cos\alpha), \qquad (3.4)$$

where k_1 is the wave vector for the medium inside the sphere and the B_l are expansion coefficients for the fluence inside the sphere.

To determine the expansion coefficients A_l and B_l we employ the boundary conditions at the surface of the sphere at $r = |\mathbf{r}| = a$. They state that the fluence ϕ as well as the normal component of the net flux $J_r = -D\partial\phi/\partial r$ must be continuous:

$$
\begin{aligned}
\phi_0(a) + \phi^{Pert}(a) &= \phi^{Ins}(a) \\
D_0\frac{\partial\phi_0}{\partial r}(a) + D_0\frac{\partial\phi^{Pert}}{\partial r}(a) &= D_1\frac{\partial\phi^{Ins}}{\partial r}(a).
\end{aligned}
\tag{3.5}
$$

With the abbreviations $x = k_0 a$ and $y = k_1 a$ we get

$$
A_l = -S\frac{ik_0}{D_0}h_l^{(1)}(k_0 r_s)\frac{D_0 x j_l'(x)j_l(y) - D_1 y j_l(x)j_l'(y)}{D_0 x h_l^{(1)\prime}(x)j_l(y) - D_1 y h_l^{(1)}(x)j_l'(y)}
\tag{3.6}
$$

and

$$
B_l = S\frac{ik_0}{D_0}h_l^{(1)}(k_0 r_s)\frac{D_0 x h_l^{(1)\prime}(x)j_l(x) - D_0 x h_l^{(1)}(x)j_l'(x)}{D_0 x h_l^{(1)\prime}(x)j_l(y) - D_1 y h_l^{(1)}(x)j_l'(y)},
\tag{3.7}
$$

where the prime denotes the derivative of the function with respect to its argument x or y respectively. The series converges for $x < 1$ [35].

An implementation of this solution as MATHEMATICA code can be found in [38]. A numerical implementation in ANSI C by D. Boas [18] is available as part of the software package PMI, which will be discussed in section 5.7.2. We will use it as a verification for the iterative perturbation approach we develop in chapter 4.

3.2 Pointlike Perturbations

Although the solution from the last section is analytical it is too awkward to gain real insight in the nature of the solution. In this section we will therefore

develop an approximation for small spheres which allows to discuss some basic properties of scattering and absorbing perturbations.

We concentrate on the perturbed fluence ϕ^{Pert} outside the sphere. Regrouping the terms in Eqs. (3.3) and (3.6) the perturbed fluence becomes

$$\phi^{Pert} = S\frac{k_0}{4\pi D_0} \sum_{l=0}^{\infty} h_l^{(1)}(k_0 r_s)\, h_l^{(1)}(k_0 r) P_l(\cos\alpha)\, f_l \qquad (3.8)$$

with

$$f_l = -i\,(2l+1)\,\frac{D_0 x j_l'(x) j_l(y) - D_1 y j_l(x) j_l'(y)}{D_0 x h_l^{(1)\prime}(x) j_l(y) - D_1 y h_l^{(1)}(x) j_l'(y)}\,. \qquad (3.9)$$

The size and optical properties of the sphere contribute only to f_l.

3.2.1   Small Object and Weak Perturbation

To simplify Eq. (3.9) we will assume that the sphere is small and the perturbation is weak. *Small* means that the dimension of the inclusion is optically thin for the surrounding medium, i.e. the unperturbed fluence ϕ_0 does not change significantly over the radius of the sphere a. This is the case if $x = k_0 a \ll 1$. *Weak* means that the object itself is optically thin, i.e. the total (perturbed) fluence ϕ does not change significantly over the object. This is the case if $y = k_1 a \ll 1$.

We can then use the limiting forms of the spherical Bessel and Hankel functions for small arguments x (and y)

$$
\begin{aligned}
h_l^{(1)}(x) &\rightarrow -i\,\frac{(2l-1)!!}{x^{l+1}}\\[6pt]
h_l^{(1)\prime}(x) &\rightarrow i\,(l+1)\frac{(2l-1)!!}{x^{l+2}}\\[6pt]
j_l(x) &\rightarrow \frac{x^l}{(2l+1)!!}\\[6pt]
j_l'(x) &\rightarrow
\begin{cases}
-\frac{1}{3}x & : \quad l=0\\[6pt]
\frac{l}{(2l+1)!!}x^{l-1} & : \quad l>0
\end{cases}
\end{aligned}
\qquad (3.10)
$$

where the double factorial $(n)!! = n(n-2)(n-4)\cdots(1)$. For $l = 0$ the limiting form of the derivative of the spherical Bessel function j_0' has to be derived from the explicit form $j_0(x) = \sin x/x$. We will see that this exception has an interesting consequence for the behavior of the solution. With Eq. (3.10) f_l becomes:

$$f_{l>0} = \frac{-x^{2l+1}}{((2l-1)!!)^2} \frac{l\,\Delta\mu_s'}{(l+1)\,\Delta\mu_s' + (2l+1)\,\mu_{s0}'} \tag{3.11}$$

$$f_{l=0} = \frac{k_0}{3D_0}\,a^3\,\Delta\mu_a, \tag{3.12}$$

where the dipole term is explicitly:

$$f_{l=1} = -k_0^3\,a^3\,\frac{\Delta\mu_s'}{3\mu_{s0}' + 2\Delta\mu_s'}. \tag{3.13}$$

Thus we have the remarkable result that for a small and weak perturbation the monopole term of the perturbed fluence depends only on the difference in the absorption coefficients $\Delta\mu_a$, while all higher orders depend only on the difference in the reduced scattering coefficient $\Delta\mu_s'$. Both the monopole and the dipole term are of the order a^3 and are thus proportional to the volume of the sphere. Higher terms drop quickly because of the double factorial and higher powers in $x = k_0 a$. Using the explicit forms of the spherical Hankel function $h_0^{(1)}(x) = -i\exp(ix)/x$ and $h_1^{(1)}(x) = -\exp(ix)(1/x + i/x^2)$ in Eq. (3.8) the perturbed fluence becomes

$$\phi^{Pert} = -S\,\frac{4\pi}{3}a^3\,\frac{e^{ik_0 r}}{4\pi D_0 r}\,\frac{e^{ik_0 r_s}}{4\pi D_0 r_s}\,\Delta\mu_a \tag{3.14}$$

$$+ \; S\,\frac{4\pi}{3}a^3\,\frac{e^{ik_0 r}}{4\pi D_0 r}\left(ik_0 - \frac{1}{r}\right)\frac{e^{ik_0 r_s}}{4\pi D_0 r_s}\left(ik_0 - \frac{1}{r_s}\right)\cos\alpha\,D_0\,\frac{3\Delta\mu_s'}{3\mu_{s0}' + 2\Delta\mu_s'}.$$

Recognizing the Green's function Eq. (2.19) and its gradient we can express Eq. (3.14) as

$$\phi^{Pert} = -S\,\frac{4\pi}{3}a^3\,\hat{G}(r_s)\,\hat{G}(r)\,\Delta\mu_a$$

$$+ \; S\,\frac{4\pi}{3}a^3\,\boldsymbol{\nabla}\hat{G}(r_s)\cdot\boldsymbol{\nabla}\hat{G}(r)\,D_0\,\frac{3\Delta\mu_s'}{3\mu_{s0}' + 2\Delta\mu_s'}. \tag{3.15}$$

This is an important result. Small absorbing objects cause a monopole perturbation. If the absorption in the object is higher than in the background medium the light field is depleted. Thus the increased absorption is modeled with a negative monopole source. To distinguish it from the real light sources we call this a *virtual* source. Small scattering objects behave different. For increased scattering they cause a dipole virtual source which reflects fluence back into the direction of the real source and depletes the light field on the far side.

In chapter 4 we will extend the concept of virtual sources to discuss extended perturbations of arbitrary shape. This approach will provide more insight in the different behavior of scattering and absorbing perturbations and will show that the basic difference is caused by a surface term that is only caused by a scattering change.

Before we proceed to use Eq. (3.15) we have to address the validity of the approximation: How small and how weak must a perturbation be for Eq. (3.15) to hold? For what size do we have to resort to the theory for extended perturbations? In Figure 3.1 the behavior of the first moments is exemplified for some practically relevant parameter sets. Shown are the exact solutions of the expansion coefficient f_l obtained with Eq. (3.9) as solid lines and the approximation for small and weak perturbations Eqs. (3.11, 3.12) as dashed lines. From the top row to the bottom row the optical thickness of the inclusion for the surrounding medium $|ak_0|$ increases as the size and/or the modulation frequency increases, and is 0.35, 0.46, 0.87, and 1.15 respectively.

The left column shows the expansion coefficients f_l for an absorbing object with $\Delta\mu_a \neq 0$, the right column for a scattering object with $\Delta\mu'_s \neq 0$. In order to compare how the expansion coefficients vary with changing μ_{a1} and μ'_{s1} it is convenient to normalize these parameters to their background values μ_{a0} and
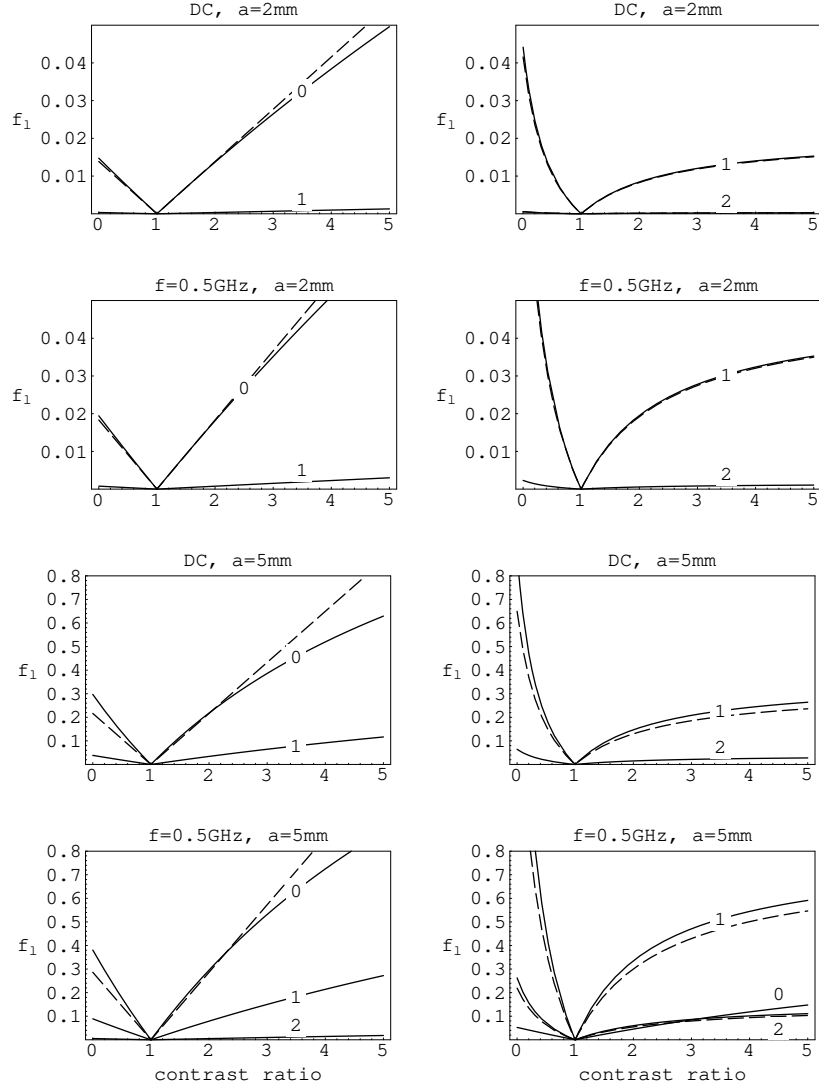
Figure 3.1: Absolute values of the coefficients f_l of the multipole expansion as a function of the contrast ratio γ. Results for spheres with a = 2 mm and a = 5 mm radius, for steady state light (DC), and for amplitude modulated light with modulation frequency f = 500 MHz. Left column: absorbing object with $\mu_{a1} = \gamma\mu_{a0}$; right column: scattering object with $\mu'_{s1} = \gamma\mu'_{s0}$. The background optical properties are $\mu_{a0} = 0.1\ cm^{-1}$, $\mu'_{s0} = 10\ cm^{-1}$. Solid lines were computed with the exact solution Eq. (3.9), dashed lines with the limit for pointlike weak perturbations Eqs. (3.11, 3.12). The order of the moments are indicated at the lines.

μ'_{s0} by means of a *contrast ratio* parameter γ

$$\mu_{a1} = \gamma\mu_{a0} \tag{3.16}$$

$$\mu'_{s1} = \gamma\mu'_{s0}$$

which signifies the relative strength of the perturbation. Note that the optical thickness $|ak_1|$ of the object itself scales with the contrast ratio γ. Consequently, for $\gamma > 1$ the weak perturbation condition $|ak_1| \ll 1$, is fulfilled worse than the small object condition $|ak_0| \ll 1$.

Figure 3.1 shows that for a radius $a = 5$ mm the small object approximation is violated both for the absorbing and the scattering sphere, as could be expected from the high $|ak_0|$ values. For the scattering sphere with a modulation frequency $f = 500$ MHz this results in a significant monopole moment (which is even larger than the quadrupole moment), in clear contradiction to Eq. (3.12). For the absorbing sphere the appearance of the dipole moment indicates the violation of the small object approximation.

3.2.2   Small Object and Strong Perturbation

The behavior for stronger perturbations is different for scattering and absorbing spheres.

For the scattering sphere the approximation for dipole and higher moments is surprisingly robust for large contrast ratios γ, even for the large sphere with $a = 5$ mm radius. In biological tissues the scattering coefficient does not vary too strongly, a scattering contrast up to five, as in Fig. 3.1, should cover most cases. The dipole approximation of Eq. (3.15) is therefore limited by the size of the object, with an upper limit of at least 2 mm radius. The situation is different for inclusions with lower scattering than the background

medium. While in 'normal tissues' the contrast ratio for lower scattering is not very pronounced there is an important exception: regions with clear, non–scattering fluids like the ventricular system with cerebrospinal fluid in the brain (see chapter 6). In these cases the diffusion approximation breaks down and one has to resort to Monte Carlo simulations.

For an absorbing sphere Fig. 3.1 shows that the monopole moment begins to deviate from the approximate form for contrast ratios $\gamma \gtrsim 2.5$ and starts to saturate. Since for $\mu_{a1} \to \infty$ the conservation of energy forces the strength of the perturbation to saturate eventually, it is clear that Eq. (3.12) with its linear dependence on $\Delta\mu_a$ must fail for large μ_{a1}. However, it is remarkable that even for the relatively small sphere with $a = 2$ mm the deviation starts already at an absorption contrast of only three. Absorption contrasts can be high in biomedical applications, examples are tumors marked with contrast agents and, more common, blood vessels and hemorrhages. The typical volume concentration of blood in tissue is about 3%. Most of it is distributed in the tissue quasi continuously in small capillaries and thus determines the absorption coefficient of tissues in the visible NIR spectral range. Larger regions of whole blood will therefore have an absorption contrast to the surrounding of about $\gamma = 33$. The scattering is close to that of many tissue types. A practically relevant question is therefore: How large may a bleeding or a vessel be to be described accurately with the simple monopole perturbation model Eq. (3.15)? Figure 3.2 shows that the simple approximation deviates from the exact solution for radii greater than about 0.7 mm due to saturation. The dipole moment essentially plays no role.

Note that diffusion theory is not expected to work properly *inside* such a strong absorber as whole blood ($\mu_a \approx 15$ cm^{-1} $\mu_s' \approx 8$ cm^{-1} @ $\lambda = 760$ nm [39]). But the boundary condition of continuous flux and fluence we used to derive the exact solution relies on diffusion theory to work inside the object. One approach to overcome this limitation is to approximate blood as a perfect
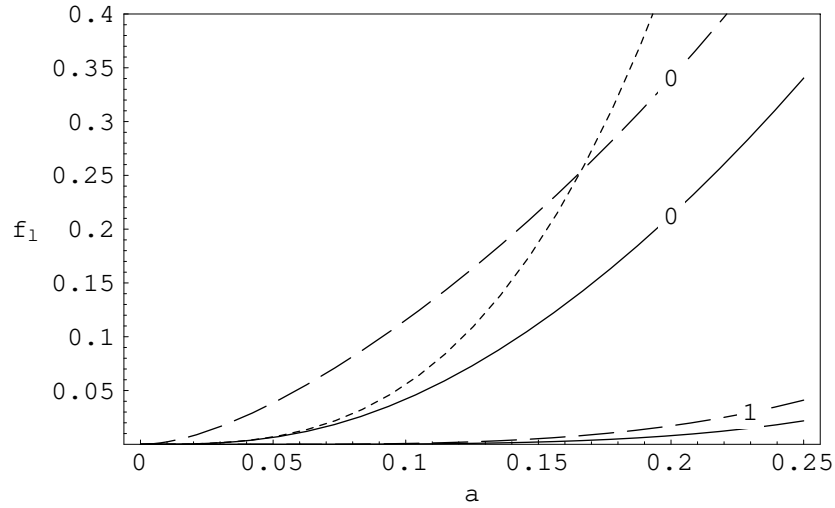
Figure 3.2: Absolute value of the first moments for a strongly absorbing sphere and steady state light as a function of the radius a[cm]. The contrast ratio $\gamma = 33$ is typical for blood aggregations in the surrounding tissue. Shown are the monopole moments (0) and dipole moments (1) of the exact solution (solid line) and the perfect absorber (dashed line), and the approximation for small and weak perturbation (dotted line).

absorber and to use the boundary condition of no outgoing partial flux $J_{\mathbf{r}-} = 0$, where no assumptions are made for the inside of the object. The expansion coefficient f_l becomes:

$$f_l^{abs} = -i(2l+1)\frac{3\mu'_{s0}\,j_l(x) - 2k_0 j'_l(x)}{3\mu'_{s0}\,h_l^{(1)}(x) - 2k_0 h_l^{(1)\prime}(x)}. \tag{3.17}$$

Figure 3.2 shows that the monopole moment for a perfect absorber f_0^{abs} (dashed line) does not agree at all with the exact solution for small objects, but for a radius $a \gtrsim 1.7$ mm the agreement is at least better than with the small and weak approximation, which diverges quickly.

Thus the small and weak approximation should not be expected to quantitatively describe blood volumes larger than about 3 mm in diameter. However, we see that the dipole moment can be neglected for the perfect absorber too. This means that although the approximation for small and weak perturbations

overestimates the strength of strong absorbing perturbations it can nevertheless be used to explore the spatial behavior of absorbing perturbations.

In summary, absorbing perturbations cause a perturbation with a dominant monopole moment, while for scattering perturbations the dipole moment is dominant. For perturbations smaller than 4 mm in diameter higher multipole terms can be neglected. This means that the shape of such small objects does not influence the perturbation outside the objects, they can therefore be treated as pointlike perturbations. Both leading moments scale with the volume of the perturbation. For pointlike absorbing perturbations with a contrast ratio less than about three the perturbation is linear in $\Delta\mu_a$. For higher contrast the perturbation begins to saturate and can be described with Eq. (3.9), the limiting form for perfect absorbers is Eq. (3.17). Although scattering perturbations are linear only for $\Delta\mu'_s \ll \mu'_{s0}$ the simple form in Eq. (3.14) holds for all practically relevant contrast ratios in tissues, except for clear, non–scattering regions.

3.3   Sensitivity Maps

Sensitivity maps visualize the spatial distribution of the sensitivity of a measurement for the presence of perturbations. The idea is to keep the source and detector position fixed and to calculate the change of the detector response a perturbation at different positions would cause. The knowledge of this sensitivity for all volume elements of interest is the basis of most tomographic approaches to reconstruct the optical properties from measurements on the outside of the medium. It is also of great interest for applications that do not aim for a full tomographic reconstruction, as for example local measurements of the averaged optical properties. Here sensitivity maps can be used to assess the errors inhomogeneities cause in algorithms that assume homogeneous media. We will use sensitivity maps in section 3.4 for a design study for an optical probe to detect surface near brain hematomas. Here we proceed with the definition of the formalism and thereafter specialize on sensitivity maps for absorbing perturbations in section 3.3.1 and for scattering perturbations in section 3.3.2.

For absorbing perturbations the sensitivity has been described as 'photon–hitting density' [40], 'photon sampling volume' [41], 'weighting function' [42], and 'photon visit probability' [33]. These names are inspired by an intuitive physical interpretation of the nature of the perturbed measurement. Consider photons which actually travel from source to detector in the unperturbed medium and monitor the volume were we will put the test perturbation. The change of the detector signal due to a change of the absorption must depend on the average pathlength these photons spend in the volume of interest. This can be computed directly with Monte Carlo simulations by recording and analyzing the photon paths. We will use this approach in chapter 6 to obtain sensitivity maps for measurements on the head, because diffusion theory cannot be applied there.
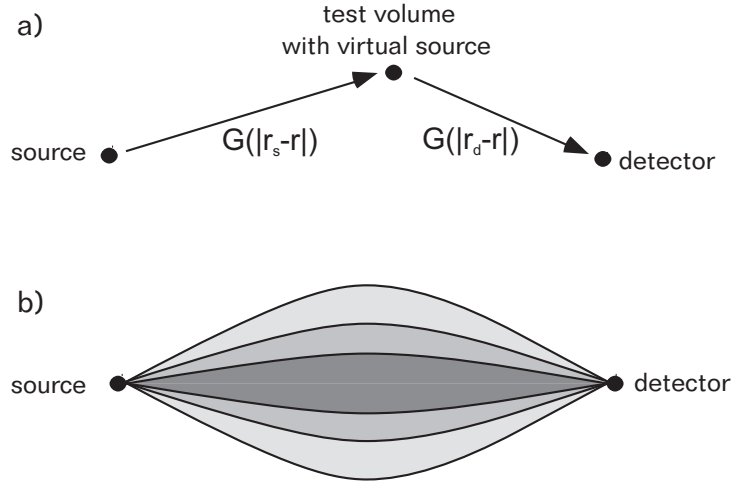
Figure 3.3: Principle of the sensitivity map.

In the framework of diffusion theory the sensitivity for a small absorption change in a small volume can be described with the monopole approximation we have developed in the last section (Eq. 3.15)

$$\phi^{Pert} = -S\, \frac{4\pi}{3} a^3\, \hat{G}(|\mathbf{r}_s - \mathbf{r}|)\, \hat{G}(|\mathbf{r} - \mathbf{r}_d|)\, \Delta\mu_a, \tag{3.18}$$

where $\mathbf{r}_s$, $\mathbf{r}$, and $\mathbf{r}_d$ are the positions of source, test volume, and detector respectively, S is the source strength, and a is the radius of the test volume, see Fig. 3.3a. The first Green's function determines how much light gets from the source to the test volume. The virtual source strength determines how much the perturbation changes the light propagation, for the absorption perturbation this is simply the product of the volume and the change in absorption $V\Delta\mu_a$. Then the second Green's function determines how this change propagates to the detector. The product of both Green's functions is sometimes referred to as 'three point Green's function' $\hat{G}(\mathbf{r}_s, \mathbf{r}, \mathbf{r}_d) = \hat{G}(|\mathbf{r}_s - \mathbf{r}|)\, \hat{G}(|\mathbf{r} - \mathbf{r}_d|)$. When the sensitivity is plotted for varying $\mathbf{r}$ the region with high sensitivity spans between source and detector in a shape that resembles a banana, as is schematically shown in Fig. 3.3b. For this reason the sensitivity maps are also called 'photon bananas'. Arridge *et al* [32, 43] have refined the photon banana concept (and coined the term 'photon measurement density functions')

to distinguish between the different measurement modalities, viz. integrated intensity for DC measurements, amplitude ratio and phase difference for frequency domain measurements, and the temporal moments for time domain measurements.

Although originally developed for absorption perturbations, the concept of the sensitivity maps or photon bananas can naturally be extended to scattering perturbations simply by replacing the absorbing test perturbation with a scattering test perturbation. We use of the dipole approximation in Eq. (3.15), i.e.

$$\phi^{Pert} = S\,\frac{4\pi}{3}a^3\,\boldsymbol{\nabla}\hat{G}(|\mathbf{r}_s - \mathbf{r}|)\cdot\boldsymbol{\nabla}\hat{G}(|\mathbf{r} - \mathbf{r}_d|)\,D_0\,\frac{3\Delta\mu'_s}{3\mu'_{s0} + 2\Delta\mu'_s}, \qquad (3.19)$$

to describe the effect of the scattering perturbation on the detector signal. However, the physical interpretation is not as straightforward as for the absorption change. Principally, due to the different scattering in the perturbation the paths of the photons which pass through this volume are altered. But the multipole expansion formalism does not facilitate an intuitive explanation why this is mediated by the *gradient* of the Green's functions, not the Green's functions themselves. We have to delay an interpretation until the virtual source approach is fully developed in section 4.

Generally, sensitivity maps can be obtained for all measurement geometries. For tomographic applications mostly measurements in transmission mode or on the circumference of a cylindrical medium were investigated. The curved photon bananas can be used in backprojection image reconstruction approaches [44]. However, because of the high attenuation in biological tissue source–detector separations are limited to about 5 to 10 cm, depending on the optical properties. Practically, this means that for some important applications, like imaging of breast cancer [45, 46, 47, 44] and brain imaging in neonates [48], transmission measurements can be used. But in this work we are especially interested in optical measurements on the adult head, where the larger diameter

and high scattering coefficient of the brain make transmission measurements impossible. Any optical diagnostic methods on the adult head are thus restricted to the reflection mode. In the following we will therefore concentrate on the discussion of sensitivity maps for reflection mode measurements in a semi–infinite geometry. One could argue that it would be more appropriate to use a spherical or cylindrical geometry with the average diameter of a head, but the curvature on a human head is actually quite variable. On the temporal lobe the scull is rather flat, even with some concave regions, while on the frontal lobe the curvature is pronounced. Thus there is no typical curvature and for the sake of simplicity we can as well choose the semi–infinite case.

In section 2.3.2 we showed that the extrapolated zero boundary condition can be satisfied by adding an image source on the outside of the medium for each real source in the medium. This principle applies as well to virtual sources which are caused by a perturbation. Thus the form of the monopole and dipole terms in Eq. (3.15) is unchanged except that the Green's functions for
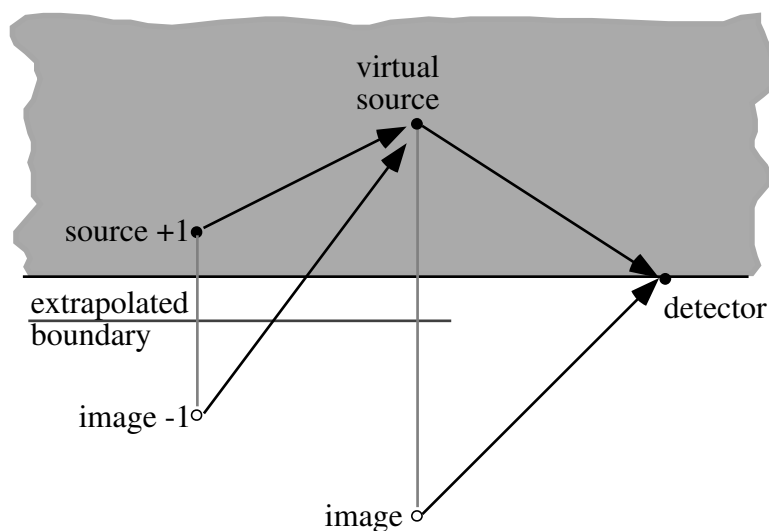

Figure 3.4: Image source configuration for a perturbation in a semi–infinite geometry.

homogeneous media are now replaced by the Green's functions for semi–infinite media according to Eq. (2.34), that is by a sum of the Green's functions for the source and its image source. This situation is depicted in Figure 3.4. Note that for the scattering perturbation the gradient of the sum has to be taken.

In the following two sections we will discuss the properties of sensitivity maps for scattering and absorbing perturbations for steady state and for frequency domain measurements. The results will be used for the design study of an optical probe in section 3.4.

3.3.1   Sensitivity Maps for Absorption Perturbations

The form and strength of the sensitivity maps depends on the values of the optical properties of the background medium, the source–detector distance, the modulation frequency, and of course on the measurement modality. We consider the amplitude ratio ϕ/ϕ_0 and the phase difference $\arg(\phi) - \arg(\phi_0)$ of the detected diffuse photon density wave ϕ in the perturbed medium relative to the DPDW ϕ_0 in the unperturbed background medium . To get an overview over the principal behavior of the photon bananas we choose a typical example of a reflection mode measurement and then vary the modulation frequency and the source–detector distance.

Figure 3.5 shows the geometry of our example sensitivity map. The light enters the background medium ($\mu_{a0} = 0.1$ cm^{-1}, $\mu'_{s0} = 10$ cm^{-1}) at the surface of the medium at (0,0,0). The equivalent diffuse point source is therefore placed at a depth of one mean free path below the surface at $\mathbf{r}_s = (0, 0, 0.1)$ (all distances are given in cm). The detector is placed in 2 cm distance at $\mathbf{r}_d = (2, 0, 0)$.

In order to appreciate the practically achievable signals we use a reasonably macroscopic absorbing test perturbation of $a = 2$ mm radius and a contrast
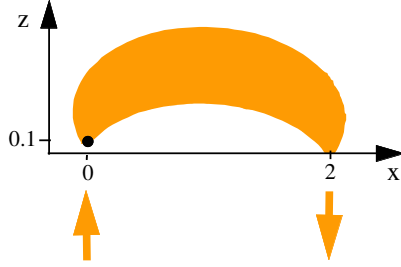
Figure 3.5: Geometry for sensitivity maps in semi–infinite media.

ratio $\gamma = 2$, that is $\mu_{a1} = \gamma\mu_{a0} = 0.2$ cm^{-1} and consequently $\Delta\mu_a = 0.1$ cm^{-1}. From section 3.2.1 we know that such a perturbation can still accurately be described with the monopole approximation. In Figs. 3.6, 3.7, and 3.8 the sensitivity is shown for different modulation frequencies. The contour plots in Fig. 3.6 together with the surface plots in Fig. 3.7 give a good qualitative impression of the photon bananas, while the line plots in Fig. 3.8 for a cut through the $y = 0$ plane half way between source and detector are useful for a quantitative comparison.

We see that for increasing modulation frequency the photon bananas for the amplitude ratio as well as for the phase difference move nearer to the surface. Also, the extrema become stronger and sharper. Consequently, high modulation frequencies are appropriate for high resolution measurements near the surface, while lower modulation frequencies are better suited for deeper measurements. While these trends hold for both amplitude ratio and phase difference there are also differences. The photon bananas for the phase difference generally penetrates deeper into the medium than for the amplitude ratio. Figure 3.7 shows that the strength of the banana for phase difference is relatively uniform over its way from source to detector, while the banana for amplitude ratio is strongly peaked near source and detector. This suggests to use phase measurements for the detection of buried absorbers since they are relatively insensitive to variations of the optical properties at source and detector, and to use relatively low modulation frequencies for a deep penetration of

Amplitude Ratio

Phase Difference

Figure 3.6:　Photon bananas for absorbing perturbations in the x–z–plane be-tween source and detector (dimensions in cm), for DC light and for modulation frequencies from 30 MHz to 1 GHz. The plot range for all amplitude ratios is 0.96 to 1.01. For the phase difference the plot ranges in degree are -0.18 to 0.1 for 30 MHz, -0.45 to 0.3 for 100 MHz, -0.8 to 0.4 for 300 MHz, and -1.1 to 0.5 for 1 GHz.

Figure 3.7: Photon bananas for absorbing perturbations. Top row: amplitude ratio; bottom row: phase difference in degrees. Left column: f = 100 MHz; right column: f = 1000 MHz.

the sensitive region. However, Fig. 3.8 shows that the maximum phase difference strongly decreases for lower frequencies. The phase errors of the detection system will therefore limit the use of lower frequencies. Currently, about 0.05 degree phase accuracy are realistically for shot noise limited systems [49].

Note that the phase difference has a dominant region with a negative phase difference, but also a less pronounced positive region near the surface. This is caused by the distribution of the pathlength of the photons. Photons with a shorter total pathlength travel on average nearer to the surface, while photons with a longer total pathlength travel on average deeper in the medium. Thus

Figure 3.8: Sensitivity for absorbing perturbations versus depth half way between source and detector, i.e. on a line from (1,0,0) to (1,0,1.5).

an absorber near to the surface dampens predominantly the 'fast' photons and the total phase is delayed, while an absorber deeper in the medium dampens the 'slow' photons and the phase is advanced.

The second parameter which can be varied in reflection mode measurements is the source–detector distance. Figure 3.9 shows that for increasing source–detector distance the maximum of the sensitivity moves deeper into the medium while the sensitivity drops. Note that the sensitivity decrease of the phase difference is less pronounced than for the amplitude ratio.
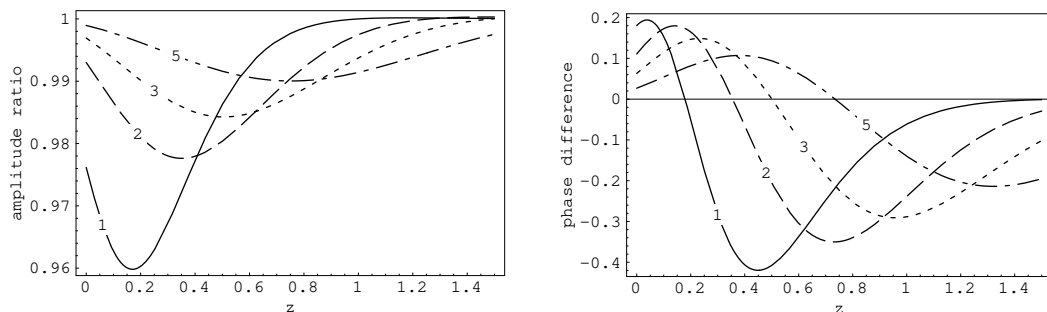
Figure 3.9: Sensitivity for absorbing perturbations, source–detector separations between 1 and 5 cm, f = 100 MHz.
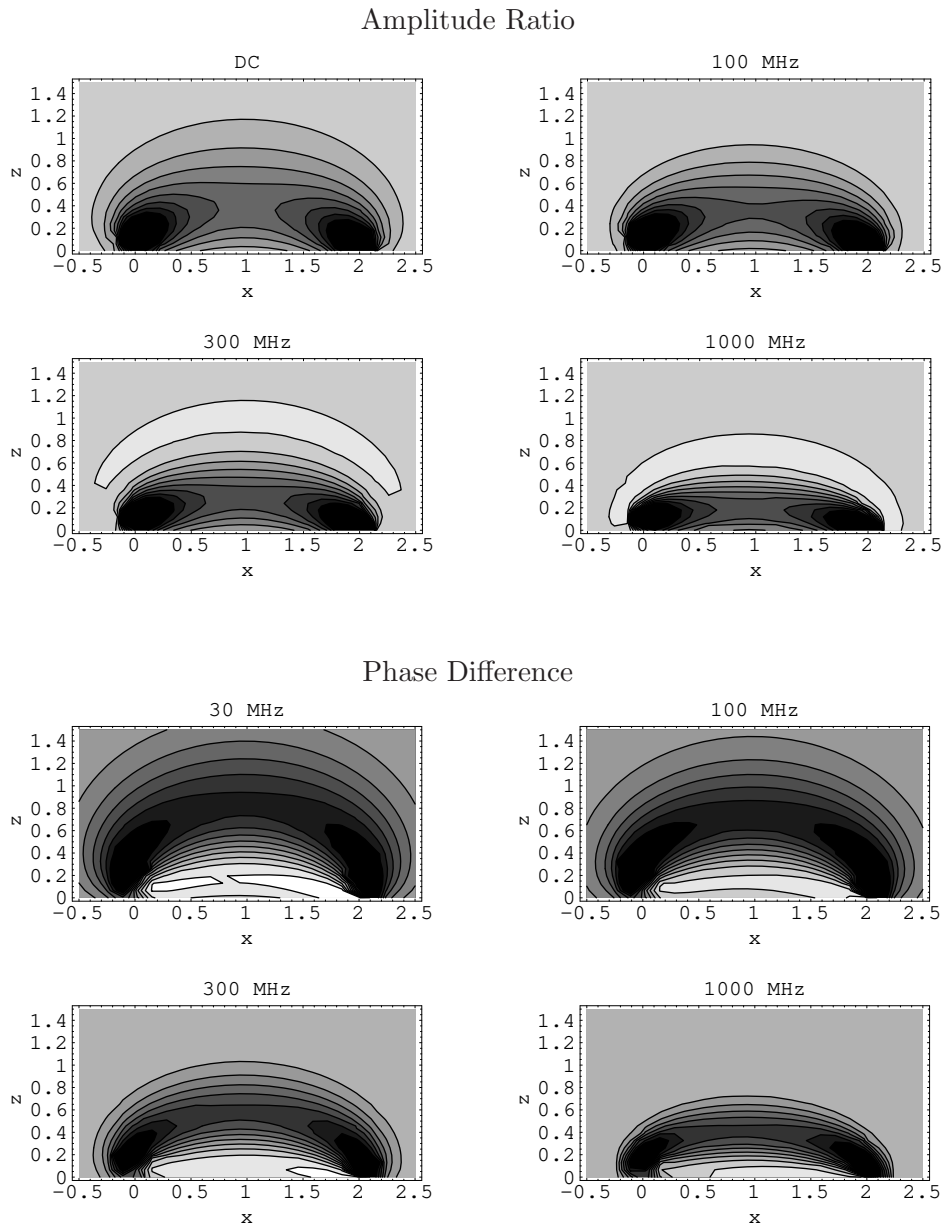
Amplitude Ratio

Phase Difference
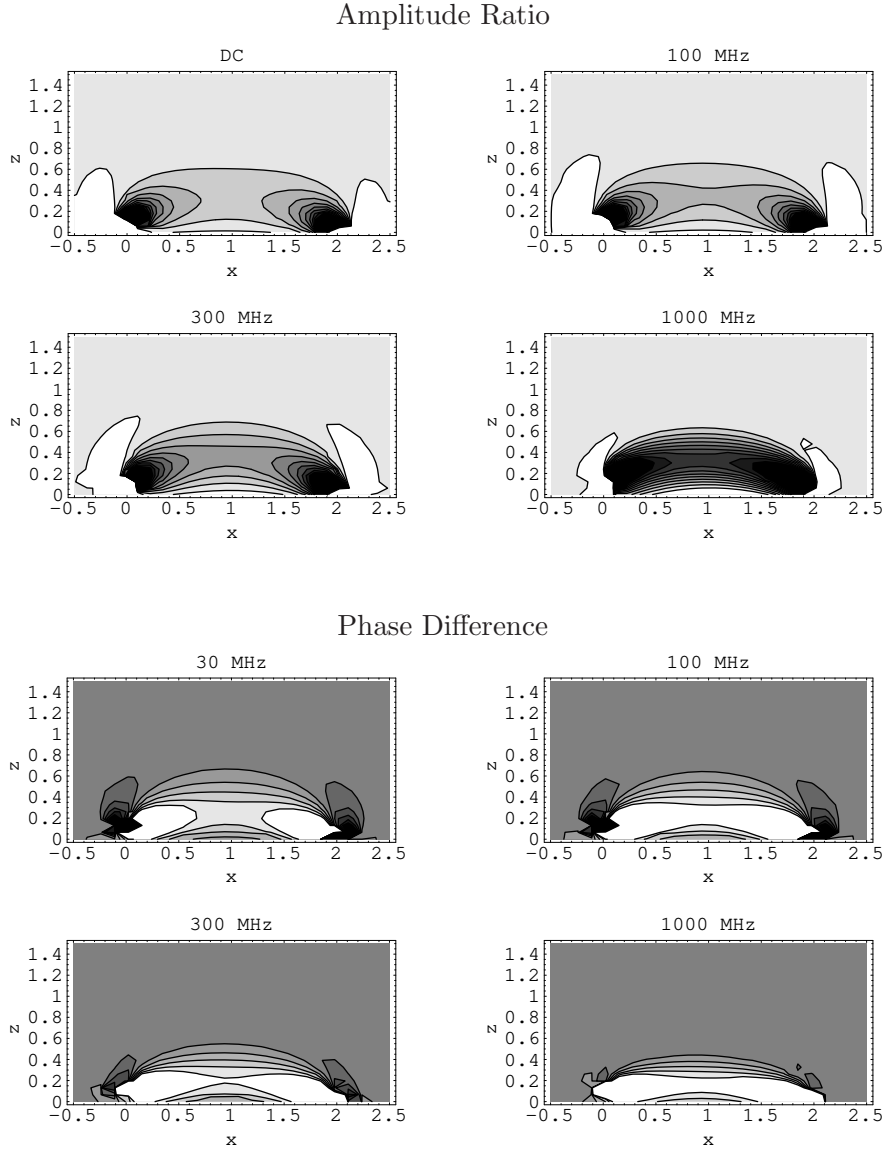
Figure 3.10: Photon bananas for scattering perturbations in the x–z–plane between source and detector (dimensions in cm), for DC light and for modulation frequencies from 30 MHz to 1 GHz. The plot range for all amplitude ratios is 0.91 to 1.01. For the phase difference the plot ranges in degree are ± 0.4 for 30 MHz, ± 1 for 100 MHz, ± 3 for 300 MHz, and ± 8 for 1 GHz.

3.3.2 Sensitivity Maps for Scattering Perturbations

To compare the effects of absorption and scattering perturbations we now consider a scattering perturbation with the same strength and size as the
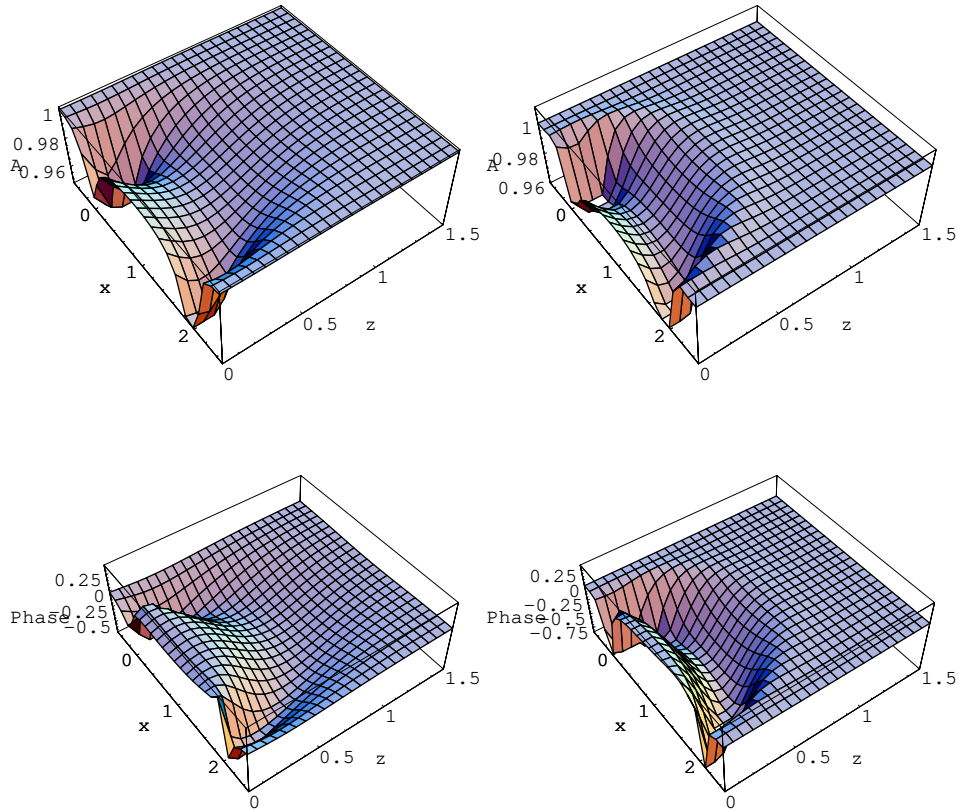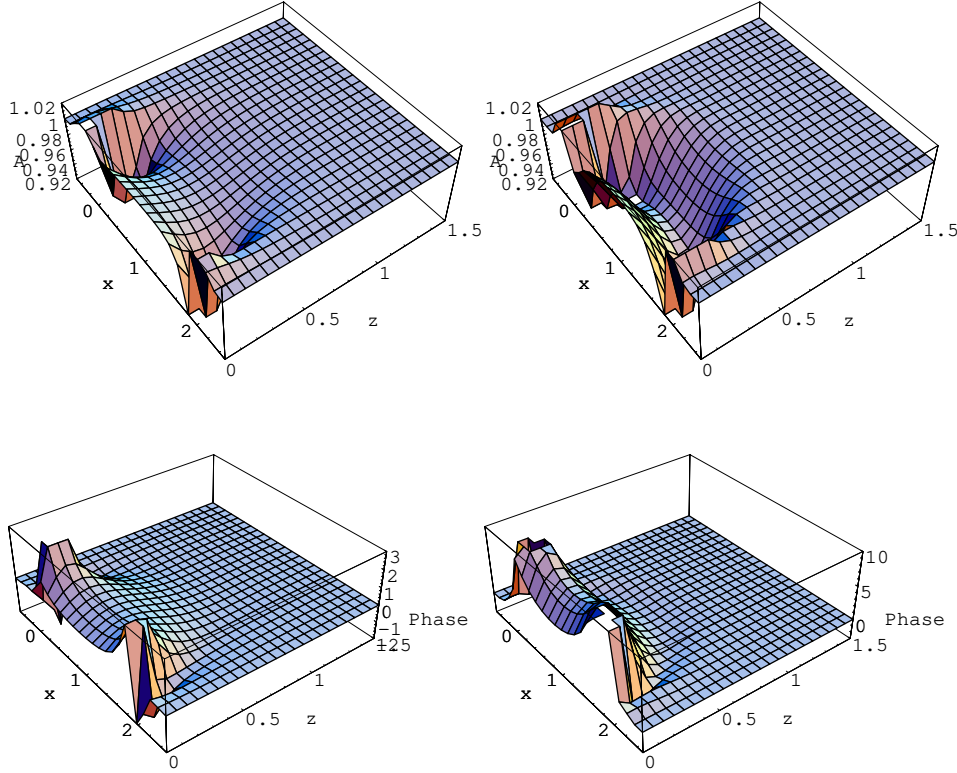
Figure 3.11: Photon bananas for scattering perturbations. Top row: amplitude ratio; bottom row: phase difference in degrees. Left column: f = 100 MHz; right column: f = 1000 MHz.

absorption perturbation in the last section, i.e. radius $a = 2$ mm and contrast ratio $\gamma = 2$, therefore $\mu'_{s1} = \gamma\mu'_{s0} = 20 \text{ cm}^{-1}$ and $\Delta\mu'_s = 10 \text{ cm}^{-1}$. Consequently, Figures 3.12 to 3.13 show sensitivity maps for the same parameters as were used for the absorption perturbation.

The sensitivity maps for scattering objects also have the typical banana shape and one might be surprised that the dipole character of the scattering perturbation (Eq. 3.19) does not cause more discrepancies. However, a closer inspection of the shape in Figs. 3.10 and 3.11 reveals several differences. Contrary to the absorption case, the sign of the phase difference is positive through-
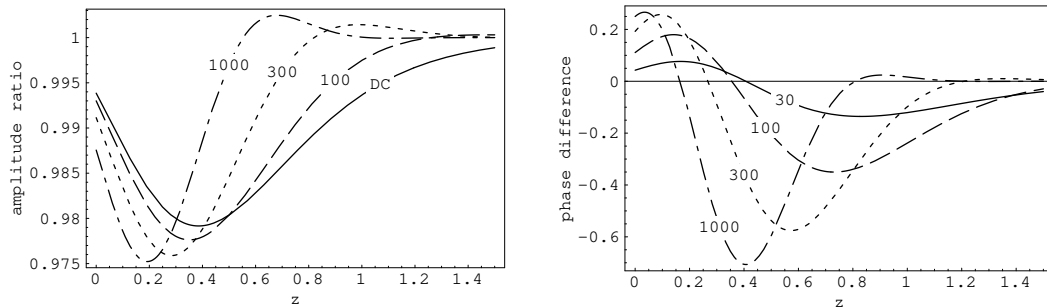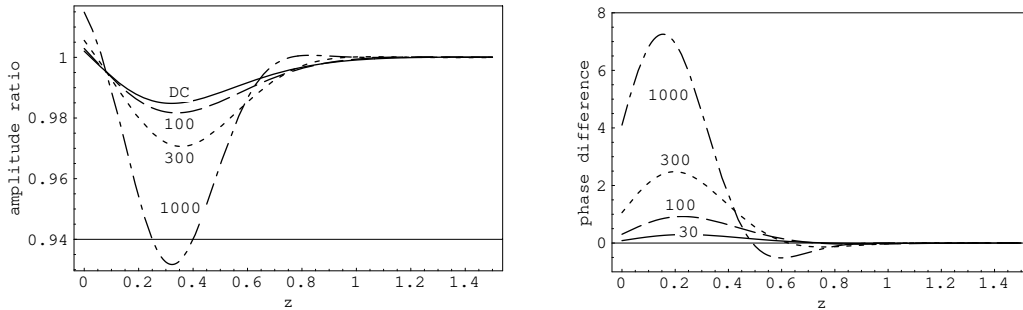
Figure 3.12: *Sensitivity for scattering perturbations versus depth half way between source and detector, i.e. on a line from (1,0,0) to (1,0,1.5).*

out the region between source and detector. This means that an increase in scattering on the relatively direct paths between source and detector always delays the photon propagation. In the sensitivity maps for amplitude ratio as well as for phase difference we see small regions of opposite sign directly besides the source and detector on the outside. These features are caused by the dipole character of the scattering perturbation. Because here the angle between $\mathbf{r} - \mathbf{r}_s$ and $\mathbf{r} - \mathbf{r}_d$ is larger than $\pi/2$ the detector sees the front lobe of the dipole perturbation, where light is scattered back into the direction of the source.

Figure 3.12 shows the behavior halfway between source and detector in more detail; compare it to Fig. 3.8 for the absorbing perturbation. We see that, contrary to the absorption case, the depth of the maximal sensitivity does not shift significantly for different modulation frequencies, but therefore the strength of the sensitivity increases drastically with the frequency. Note that for the scattering perturbation the phase delay for 1 GHz modulation frequency is about an order of magnitude higher than for an absorbing perturbation of the same relative strength.

In Fig. 3.13 the sensitivity for different source–detector distances is shown. As for the absorption case (Fig. 3.9) the sensitivity moves deeper into the
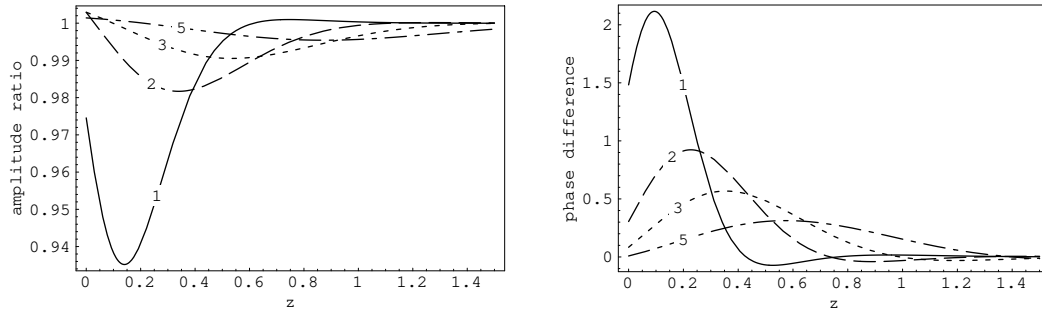
Figure 3.13:   Sensitivity for scattering perturbations, source–detector separations between 1 and 5 cm, $f = 100 MHz$.

medium for increasing source–detector separation and the strength decreases. Thus for scattering perturbations the source–detector distance determines the sampling depth, while the modulation frequency determines the strength of the sensitivity.

3.4   Design Example for Detection of Buried Absorbers

The general discussion of the sensitivity of reflection mode measurements to absorbing and scattering perturbations in the last two sections has highlighted the basic trends for variations of the source–detector separation and the modulation frequency. In this section we show how the sensitivity analysis can be utilized for the design of a detection system.

In chapter 6 we will discuss the detection of epidural and subdural brain hematomas, which are located just below the skull. We will show that the light propagation is dominated by a tunneling effect in the clear layer of cerebrospinal fluid between skull and brain and thus cannot be described by diffusion theory.

However, we expect that in cases of a local volume expansion in the brain due to intracranial bleeding, brain tumor, or edema the brain is pressed against the skull, thereby squeezing the cerebrospinal fluid out of the arachnoidea. The DC system we discuss in chapter 6 is not expected to distinguish between this situation and a bleeding because both essentially block the tunneling effect. It is therefore worth exploring frequency domain measurements for this case. Without the layer of cerebrospinal fluid the head can be approximated as an optically quasi homogeneous medium since the optical properties of the skull and the gray brain matter are very similar. In such a simplified model the task is simply to detect an increase of absorption at a fixed depth of about one centimeter.

We consider a simple system with one source and one detector. The optical properties for skull and brain are assumed to be $\mu_{a0} = 0.3$ cm^{-1} and $\mu'_{s0} = 20$ cm^{-1}. From section 3.3.1 we know that the photon banana for the phase difference penetrates deeper than that for the amplitude ratio, and is also not so strongly peaked in the vicinity of source and detector. We will therefore concentrate on phase measurements. But what are the best modulation frequency and source–detector separation? To address this issue we have plotted in Fig. 3.14 the phase difference for our standard pointlike absorbing perturbation ($a = 0.2$ cm and $\gamma = 1$), located in one centimeter depth halfway between source and detector, as a function of frequency and source–detector separation. As expected, the highest sensitivity for the phase difference occurs at large separations and at high frequencies. But this is also the region of high attenuation of the diffuse photon density waves. A low amplitude of the detector signal eventually limits the achievable phase accuracy of the system. In order to optimize this tradeoff Fig. 3.14 also shows the amplitude of the total signal (not the amplitude ratio!). More precisely, we have plotted logarithmic contours for the Green's function $\hat{G}(\mathbf{r}_s - \mathbf{r}_d, f)$ in dB, that is $10 \log_{10}(\hat{G}(\mathbf{r}_s - \mathbf{r}_d, f) \cdot [\text{cm}^2])$. Once we choose the detector aperture and size
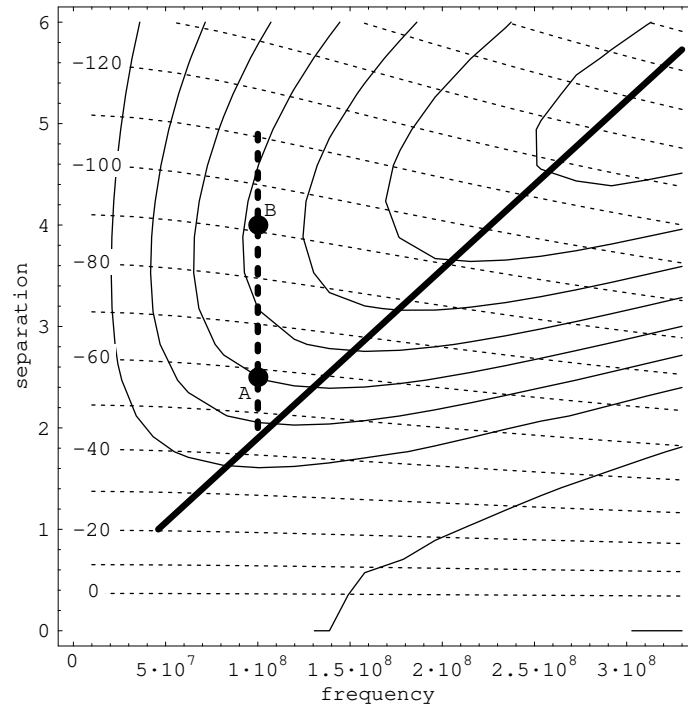
Figure 3.14: Total amplitude and phase difference for different source–detector separations in cm and modulation frequencies in Hertz. The values for the contours of the phase difference (solid lines) in degrees are marked on the right side of the frame. The dashed contours are for the logarithmic amplitude in dB, details see text.

and the source power we can use Eq. (2.36) to calculate the detector signal. In Fig. 3.14 the combinations of separation and frequency witch yield the largest phase difference with the largest detector signal are marked with a thick solid line. On first glance this line should mark the optimal parameter combinations from a signal–to–noise point of view. However, this also depends on the detection system.

Detection with normal photomultipliers like the Hamamatsu R928 is limited to about 100 MHz. Since lower frequencies bring no advantage for phase sensitivity or total amplitude we can restrict our attention to the thick dashed line in Fig. 3.14. We discuss two situations: point **A** at 100 MHz and 2.5 cm
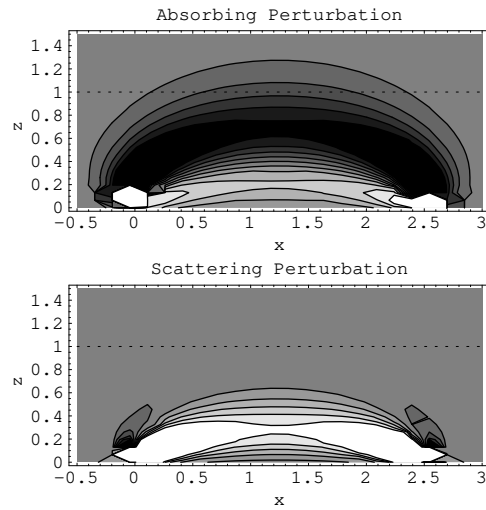
*Figure 3.15:   Sensitivity maps for parameters at point **A** in Fig. 3.14, i.e.
modulation frequency f = 100 MHz, 2.5 cm separation.*

separation close to the -60 dB contour line; and point **B** at 100 MHz and
4 cm separation close to the -90 dB contour line. One advantage of photo
multipliers is the large detection area which permits to use large optical fibers.
Using a 1000 μm diameter multimode fiber with a high numerical aperture
of $NA = 0.4$ and a 1 mW light source Eq. (2.37) in section 2.3.2.3 predicts a
detectable power of $P = \hat{G} \cdot 2.4 \cdot 10^{-6}$ [Wcm^2]. Thus the -60 dB contour line in
Fig. 3.14 corresponds to a power of 2.4 pW, which can be detected with such a
PMT with sufficient signal–to–noise ratio to make phase measurements with an
accuracy of about 0.1° [50]. Note that Fig. 3.14 shows the phase sensitivity for
a fixed depth of 1 cm, midway between source and detector. Figure 3.15 shows
the complete sensitivity maps for these parameters, for absorption changes and
scattering changes. We see that both photon bananas have their maximum
sensitivity much closer to the surface, which means that the measurement will
be rather susceptible to inhomogeneities in the sub surface layer.

Consider now point **B** with $f = 100$ MHz and 4 cm separation. Figure 3.16
shows that the photon banana for the phase difference reaches now deeper.
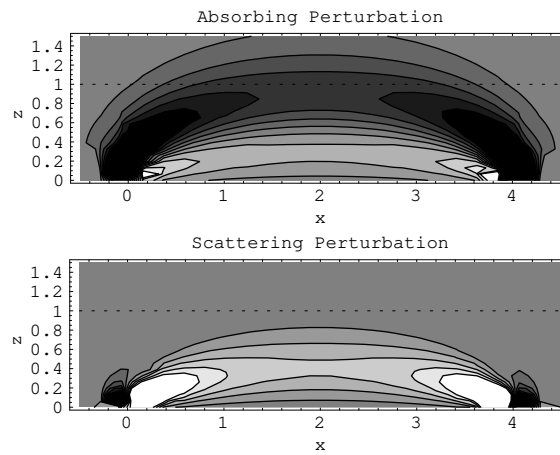
Figure 3.16:   Sensitivity maps for parameters at point **B** *in Fig. 3.14, i.e. modulation frequency* $f = 100$ *MHz, 4 cm separation.*

Additionally the increased source–detector separation gives a small gain of $0.2°$ phase difference. But the drawback is a 30 dB loss of amplitude, down to some fW of detectable power, which will reduce the phase accuracy. A further increase in source–detector separation will yield no improvement in the phase sensitivity and only marginally deeper penetration of the photon banana. Therefore we conclude that a detection system based on standard photomultipliers should use a modulation frequency of 100 MHz and a source–detector separation between 2.5 cm and 4 cm, depending on the noise of the phase detector and the expected inhomogeneities in the sub surface layer.

Chapter 4

General Perturbation Theory for Complex Extended Objects

While the multipole expansion method from the previous chapter is quite useful for the investigation of the basic properties of light propagation in inhomogeneous systems, it has a fundamental limitation: The inhomogeneity must be either of spherical geometry, or it must be so small that the higher order multipole terms, which are sensitive to the shape of the object, can be neglected. For many practical biomedical applications these restrictions render the multipole expansion approach useless because the inhomogeneities of interest, like tumors, vessel systems, hematomas, or regions of hypoxia, are neither small nor spherical.

A straightforward way to model extended objects is to divide them into small volume elements or voxels, use simple perturbation solutions for each voxel, and obtain a solution for the extended object as a sum of the contributions from all voxels. To this end, Boas *et al* [18] and Feng *et al* [51] have used limiting forms of the multipole expansion approach, similar to the result we have discussed in section 3.2.1. Barbour and Graber *et al* [52, 42] have obtained

'weight functions' based on Monte Carlo simulations. Pogue *et al* [53], Kaschke *et al* [46], and Arridge *et al* [54] have used direct Green's function approaches. O'Leary *et al* [55] have used an approximated integral approach. Only [54, 55, 18] treat scattering objects correctly.

All these approaches, however, have a fundamental limitation: they linearize the problem, i.e. they neglect the interaction of objects or, for large objects, of different parts of the objects. They are therefore not suited for extended inhomogeneities with stronger perturbations.

The objective of this chapter is to overcome these limitations and to develop a comprehensive and coherent theory for diffuse light transport in heterogeneous turbid media, based on an integral perturbation approach. The theory covers steady state and modulated light, is applicable to absorbing and scattering inhomogeneities of arbitrary size and shape, and accounts for the nonlinear interaction between inhomogeneities. We have developed and used the theory in [56, 57, 58, 59, 60], this and the next chapter are based on - and extend beyond - these publications.

In section 4.1 we give a rigorous derivation of the integral formulation of the optical diffusion equation starting from the differential formulation. Thereby we introduce the virtual source formalism, which is a conceptually simple yet powerful tool. For one, it establishes the framework for a very versatile iterative numerical perturbation method. We sketch the iterative solution only briefly in section 4.2 and postpone the detailed discussion to the next chapter. But, equally important, the virtual source formalism also facilitates an intuitive and deep insight into the nature of light propagation in heterogeneous systems. We therefore devote the remainder of this chapter to the discussion of the virtual source formalism. In section 4.3 we specialize on sharply bounded objects and in section 4.4 this special case is used to discuss the principal behavior of scattering and absorption perturbations. In section 4.5 we develop the limiting

form of the virtual source formalism for small and weak perturbations. This permits us to draw a connection to the multipole approach from the previous chapter as well as to the first order approximations which are the basis for an important class of inverse algorithms [55]. In section 4.6 we use the virtual source formalism to show that weak scattering and absorption perturbations can be ambiguous and may result in the same light field. We draw conclusions for the source and detector placement in inverse problems.

4.1 The Virtual Source Formalism

We recall the frequency dependent diffusion equation (2.14) for an inhomogeneous medium from section 2.3:

$$\boldsymbol{\nabla} D(\mathbf{r}) \cdot \boldsymbol{\nabla}\phi(\mathbf{r},\omega) + D(\mathbf{r})\nabla^2\phi(\mathbf{r},\omega) - \mu_a(\mathbf{r})\,\phi(\mathbf{r},\omega) + \frac{i\omega}{c(\mathbf{r})}\,\phi(\mathbf{r},\omega) = -S_0(\mathbf{r},\omega). \tag{4.1}$$

For a homogeneous medium the first term vanishes because $D = D_0$ is constant and we get the homogeneous diffusion equation

$$D_0\nabla^2\phi(\mathbf{r}) - \mu_{a0}\phi(\mathbf{r}) + \frac{i\omega}{c}\phi(\mathbf{r}) = -S(\mathbf{r}). \tag{4.2}$$

We will show below that this term determines the dipole-like perturbation that dominates the effect of small scattering perturbations. Therefore any perturbation theory that starts with homogeneous diffusion equation cannot describe scattering objects.

In the following we will drop $(\mathbf{r})$ in the formulas and implicitly assume that all quantities vary spatially, unless otherwise noted. It is advantageous to reformulate Eq. (4.1) in terms of the net flux vector $\mathbf{J} = -D\boldsymbol{\nabla}\phi$ and the reduced scattering coefficient $\mu'_s = 1/(3D)$. We also employ the definition of the square of the wave number $k^2 = -3\mu'_s(\mu_a - i\omega/c)$ to obtain

$$3\boldsymbol{\nabla}\mu'_s \cdot \mathbf{J} + \nabla^2\phi + k^2\phi = -3\mu'_s S. \tag{4.3}$$

The advantage of using the net flux $\mathbf{J}$ instead of the gradient of the fluence is that the net flux is continuous at boundaries between different media while $\boldsymbol{\nabla}\phi$ is not. This will be helpful for the discussion of objects with sharp boundaries in section 4.3.

To separate the effect of the objects from that of the background medium the optical properties are written as $\mu_a = \mu_{a0} + \Delta\mu_a$ and $\mu'_s = \mu'_{s0} + \Delta\mu'_s$, where μ_{a0} and μ'_{s0} are the constant parts due to the background medium, and $\Delta\mu_a$ and $\Delta\mu'_s$ are the absorption and scattering perturbations due to the objects. With this we write $k^2 = k_0^2 + \Delta k^2$, where

$$k_0^2 = -3\mu'_{s0}(\mu_{a0} - \frac{i\omega}{c}), \tag{4.4}$$

$$\Delta k^2 = -3(\Delta\mu_a\mu'_{s0} + \Delta\mu'_s(\mu_{a0} - i\omega/c) + \Delta\mu_a\Delta\mu'_s), \tag{4.5}$$

and extract the Helmholtz operator of the background medium, $(\nabla^2 + k_0^2)$, to obtain:

$$(\nabla^2 + k_0^2)\phi = -3\mu'_s S - 3\boldsymbol{\nabla}\mu'_s \cdot \mathbf{J} - \Delta k^2 \phi. \tag{4.6}$$

We rewrite this as

$$(\nabla^2 + k_0^2)\phi = -3\mu'_{s0}\left(\frac{\mu'_s}{\mu'_{s0}}S + S^{Virt}[\phi]\right), \tag{4.7}$$

where the virtual source density $S^{Virt}[\phi]$ is defined as,

$$S^{Virt}[\phi] = S_\phi^{Virt} + S_\mathbf{J}^{Virt} \tag{4.8}$$

$$S_\phi^{Virt} = \frac{1}{3\mu'_{s0}}\Delta k^2 \phi, \tag{4.9}$$

$$S_\mathbf{J}^{Virt} = \frac{\boldsymbol{\nabla}\mu'_s}{\mu'_{s0}} \cdot \mathbf{J}, \tag{4.10}$$

which depends on both the fluence and its gradient, since $\mathbf{J} = -D\boldsymbol{\nabla}\phi$.

In this form we can see how the presence of the objects affects the light field. The strength of the real source density S is scaled according to the actual optical properties at its location. Note that in the common case where S is

located entirely in the background medium its strength remains unchanged. Additionally, the objects cause a virtual source density $S^{Virt}[\phi]$ that depends on the optical properties of the objects and the light field at the objects.

We now change to the integral formulation. With Green's vector theorem [37], Eq. (4.7) can be transformed into an equivalent integral equation,

$$\phi(\mathbf{r}) = \phi_0(\mathbf{r}) + \phi^{Pert}(\mathbf{r}), \tag{4.11}$$

$$\phi_0(\mathbf{r}) = \int_{V_s} d\mathbf{r}' \, (\mu_s'(\mathbf{r}')/\mu_{s0}') \, S(\mathbf{r}') \, \hat{G}(|\mathbf{r} - \mathbf{r}'|), \tag{4.12}$$

$$\phi^{Pert}(\mathbf{r}) = \int_{V_{obj}} d\mathbf{r}' \, S^{Virt}[\phi(\mathbf{r}')] \, \hat{G}(|\mathbf{r} - \mathbf{r}'|) \tag{4.13}$$

$$= \int_{V_{obj}} d\mathbf{r}' \, \left(\frac{1}{3\mu_{s0}'} \Delta k^2 \phi(\mathbf{r}') + \frac{\boldsymbol{\nabla}\mu_s'}{\mu_{s0}'} \cdot \mathbf{J}(\mathbf{r}') \right) \hat{G}(|\mathbf{r} - \mathbf{r}'|),$$

where $\hat{G}(|\mathbf{r} - \mathbf{r}'|) = 3\mu_{s0}' G(|\mathbf{r} - \mathbf{r}'|)$ is the impulse response to a physical point source and $G(|\mathbf{r} - \mathbf{r}'|) = \exp(ik_0 |\mathbf{r} - \mathbf{r}'|)/(4\pi |\mathbf{r} - \mathbf{r}'|)$ is the Green's function of the Helmholtz equation for the background medium, see Eqs. (2.18, 2.19). ϕ_0 is a convolution of the scaled real source density with the impulse response. If the volume V_s of the source density is located entirely in the background medium, ϕ_0 becomes the *background fluence*, that is the fluence in the homogeneous background medium without objects. The perturbation fluence ϕ^{Pert} is a convolution integral of similar form. The virtual source density $S^{Virt}[\phi]$ contributes to the light field like the real source density S, but its strength in turn depends on the light field within the objects. Once $S^{Virt}[\phi]$ is determined by solving the integral equation inside the objects, the light field at an arbitrary position, inside or outside the objects, can be calculated as a simple integration over the virtual and real source densities. Due to the fundamental role of the virtual source density we will refer to this approach as the virtual source formalism.

While the transformation of the differential equation into an integral equation by itself does not solve the problem, the virtual source formalism is the ap-

propriate form for a perturbation approach. In the following section we will briefly outline how the integral equation can be solved iteratively, but a detailed description of the numerical implementation is postponed to chapter 5. Once we principally know how to obtain a solution we will use the virtual source formalism to discuss the basic properties of the solution.

4.2 Iterative Solution and Born Approximation

Formally, the integral equation of the virtual source formalism (4.11–4.13) is a Fredholm equation of the second kind in three dimensions. It can be solved with the iterative approach of successive approximation [37]. The first order approximation ϕ_1 is obtained by using the background solution ϕ_0 to calculate the perturbation integral in Eq. (4.13), which yields:

$$
\begin{aligned}
\phi_1(\mathbf{r}) &= \phi_0(\mathbf{r}) + \int_{V_{obj}} d\mathbf{r}' S^{Virt}[\phi_0(\mathbf{r}')] \, \hat{G}(|\mathbf{r} - \mathbf{r}'|) \\
&= \phi_0(\mathbf{r}) + \int_{V_{obj}} d\mathbf{r}' \left(\frac{1}{3\mu'_{s0}} \Delta k^2 \phi_0(\mathbf{r}') + \frac{\boldsymbol{\nabla}\mu'_s}{\mu'_{s0}} \cdot \mathbf{J}_0(\mathbf{r}') \right) \hat{G}(|\mathbf{r} - \mathbf{r}'|).
\end{aligned}
\tag{4.14}
$$

This is known as the Born approximation. Some imaging reconstruction schemes [55, 61] are based on the inversion of a different formulation of this equation, which we will discuss in section 4.5. The second order is calculated by using ϕ_1 in the perturbation integral, etc., which leads to the general recursion formula

$$
\phi_n(\mathbf{r}) = \phi_0(\mathbf{r}) + \int_{V_{obj}} d\mathbf{r}' \, S^{Virt}[\phi_{n-1}(\mathbf{r}')] \, \hat{G}(|\mathbf{r} - \mathbf{r}'|).
\tag{4.15}
$$

By repeated application of this equation to itself one can transform it into a Neumann series [37]

$$
\phi_n = \phi_0 + \int dV \hat{G} S^{Virt} \phi_0 + \int dV \hat{G} S^{Virt} \int dV \hat{G} S^{Virt} \phi_0
$$

$$+ \cdots + \left[\int dV \hat{G} S^{Virt} \right]^n \phi_0, \qquad (4.16)$$

where we have used a shorthand notation where the integration as well as S^{Virt} have to be understood as operators acting on everything on their right hand side. However, for numerical evaluation (chapter 5) we prefer the recursive form.

4.3   Sharp Boundaries

Objects with sharp boundaries are a special but important case. Compared with a typical length scale of resolution in imaging of a few millimeters, blood vessels, bones, hematoma, some tumors, and most inclusions in tissue phantoms can be considered as sharply bounded. Both the integral and the differential formulation given so far rely on a smoothly varying reduced scattering coefficient μ_s', because they contain $\boldsymbol{\nabla}\mu_s'$ in the term $S_{\mathbf{J}}^{Virt}$ (Eq. 4.10). If objects have sharp boundaries the reduced scattering coefficient μ_s' is discontinuous at their surface and $\boldsymbol{\nabla}\mu_s'(\mathbf{r}_{surf})$ has a singularity. In the differential formulation, the boundary conditions of continuous fluence and net flux have to be applied at the surfaces and solved together with the diffusion equation. The integral formulation requires no additional boundary conditions. At the surface of a sharp object, $\boldsymbol{\nabla}\mu_s'(\mathbf{r}) = -\Delta\mu_s'(\mathbf{r})\,\mathbf{n}(\mathbf{r})\,\delta(\mathbf{r} - \mathbf{r}_{surf})$, where δ is Dirac's delta function and $\mathbf{n}$ is the outward pointing surface normal vector. This transforms the volume integral (Eq. 4.13) over $S_{\mathbf{J}}^{Virt}$ (Eq. 4.10) into a sum of an integral over the inner part of the volume $V_{obj-inside}$ where $\mu_s'(\mathbf{r})$ is smooth, and a surface integral over the sharp transition:

$$\frac{1}{\mu_{s0}'} \int_{V_{obj}} d\mathbf{r}' \boldsymbol{\nabla}\mu_s'(\mathbf{r}')\mathbf{J}(\mathbf{r}')\hat{G}(|\mathbf{r} - \mathbf{r}'|)$$

$$\rightarrow \quad \frac{1}{\mu_{s0}'} \int_{V_{obj-inside}} d\mathbf{r}' \boldsymbol{\nabla}\mu_s'(\mathbf{r}')\mathbf{J}(\mathbf{r}')\hat{\mathbf{G}}(|\mathbf{r} - \mathbf{r}'|)$$

$$- \frac{1}{\mu'_{s0}} \int\limits_{S_{obj}} dA' \Delta\mu'_s(\mathbf{r}')\mathbf{n}(\mathbf{r}') \cdot \mathbf{J}(\mathbf{r}')\hat{G}(|\mathbf{r} - \mathbf{r}'|). \tag{4.17}$$

In the following discussion we will consider only sharply bounded objects with constant optical properties inside, for which the volume integral over $\boldsymbol{\nabla}\mu'_s\mathbf{J}$ vanishes. For these objects the different effects of scattering and absorbing perturbations are most pronounced and easy to interpret. With these simplifications Eqs. (4.8–4.10, 4.13) become

$$\begin{aligned}
\phi^{Pert}(\mathbf{r}) &= -\frac{\Delta\mu'_s}{\mu'_{s0}} \int\limits_{S_{obj}} d\mathbf{A}' \cdot \mathbf{J}(\mathbf{r}')\hat{G}(|\mathbf{r} - \mathbf{r}'|) \\
&\quad - \left(\Delta\mu_a + \Delta\mu'_s \frac{\mu_{a0} - i\omega/c}{\mu'_{s0}} + \frac{\Delta\mu_a\Delta\mu'_s}{\mu'_{s0}} \right) \\
&\quad \times \int\limits_{V_{obj}} d\mathbf{r}' \phi(\mathbf{r}')\hat{G}(|\mathbf{r} - \mathbf{r}'|).
\end{aligned} \tag{4.18}$$

Note that if $\Delta\mu_a$ or $\Delta\mu'_s$ are small compared to the background value the mixed term, $\Delta\mu_a\Delta\mu'_s/\mu'_{s0}$, can be neglected and absorption and scattering perturbations are approximately additive.

4.4   Scattering and Absorbing Inhomogeneities

To discuss the basic effects of scattering and absorption changes we investigate the importance of the contributions from the surface and volume integrals. We compare a scattering and an absorbing perturbation with the same relative change ζ in scattering ($\Delta\mu'_s = \zeta\mu'_{s0}$, $\Delta\mu_a = 0$) or absorption ($\Delta\mu_a = \zeta\mu_{a0}$, $\Delta\mu'_s = 0$). For the absorbing perturbation Eq. (4.18) simplifies to:

$$\phi^{Pert} = -\zeta\mu_{a0} \int\limits_V dV \phi\hat{G}, \tag{4.19}$$

for the scattering perturbation to:

$$\phi^{Pert} = -\zeta \int\limits_S d\mathbf{A} \cdot \mathbf{J}\hat{G} \ - \ \zeta(\mu_{a0} - i\omega/c) \int\limits_V dV \phi\hat{G}. \tag{4.20}$$
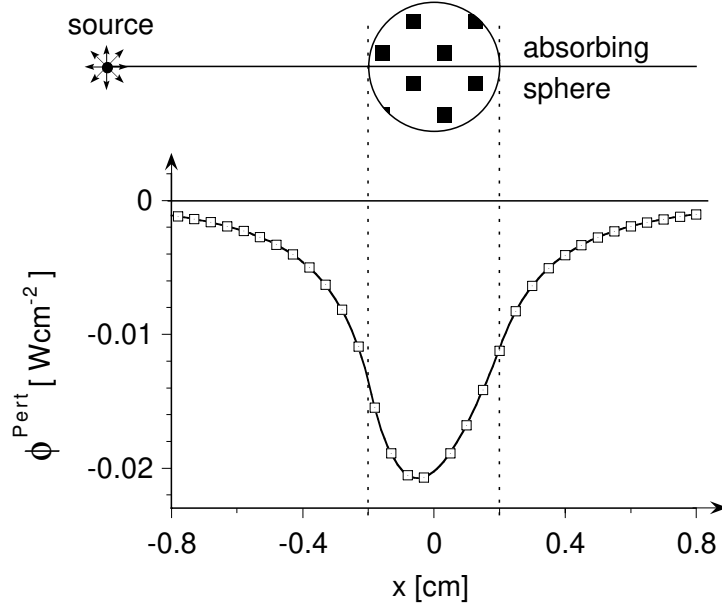
Figure 4.1:   Perturbation of the diffuse light field in an infinite background medium, caused by the doubled absorption in a sphere, calculated on a line through point source and sphere. For comparison, results from the analytical solution (section 3.1) are marked with symbols. (Sphere: radius = 0.2 cm, 739 voxels, $\mu_a = 0.2$ cm^{-1}, $\mu'_s = 10$ cm^{-1}; background medium: $\mu_a = 0.1$ cm^{-1}, $\mu'_s = 10$ cm^{-1}; point source at $x = -1$ cm; $S = 1$ W.)

The result is shown in Fig. 4.1 for a sphere with doubled absorption ($\zeta = 1$) and in Fig. 4.2 for a sphere with doubled scattering relative to the background medium, which has typical optical properties of biological tissues in the NIR wavelength region. We chose unmodulated (DC) light because plots of the real DC fluence yield a better understanding of the surface effect than the amplitude of the AC fluence.

For the absorption change the volume integral causes a monopole pattern. The virtual source density reduces to $S^{Virt}[\phi] = -\Delta\mu_a\phi$, thus an increase in absorption simply depletes the light field as expected.

For the object with scattering change both the volume integral and the surface
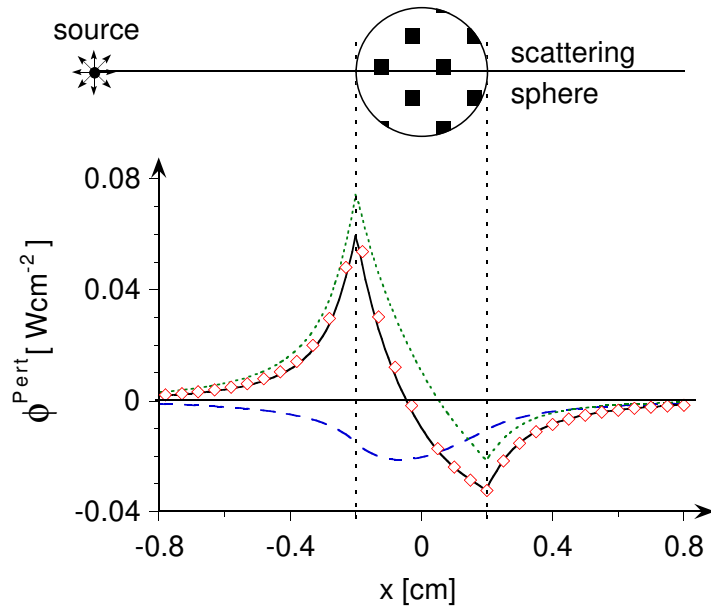
Figure 4.2:   Perturbation fluence from a sphere with increased scattering. Same as Fig. 4.1, but the sphere has doubled scattering: $\mu_a = 0.1\ cm^{-1}$, $\mu'_s = 20\ cm^{-1}$. The total fluence perturbation ϕ^{Pert} (solid line) is now a sum of the contributions from the surface integral (dotted line) and the volume integral (dashed line) in Eq. (4.18).

integral are important. It is remarkable that for DC light the volume integral is the same as for an absorption perturbation with the same relative strength. Why should an increase in scattering cause an absorption effect? The reason is simply that because of the increased scattering the photons which enter the object travel a longer path inside the object before they leave and therefore have a higher chance to be absorbed. Thus the scattering enhances the effect of the absorption and the contribution from the volume integral can be described as volume-induced scattering-enhanced absorption. In the surface integral the dot product $d\mathbf{A}' \cdot \mathbf{J}(\mathbf{r}')$ yields a distribution of virtual surface sources with positive virtual sources on the side near to the point source and negative virtual sources on the far side. This contribution can be described as surface-induced back-scattering. However, because the magnitude of the net flux vector drops quickly with increasing distance from the point source,

the virtual surface sources on the far side are considerably weaker than those on the front. In Fig. 4.2 we have chosen an intermediate object size. In the limit of a small sphere the surface-to-volume ratio is high, thus the surface-induced back scattering dominates and ϕ^{Pert} approaches a dipole field [51]. For large objects the surface-to-volume ratio is low, thus the volume-induced scattering-enhanced absorption dominates. For comparison, we also plotted the analytical solution from section 3.1 in Figs. 4.1 and 4.2. The agreement is excellent.

We note that the definition of the diffusion coefficient D has an interesting consequence for the qualitative effects of absorbing perturbations. In our paper [56] we still used the old and inaccurate definition $\tilde{D} = 1/(3(\mu_a + \mu'_s))$ instead of the correct $D = 1/(3\mu'_s)$ (see the paragraph around Eq. (2.13) on page 16). The equivalent for Eq. (4.19) for absorbing perturbations is equation (16) in that paper. It has a contribution from a surface integral just like in Eq. (4.20). We had shown that this surface contribution was by a factor μ_{a0}/μ'_{s0} smaller than the volume contribution and was thus negligible in the strong scattering regime. It is satisfying that the use of the correct diffusion coefficient simplifies the formalism and makes the fundamental difference between scattering and absorbing perturbations even more obvious.

4.5   Weak and Small Perturbations

We have now two complementary approaches to describe inhomogeneities: the virtual source formalism derived in the last sections, and the multipole expansion from chapter 3. In this section we show that in the limiting case of small and weak perturbations both approaches are equivalent, and then we compare them. To prove the equivalence we have to transform the integral over the virtual source density for the scattering perturbation $S_{\mathbf{J}}^{Virt}$ with Green's

first identity. It is possible to do this for the case of arbitrary and especially smooth distributions of the scattering coefficient [50]. Here we follow a different approach and start from the integral equation for sharply bounded objects Eq. (4.18) because this yields the same result with less effort.

Consider the perturbed fluence for sharply bounded objects in Eq. (4.18). For weak perturbations we can use the Born approximation, i.e. use the unperturbed background fluence in the integral, and with $\mathbf{J}_0 = -1/(3\mu'_{s0})\,\boldsymbol{\nabla}\phi_0$ we obtain

$$
\begin{aligned}
\phi^{Pert}(\mathbf{r}) \;=\; & \frac{\Delta\mu'_s}{3\mu'^2_{s0}} \int\limits_{S_{obj}} d\mathbf{A}' \cdot \boldsymbol{\nabla}\phi_0(\mathbf{r}')\hat{G}(|\mathbf{r}-\mathbf{r}'|) \\
& - \left(\Delta\mu_a + \Delta\mu'_s\frac{\mu_{a0}-i\omega/c}{\mu'_{s0}} + \frac{\Delta\mu_a\Delta\mu'_s}{\mu'_{s0}}\right) \\
& \times \int\limits_{V_{obj}} d\mathbf{r}'\phi_0(\mathbf{r}')\hat{G}(|\mathbf{r}-\mathbf{r}'|).
\end{aligned}
\tag{4.21}
$$

The surface integral in this equation can be transformed into volume integrals with Green's first identity. This yields a term $\nabla^2\phi_0$ which can be transformed according to the homogeneous Helmholtz equation $\nabla^2\phi_0 = -k_0^2\phi_0$, and furthermore with $-k_0^2/(3\mu'_{s0}) = \mu_{a0} - i\omega/c$. Note that for these two steps it is essential to use the Born approximation in Eq. (4.21). The surface integral then becomes

$$
\frac{\Delta\mu'_s}{3\mu'^2_{s0}} \int\limits_{S_{obj}} d\mathbf{A}' \cdot \boldsymbol{\nabla}\phi_0\hat{G} \;=\; \Delta\mu'_s\frac{\mu_{a0}-i\omega/c}{\mu'_{s0}} \int\limits_{V_{obj}} d\mathbf{r}'\,\phi_0\hat{G} \;+\; \frac{\Delta\mu'_s}{3\mu'^2_{s0}} \int\limits_{V_{obj}} d\mathbf{r}'\,\boldsymbol{\nabla}\phi_0\cdot\boldsymbol{\nabla}\hat{G}.
\tag{4.22}
$$

Inserting Eq. (4.22) in Eq. (4.21) we notice that the first volume integral on the right hand side of Eq. (4.22) cancels with one in Eq. (4.21), so that we finally have:

$$
\begin{aligned}
\phi^{Pert}(\mathbf{r}) \;=\; & \frac{\Delta\mu'_s}{3\mu'^2_{s0}} \int\limits_{V_{obj}} d\mathbf{r}'\boldsymbol{\nabla}\phi_0(\mathbf{r}') \cdot \boldsymbol{\nabla}\hat{G}(|\mathbf{r}-\mathbf{r}'|) \\
& - \left(\Delta\mu_a + \frac{\Delta\mu_a\Delta\mu'_s}{\mu'_{s0}}\right) \int\limits_{V_{obj}} d\mathbf{r}'\phi_0(\mathbf{r}')\hat{G}(|\mathbf{r}-\mathbf{r}'|).
\end{aligned}
\tag{4.23}
$$

In order to make a direct connection to the multipole approach from chapter 3 we explicitly have to assume that the scattering change is small, that is $\Delta\mu'_s \ll \mu'_{s0}$. Then the mixed term with $\Delta\mu'_s\,\Delta\mu_a$ in Eq. (4.23) can be neglected:

$$\phi^{Pert}(\mathbf{r}) = \frac{\Delta\mu'_s}{3\mu'^2_{s0}} \int\limits_{V_{obj}} d\mathbf{r}'\boldsymbol{\nabla}\phi_0(\mathbf{r}') \cdot \boldsymbol{\nabla}\hat{G}(|\mathbf{r}-\mathbf{r}'|)$$

$$- \Delta\mu_a \int\limits_{V_{obj}} d\mathbf{r}'\phi_0(\mathbf{r}')\hat{G}(|\mathbf{r}-\mathbf{r}'|). \qquad (4.24)$$

For simplicity we will refer to this formulation as the $\boldsymbol{\nabla}\hat{G}$–approach. Note that this assumption is even more restrictive than the assumption that the Born approximation holds, i.e. that the perturbed fluence does not differ too much from the unperturbed fluence. If we additionally focus on small objects we can approximate the integral and consequently Eq. (4.24) becomes

$$\phi^{Pert}(\mathbf{r}) = \frac{\Delta\mu'_s}{3\mu'^2_{s0}}V_{obj}\boldsymbol{\nabla}\phi_0(\mathbf{r}') \cdot \boldsymbol{\nabla}\hat{G}(|\mathbf{r}-\mathbf{r}'|) - \Delta\mu_a V_{obj}\phi_0(\mathbf{r}')\hat{G}(|\mathbf{r}-\mathbf{r}'|). \quad (4.25)$$

For comparison consider now the limiting form of the multipole expansion for small and weak perturbations Eq. (3.15) in chapter 3 on page 33. In the limit $\Delta\mu'_s \ll \mu'_{s0}$ Eq. (3.15) becomes identical to Eq. (4.25). Thus the $\boldsymbol{\nabla}\hat{G}$–approach can be understood as a method to extend the limiting form of the multipole approach to extended objects. A large object is simply modeled with many small volume elements for which the limiting form of the multipole expansion hold.

An advantage of the $\boldsymbol{\nabla}\hat{G}$–approach is that it yields a simple *linear* dependence in the perturbations $\Delta\mu'_s$ and $\Delta\mu_a$. For this reason it has been used as the basis for some inverse algorithms in optical tomography [55].

The most important disadvantage of the $\boldsymbol{\nabla}\hat{G}$–approach from a practical point of view is that it is based on the Born approximation. As a consequence it cannot be used to obtain higher order approximations with the method of successive approximation. An attempt to repeat the derivation from Eq. (4.21)

to Eq. (4.22) for higher orders leads to awkward results[1] with no practical use. This severely limits the application of the $\boldsymbol{\nabla}\hat{G}$–approach as a forward algorithm, because it is limited to the Born approximation, while stronger perturbations *need* to be modeled with higher orders.

A disadvantage of more philosophical nature but – in our opinion – equal importance is that the $\boldsymbol{\nabla}\hat{G}$–approach does not facilitate the physical interpretation of extended scattering perturbations as well as the virtual source formalism. From the first integral in Eq. (4.24) it is not immediately obvious that the perturbation caused by a scattering change has a sharp peak at the front and back surface. Of course one can understand this by noting that the dipoles in the volume will almost cancel each other and leave 'free' dipoles at the surface. But this means essentially to mentally apply Green's first identity to arrive at the virtual source concept. Therefore we believe it is more convenient to directly use the virtual source formalism. Another drawback of the $\boldsymbol{\nabla}\hat{G}$–approach is that the effect of the scattering perturbation is propagated to the detector position $\mathbf{r}$ not by the Green's function, but by the gradient of the Green's function. Thus absorbing and scattering perturbations cannot be compared directly, because of the different $\mathbf{r}$–dependence of the Green's function and its gradient.

4.6   Ambiguity of Scattering and Absorption

In this section we will discuss an ambiguity of scattering and absorption perturbations which is of special importance for imaging applications with DC or low-frequency modulated light. Typical source and detector configurations in inverse problems are shown in Fig. 4.3. A general strategy is to distribute

---

[1] The reason is that without the Born approximation the $\nabla^2\phi$–term cannot be transformed with the help of the homogeneous diffusion equation.
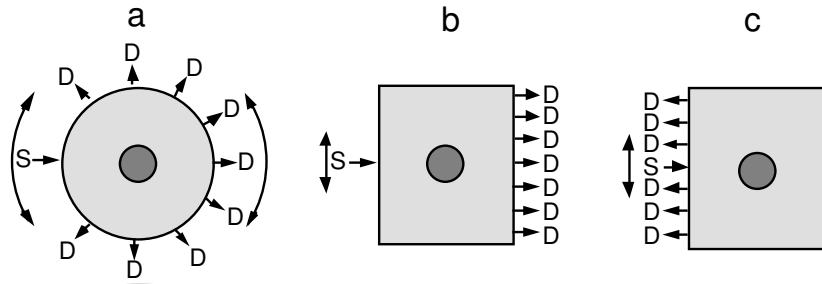
Figure 4.3: Measurement configurations for imaging.

sources and detectors as widely as the accessible surface of the sample allows. Practical considerations will, however, limit the number and placement of sources and detectors. It is therefore important to explore the impact of different configurations. As an example, researchers have successfully used phased arrays of few sources and detectors [62] to simplify object localization. Although frequency domain measurements are superior to DC measurements because of the additional phase information, the simplicity and low cost of the equipment makes DC measurements attractive [45].

To discuss the ambiguity we will use the virtual source formalism because, contrary to the $\boldsymbol{\nabla}\hat{G}$–approach from the last section, the virtual source formalism is well suited to treat absorbing and scattering perturbations simultaneously. The reason is that both absorbing and scattering perturbations simply yield a distribution of virtual sources. After the virtual sources are obtained it is unimportant whether they were caused by a scattering or an absorbing perturbation, because the perturbation light field is then generated by means of the Green's function in the same way as for normal real light sources.

If the modulation frequency is low enough ($\omega \ll c\mu_{a0}$) the imaginary part of the Δk^2 term (see Eq.(4.4) on page 60) can be neglected. Our proposition is that for a fixed source position, a scattering perturbation and an absorp-

tion perturbation can both yield the same virtual source distribution. Since the virtual source distribution determines the perturbation fluence completely, both situations are principally indistinguishable.

To illustrate this, we construct an example for the DC case, see Fig. 4.4. We choose a rectangular object for numerical reasons because it is easier to represent in a Cartesian voxel grid than a sphere. In this way we can rule out errors due to a volume mismatch between the real and the discretized object. The scattering object **i** in Fig. 4.4a is a 1x1x1 cm^3 cube with increased scattering $\mu'_s = 12$ cm^{-1} but the same absorption as the background medium ($\mu_{a0} = 0.1$ cm^{-1}, $\mu'_{s0} = 10$ cm^{-1}). The corresponding virtual source distribution consists of a negative volume part which is spread over the cube, a positive surface part on the front of the cube, and a smaller surface part on the back. The resulting perturbation due to the scattering cube is shown as solid curve in Fig. 4.4c.

To mimic the virtual source distribution of the scattering cube with an absorbing perturbation (Fig. 4.4b) we model the volume distribution with a cube **i** with increased absorption $\mu_a = 0.12$ cm^{-1}, the front surface part with a 0.1 cm thick slab **ii** with decreased absorption $\mu_a = 0.002$ cm^{-1}, and the back surface part with a 0.1 cm thick slab **iii** with increased absorption $\mu_a = 0.26$ cm^{-1}. The scattering is the same as in the background. The resulting perturbation fluence is shown as dashed curve in Fig. 4.4c. It differs slightly from the one for the scattering perturbation because the equivalent absorber distribution is actually more complicated than the simple three object model we used. Note also that this scheme does not work for strong perturbations. The front virtual surface source distribution has to be mimicked with a region of decreased absorption. The constraint that $\Delta\mu_a$ cannot be smaller than $-\mu_a$ puts a limitation on the maximal accessible scattering perturbation that can be mimicked.

To distinguish between weak absorption and scattering perturbations with DC
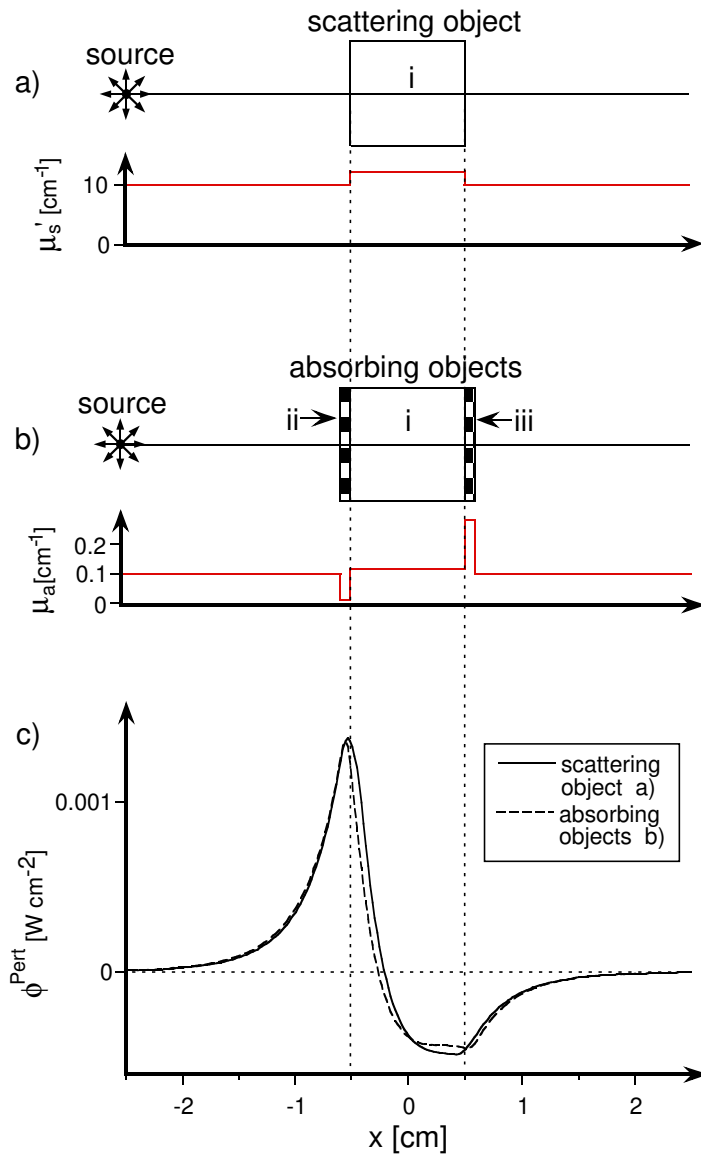
*Figure 4.4: Ambiguity between scattering and absorbing inhomogeneities for DC light. a): Scattering cube with increased scattering but the same absorption than the background medium. b): The equivalent absorbing object is composed of the cube **i** with increased absorption, a thin slab **ii** with decreased absorption on the front side of **i**, and a thin slab **iii** with increased absorption on the back side. For both situations: 1 W source at x = -2.5 cm, voxel length 1 mm. c): The perturbation for the scattering (solid curve) and the absorbing inhomogeneities (dashed curve).*

or low- frequency modulated light, it is necessary to take measurements with different source positions in order to shift the position of the virtual surface sources. This is easily achieved in applications like breast and brain imaging where a measurement configuration like Fig. 4.3a allows for maximal flexibility. Even in more restricted transmission measurements (Fig. 4.3b), i.e. in prostrate imaging between urethra and rectum, it is always possible to exchange source and detector positions to get an illumination from the opposite side. For measurements in reflection mode (Fig. 4.3c), however, movement of the source will only cause a small change of the illumination angle for deep objects. We conclude that in reflection mode measurements the ambiguity between scattering and absorption should be avoided by using frequencies comparable or higher than $c\mu_a$.

Chapter 5

Numerical Implementation of the Virtual Source Formalism

In the last chapter we have seen that the virtual source formalism is a valuable tool to analyze the basic properties of the solutions of the light diffusion equation in inhomogeneous media. In this chapter we discuss how the virtual source formalism can be implemented as a numerical method. We have discussed this issue only briefly in conjunction with the theoretical aspects in Refs. [56, 58, 59, 60], here we give a more detailed discussion. In the first two sections the discretization of the recursive equation and the appearance of a self interaction term are discussed. Section 5.3 describes the actual iteration and section 5.4 introduces a technique to improve the convergence for strong perturbations. Section 5.5 briefly covers the extension to semi infinite geometries. In Section 5.6 we show that the surface effects due to sharp boundaries of scattering objects can potentially increase the resolution of inverse algorithms, but that this benefit is limited by a high sensitivity to discretization errors. In Section 5.7 we describe the implementation of the algorithms in two software packages.

5.1   Discretization

We recall the recursion formula Eq. (4.15) from section 4.2

$$\phi_n(\mathbf{r}) = \phi_0(\mathbf{r}) + \int\limits_{V_{obj}} d\mathbf{r}' S^{Virt}[\phi_{n-1}(\mathbf{r}')]\hat{G}(|\mathbf{r} - \mathbf{r}'|) \tag{5.1}$$

and the definition of the virtual source density Eq. (4.8–4.10) from section 4.1

$$S^{Virt}[\phi] = \frac{1}{3\mu'_{s0}}\Delta k^2 \phi \; + \; \frac{\boldsymbol{\nabla}\mu'_s}{\mu'_{s0}} \cdot \mathbf{J}. \tag{5.2}$$

For numerical evaluation the integral is discretized. The volume of the objects is splitted into N_V voxels of volume V_j with center points $\mathbf{r}_j$. For the fluence at an arbitrary point $\mathbf{r}$ Eq. (5.1) becomes

$$\phi_n(\mathbf{r}) = \phi_0(\mathbf{r}) + \sum_j^{N_V} V_j S_j^{Virt}[\phi_{n-1}(\mathbf{r}_j)]\hat{G}(|\mathbf{r} - \mathbf{r}_j|). \tag{5.3}$$

During the iteration, however, the perturbed fluence ϕ_n is calculated only at the voxel positions. Thus for a voxel at $\mathbf{r}_i$ we get

$$\phi_{n,i} = \phi_{0,i} + \sum_j^{N_V} V_j S_j^{Virt}[\phi_{n-1,j}]\hat{G}_{ij}, \tag{5.4}$$

where $\phi_{n,i} = \phi_n(\mathbf{r}_i)$ and $\hat{G}_{ij} = \hat{G}(|\mathbf{r}_i - \mathbf{r}_j|)$. The special case for $i = j$ is discussed in detail in the next section.

Note that the term for the virtual source strength $S_j^{Virt}[\phi_{n-1,j}]$ in Eq. (5.4) is a symbolic notation and somewhat deceptive because it suggests that the virtual source strength depends only on the fluence at the voxel j. However, $S_j^{Virt}[\phi_{n-1,j}]$ has to be understood as an operator, acting on $\phi_{n-1,j}$, because for scattering perturbations S_j^{Virt} involves the gradient of the fluence via $\mathbf{J}_j = -D\boldsymbol{\nabla}\phi_j$ (see Eq. (5.2)). The standard method to calculate a gradient on a discrete grid is the centered difference quotient, which in three dimensions uses
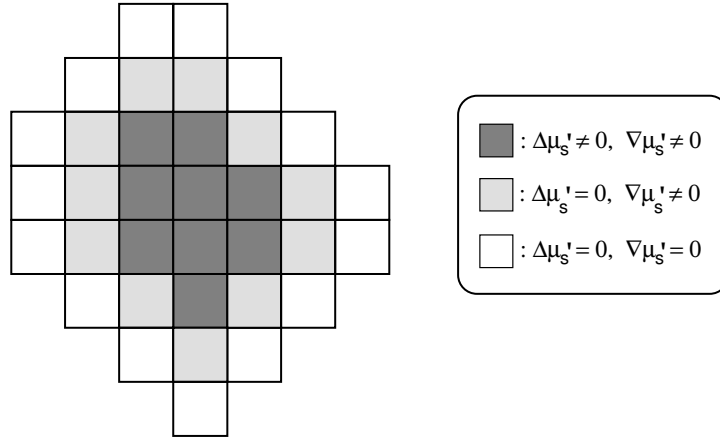
Figure 5.1: Discretization of scattering objects. The dark grey voxels belong to the object, i.e. have a $\Delta\mu'_s \neq 0$ and therefore carry a virtual source. The light gray voxels have the optical properties of the background ($\Delta\mu'_s = 0$), but the gradient of the scattering coefficient $\nabla\mu'_s \neq 0$ because the centered difference quotient uses values at neighboring voxels, which belong to the object. The white voxels are only used to compute the centered difference quotient of the fluence at the light gray voxels and carry no virtual source.

values at the six neighbor voxels. Therefore S_j^{Virt} depends on the fluence at voxel j and the six neighbor voxels.

A similar issue arises from the discrete computation of the gradient of the reduced scattering coefficient $\nabla\mu'_s$ in Eq. (5.2). Since the centered difference quotient uses the difference of the values at the neighboring voxels, a voxel just outside a scattering perturbation has a $\nabla\mu'_s \neq 0$ and therefore a virtual source. Since this virtual source also requires the computation of the gradient of the fluence with the centered difference quotient, the fluence at an extra voxel outside the object must be computed additionally. Thus scattering perturbations require *two* extra layers of voxels around the object. This situation is depicted in Fig. 5.1.

5.2   Self Interaction Term

The discretization of Eq. (5.1), which yields Eq. (5.4), appears to be a trivial step on first glance. However, consider the definition of $\hat{G}_{ij}$ in Eq. (5.4). For $i = j$ the Green's function $\hat{G}(|\mathbf{r}_i - \mathbf{r}_j|) = \exp(ik_0 |\mathbf{r}_i - \mathbf{r}_j|)/(4\pi D_0 |\mathbf{r}_i - \mathbf{r}_j|)$ has a singularity, which raises the question how $\hat{G}_{ii}$ should be defined. Physically, the question is if the perturbation at a voxel should affect the light field in the voxel. In other words, should there be a self interaction term $\hat{G}_{ii}$, and if yes, how can the singularity of the Green's function be avoided?

Note that formally our approach has a close analogy to the multiple scattering of waves on *solid* particles (see e.g. Ishimaru [3] section 14-1), where the self interaction is excluded and thus $\hat{G}_{ii} = 0$. But in our case the diffuse photon density wave is not scattered at a solid particle without penetrating it, instead it traverses the voxel and thus gives rise to a virtual source density inside the volume of the voxel. Therefore in our case the self interaction term $\hat{G}_{ii}$ does *not* vanish.

To see this formally, we take special care to derive the discretization of the recursion formula Eq. (5.1). The volume of the objects is splitted into N_V voxels of volume V_i with center points $\mathbf{r_i}$ and Eq. (5.1) becomes

$$\phi_n(\mathbf{r}_i) = \phi_0(\mathbf{r}_i) + \sum_{j}^{N_V} \int_{V_j} d\mathbf{r}' S^{Virt}[\phi_{n-1}(\mathbf{r}')]\hat{G}(|\mathbf{r}_i - \mathbf{r}'|). \qquad (5.5)$$

Up to now this is exact, we just splitted the integral and chose to evaluate the fluence only at the $\mathbf{r_i}$'s. We now assume that the virtual source density S^{Virt} becomes approximately constant in each voxel V_j if we make the voxels small enough[1], so that it can be pulled out of the integral. However , for $i = j$ the

---

[1] For objects with sharp steps in the optical properties the virtual source density will have discontinuities, but we assume that the volume elements can be chosen so that the branch is along the boundaries of the volume elements.
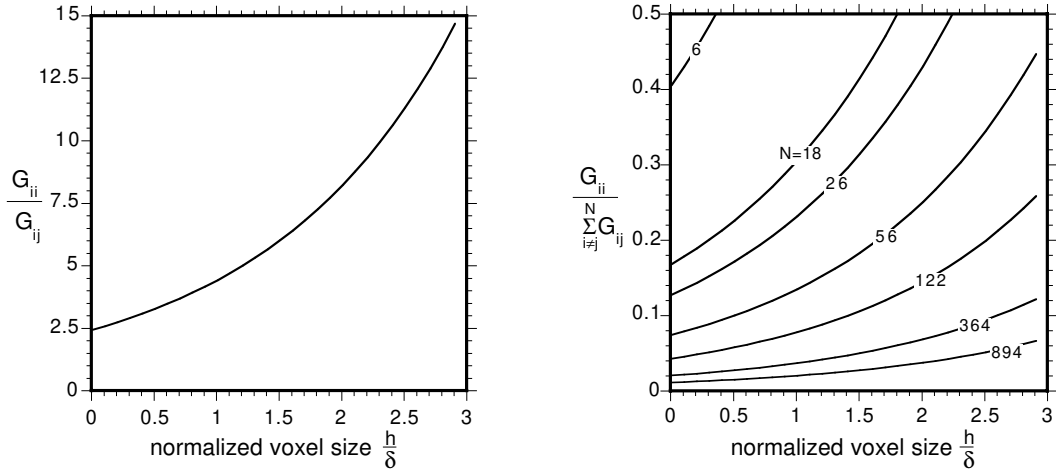
Figure 5.2: Contribution of the self interaction term $\hat{G}_{ii}$ relative to the contribution from neighboring voxels $\hat{G}_{ij}$ for steady state light. Left: for the nearest neighbor voxel. Right: for the sum of the N nearest neighbor voxels. The voxel size is normalized to the DC penetration depth δ.

Green's function has a singularity and can therefore *not* be pulled out of the integral. Thus we get

$$\phi_{n,i} = \phi_{0,i} + \sum_{j}^{N_V} V_j S_j^{Virt}[\phi_{n-1,j}]\hat{G}_{ij}, \tag{5.6}$$

where we explicitly calculate the self interaction coefficient $\hat{G}_{ii}$ as the integral over the volume of the i-th voxel:

$$\hat{G}_{ii} = \frac{1}{V_i} \int\limits_{V_i} d\mathbf{r}' \hat{G}(|\mathbf{r}_i - \mathbf{r}'|). \tag{5.7}$$

To integrate this equation analytically we make a simplification: instead of integrating over a voxel we integrate over a sphere with radius R that matches the volume of the voxel. This yields

$$\hat{G}_{ii} = \frac{1 - (1 - ikR)\exp(ikR)}{V_i(\mu_{a0} - i\omega/c)}. \tag{5.8}$$

How important is this self-contribution? To investigate this we compare the self-contribution with the contribution from the nearest neighbor voxels. In
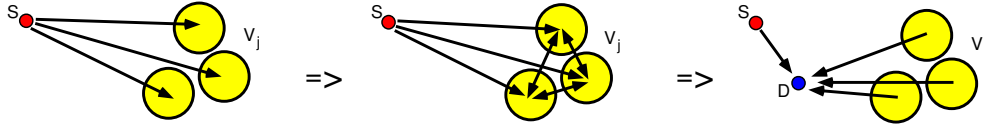
Figure 5.3: Iterative solution of the discretized version of the virtual source formalism. Left: illumination of the volume elements V_j of the perturbation by the real source S. Center: iteration of the recursive equation (5.4) allows for interaction of the volume elements. Right: after the iteration the real and virtual sources contribute to the fluence at arbitrary detector positions D according to Eq. (5.3).

Fig. 5.2a the ratio G_{ii}/G_{ij} is plotted, which compares the self-contribution only with the nearest neighbor at a distance h (h/δ is the dimensionless voxel length, normalized to the DC penetration depth δ). Fig. 5.2b shows the ratio to the sum of the contributions from the N nearest neighbor voxels. Note that this comparison does not allow to directly estimate the error which would result from neglecting the self contribution in an actual simulation, because the virtual source strength will generally be different for the different voxels of a large object, due to the quick decrease of the incoming fluence over distance from the source. However, two trends are clear: (i) the fewer voxels belong to an object, the more important is the self contribution; (ii) the larger the voxels, the more important is the self contribution.

5.3 Iteration

After the discretization of the integral equation has been thoroughly discussed we turn now to the actual iteration. It is helpful to visualize the procedure of the iteration, see Fig. 5.3. First, the background fluence due to the illumination by the real source(s) is calculated (left picture). This determines the virtual source strength S_j^{Virt} at the voxels. For the next higher order the fluence at

each voxel is calculated as the sum of contributions from the real sources and the virtual sources at all voxels according to Eq. (5.4), and then the virtual source strength is recalculated with the improved fluence (center picture). This iteration is repeated until the relative change of the fluence at all voxels is smaller than a given threshold. In this way the precision of the modeling can be adjusted to the requirements of the application. After the virtual source strength is thus obtained, the fluence can be computed at arbitrary positions, e.g. at a detector, according to Eq. (5.3) by summing up the contributions from the real and the virtual sources (right picture).

If the iteration, and equivalently the Neumann series (section 4.2), converges it is assured that it converges to the right and unique solution. The reason for this convenient quality is the fact that, contrary to the differential formulation, the integral equation already includes the boundary conditions and thus leaves no room for ambiguities. However, if the perturbation is too strong, that is if the objects are too large and/or the optical properties are too different from the background values, the iteration diverges. The Cauchy ratio criteria for convergence of the Neumann series is not a convenient test because it is overly restrictive [37]. In practice it will be preferable to start an iteration and see if it converges.

Figure 5.4 shows an example for a relatively strong absorbing perturbation, where several iteration steps are needed to reach a satisfying precision. To illustrate the effect of the iteration the fluence on a line through the source and the center of the object is shown for the first five iterations. The next iterations are omitted for clarity. The fluence approaches the solution, and after eleven iterations the fluence cannot be visibly distinguished from the final result (solid curve) in the plot. We emphasize that the fluence outside the object has been computed only for illustration purposes. During the iteration it is only necessary to compute the fluence *inside* the object.
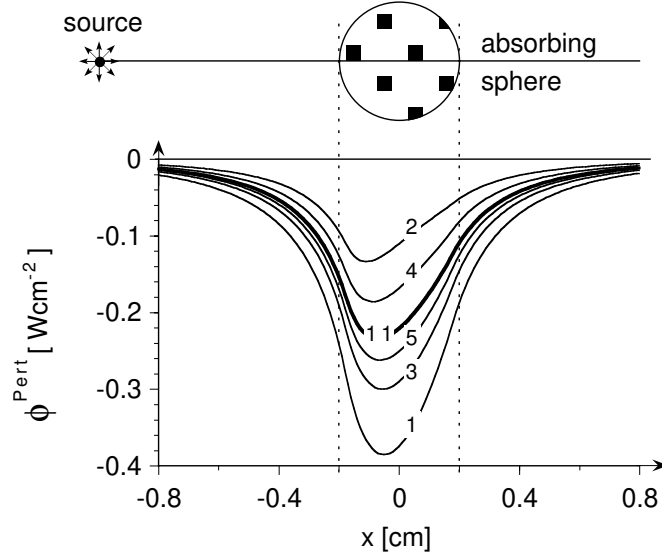
Figure 5.4: Normal iterative solution for a strongly absorbing object. The order of the iteration is indicated at the curves, the final solution is plotted with a thick line. The setup is similar to Fig. 4.1, but the absorption of the sphere is tenfold stronger. (Sphere: radius = 0.2 cm, 251 voxels, μ_a = 2.0 cm^{-1}, μ'_s = 10 cm^{-1}; background medium: μ_a = 0.1 cm^{-1}, μ'_s = 10 cm^{-1}; point source at x = -1 cm; S = 1 W.)

Note that the iterative solutions oscillate around the final solution. This can be understood by considering the Neumann series Eq. (4.16). In our example the absorbing perturbation has different but constant absorption, i.e. $\Delta\mu_a(\mathbf{r}) \equiv \Delta\mu_a$, $\Delta\mu'_s \equiv 0$. The virtual source strength is then simply $S^{Virt} = -\Delta\mu_a\phi$, and the Neumann series simplifies to

$$\phi_n = \phi_0 - \Delta\mu_a \int dV \hat{G} \, \phi_0 + \Delta\mu_a^2 \int dV \hat{G} \int dV \hat{G} \, \phi_0$$

$$+ \cdots + (-\Delta\mu_a)^n \left[\int dV \hat{G}\right]^n \phi_0. \tag{5.9}$$

For an object with increased absorption $\Delta\mu_a$ is positive, which results in an alternating series. The alternating sign explains the oscillation.

5.4 Optimized Iteration for Strong Absorbers

We have mentioned before that it is not mandatory to start the iteration with the background solution ϕ_0 in the perturbation integral. If we can guess a function that is closer to the actual solution ϕ we can certainly improve the iteration. For absorbing perturbations with higher absorption, where the iteration oscillates around the solution, it is straightforward to construct such an improved function: as we know that the real solution must lie between consecutive approximations it is appropriate to use the mean of the two previous order approximations to calculate the new virtual source strength. This can be done for each order in the iteration except for the first, so that the improved recursion formula for $\Delta\mu_a > 0$, $\Delta\mu'_s = 0$ becomes:

$$
\phi_{1,i} = \phi_{0,i} - \Delta\mu_a \sum_j^{N_V} V_j \hat{G}_{ij} \phi_{0,j},
$$

$$
\phi_{n,i} = \phi_{0,i} - \Delta\mu_a \sum_j^{N_V} V_j \hat{G}_{ij} \frac{\phi_{n-1,j} + \phi_{n-2,j}}{2} \qquad \text{for } n > 1. \quad (5.10)
$$

Figure 5.5 shows that this scheme indeed improves the convergence of the iteration significantly: the solution is already reached after the third iteration.

The optimized iteration does not only improve the speed of convergence, but even leads to convergence for strong perturbations which would be intractable, i.e. divergent, with the normal iteration procedure. To show the practical relevance we use an example which is inspired by an application from the optical diagnosis of brain hematoma in neonates. Compared to the adult head the head of a neonate is well suited for optical diagnostics. The main advantage is that transmission measurements across the neonatal head are possible, mainly because of the small diameter ($\approx$ 8–10 cm), the thin and transparent skull, and the relatively low scattering coefficient of the brain [48]. In Fig. 5.6 the setup for a frequency domain measurement on the neonatal
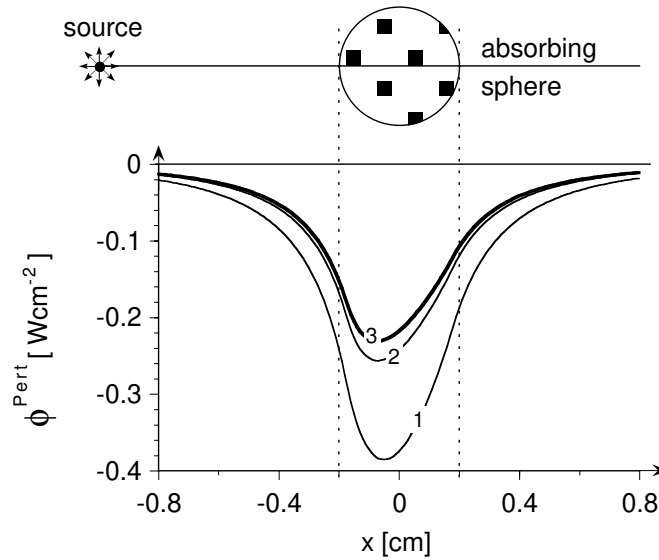
Figure 5.5: Optimized iterative solution for the same strongly absorbing object as in Fig. 5.4.

head is shown. It is very simplified: the background medium is infinite and the perturbation is spherical in order to be able to verify the results of the iterative solution of the integral formalism with the multipole method from chapter 3. The main purpose for this example is to show that the optimized iteration scheme enables the integral formalism to model realistically strong and large perturbations, such as hemorrhages.

Figure 5.7 shows that the first order Born approximation yields totally unacceptable results. The part of the amplitude ratio around the forward direction ($\alpha = 0°$) is folded up, which indicates that the perturbation ϕ_1 is stronger than the incoming background fluence ϕ_0, which is of course unphysically. With such a bad start the normal iteration scheme does not converge. However, the optimized iteration according to Eq. (5.10) *does* converge, and after eight iterations the result cannot be distinguished from the multipole method, which we use as a gold standard. Figure 5.8 shows in more detail how the phase difference changes during the iterations. The images show the phase dif-
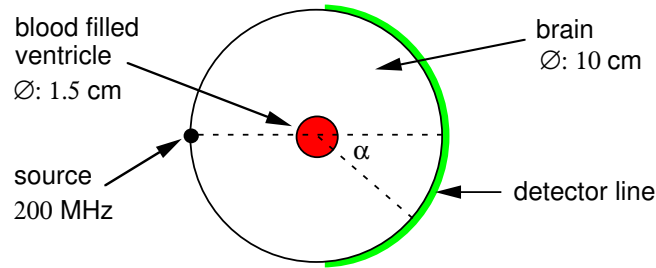
Figure 5.6: Schematic of a transmission measurement on a neonatal head. The optical properties of the brain are assumed as $\mu_{a0} = 0.2\ cm^{-1}$ and $\mu'_{s0} = 10\ cm^{-1}$. For simplicity the boundary conditions are neglected and an infinite background medium is assumed. The spherical perturbation in the center is a model for a hemorrhage in a ventricle, the optical properties $\mu_a = 1\ cm^{-1}$ and $\mu'_s = 10\ cm^{-1}$ mimic a mixture of cerebrospinal fluid and blood. The source is amplitude modulated at $f = 200$ MHz.
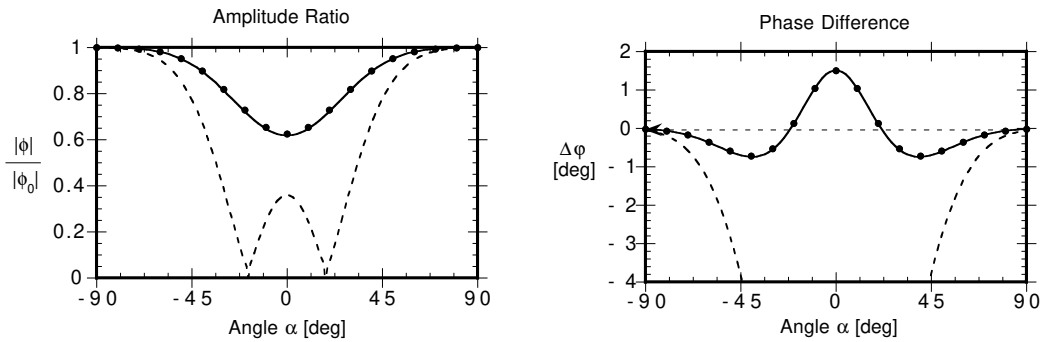
Figure 5.7: Simulated measurements on the circumfence of the neonatal head as indicated in Fig. 5.6. The solid curves are the 8th order iteration, the dashed curves are the first order Born approximation. For comparison, the symbols represent calculations made with the multipole method from chapter 3.

ference in a plane cut through source and object. The phase oscillates wildly for the first iterations, note the different range of the gray scale bar. Only for the iterations of order 7, 8, and 9 the range is the same, and one can see that the iteration now converges to a stable pattern.
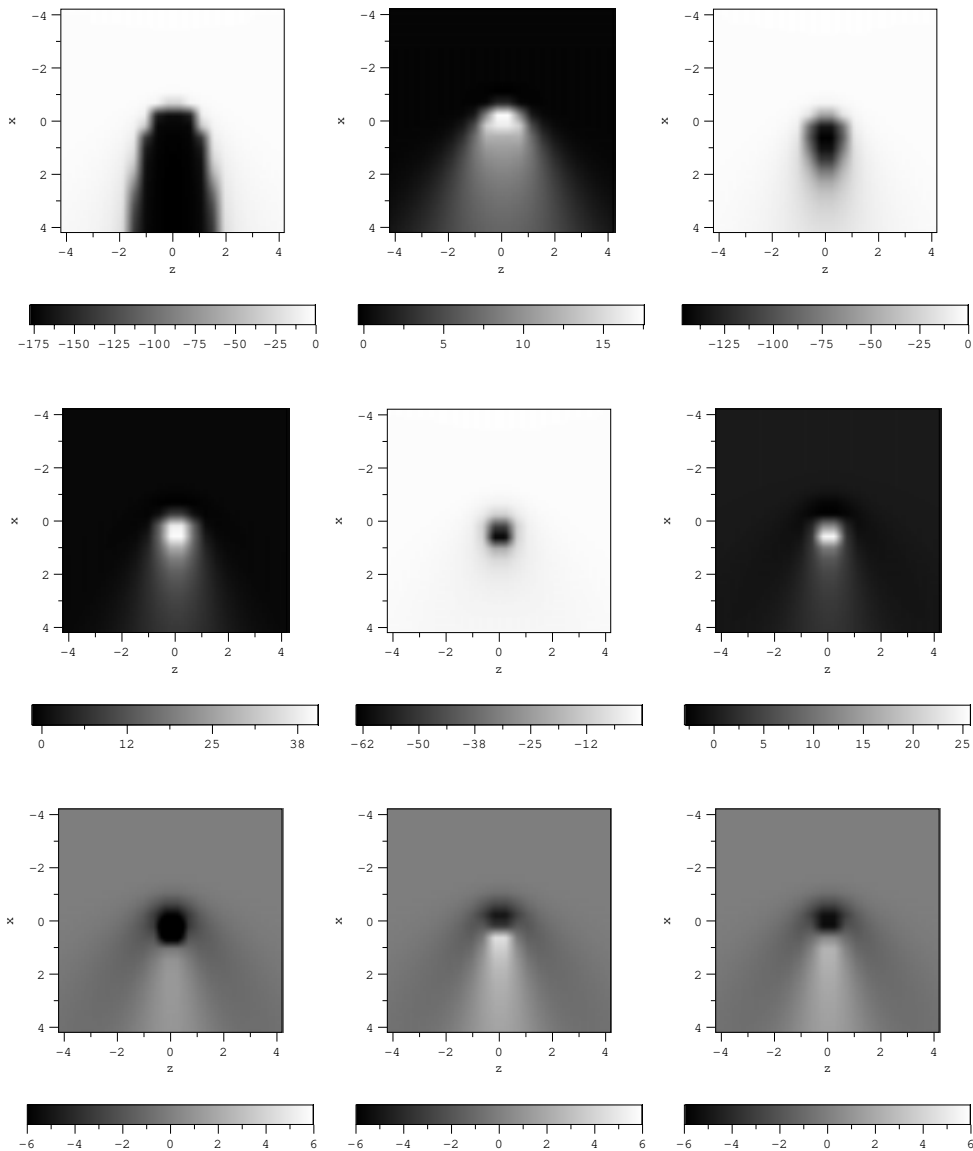
Figure 5.8: Evolution of the phase difference for the simulated measurement on the neonatal head for the first nine iterations with the optimized iteration scheme. The first order is at top left, then the order increases from left to right, and from top to bottom. Note that the geometry differs from Fig. 5.6, here the source is located at the top center of each image. Observe that the scale is only the same for the last three iterations.
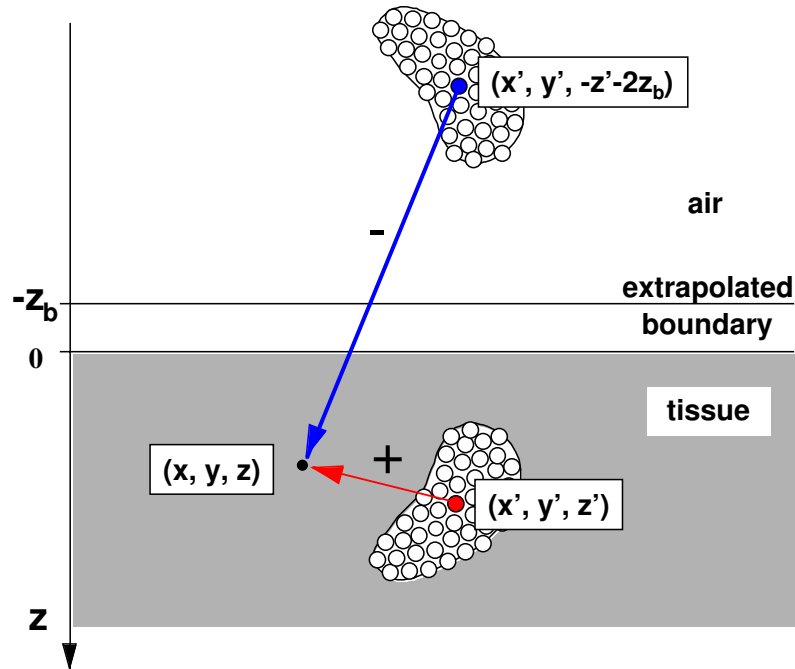
Figure 5.9: Perturbations in semi–infinite media. The method of image sources is applied to virtual sources as well as real sources.

5.5 Boundaries to Non–Scattering Media

The extension of the virtual source formalism to bounded systems is principally trivial. The only change with respect to the infinite background medium is to use the appropriate Green's function for the bounded medium. For semi–infinite media the Green's function for the extrapolated boundary condition Eq. (2.34) from section 2.3.2 simply adds an image source for every source in the medium, be it a real source or a virtual source. Thus the objects are effectively mirrored at the extrapolated boundary, see Fig. 5.9. For slab geometries the objects are consecutively mirrored at both boundaries, yielding a series of image sources [27]. For cylindrical and spherical geometries Arridge *et al* [31] have given analytical forms for Green's functions, albeit they are cumbersome series expansions involving Bessel functions. Note that the computation

of the Green's functions enters the total computational cost of the iterative solution only linearly. The reason is that the strength of the image sources is coupled to their original sources, thus they do not take part in the iteration independently.

5.6 Surface Effects and Discretization Errors

The sharp concentration of virtual sources at the surface of a scattering perturbation has the potential to increase the resolution of the inverse problem, because it makes a direct detection of the surface possible. Experimental reconstructions show indeed a higher resolution for scattering than for absorbing inhomogeneities [55].

However, the discretization for numerical evaluation results in errors that are most significant for the case of sharply bounded scattering inhomogeneities. One aspect is the limited resolution of the object which leads to a volume mismatch and also to a surface mismatch between the actual object and its voxel representation. Because this effect is highly influenced by the actual shape and position of the objects, we avoid it here by considering the cubic object **i** from the last paragraph, which can be represented by voxels exactly, i.e. without volume or surface mismatch. This allows us to concentrate on the importance of the proper numerical treatment of the surface integral. For the forward algorithm a separate evaluation of the surface integral is cumbersome but not difficult. However, for inverse algorithms it is certainly appealing to invert the basic equation for smooth optical properties, even if one knows a priori that sharp boundaries occur. This causes an error, but for a fine enough discretization, the error should become small. The question is then: what is a fine enough discretization?
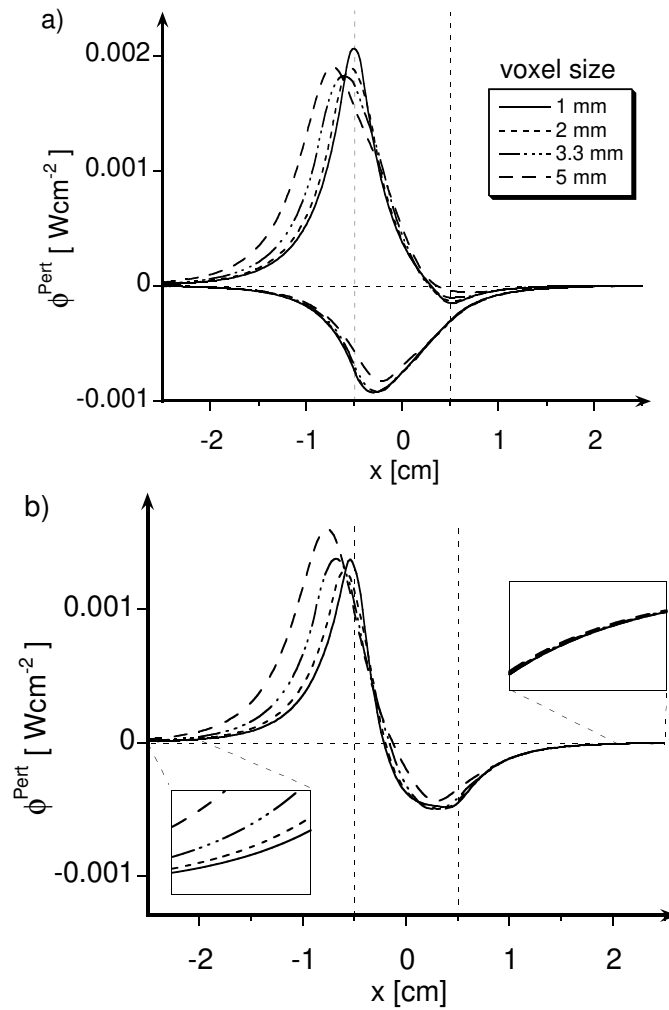
Figure 5.10: a) Volume and surface contribution for the scattering object **i** *from Fig. 4.4, calculated with different discretizations. b) The total perturbation is the sum of the volume and surface contribution in a).*

Fig. 5.10 shows numerical results obtained with the algorithm for smooth optical properties (Sec. 4.2). We compare four discretizations with a voxel size of 1, 2, 3.3, and 5 millimeters, which result in a representation of the 1 cm object by 1000, 125, 27, and 8 voxels respectively. As expected, the surface contribution is considerably more sensitive to discretization errors than the volume contribution and dominates the error of the total perturbation effect. Interestingly, the error is far more prominent in reflection than in transmission. This

can be explained by the different relative importance of both contributions: in reflection the surface effect dominates, in transmission the volume effect dominates (Fig. 5.10b. We infer that inversions based only on transmission measurements can use a coarser discretization than those utilizing reflection measurements, but therefore pay the price of a depleted surface resolution.

5.7   Software for Light Transport in Complex Inhomogeneous Systems

The numerical algorithm we have discussed in the previous sections has been implemented in two software packages, the 'SVS' and 'PMI' programmes. While the SVS software has been developed by the author, the PMI package is a joint project with researchers from the University of Pennsylvania. Both programmes will be discussed in sequence. Examples for complex geometries are given. Then a comparison with other numerical methods is drawn.

5.7.1   The SVS Software Package

SVS stands for 'superposition of virtual sources' and is the original implementation of the virtual source formalism. So far we have deliberately shown numerical results of the SVS software only for examples with simple objects as perturbations. We used either spheres in order to compare the results with the analytical multipole solution from chapter 3, or cuboids in order to avoid a volume mismatch due to the discretization of the object in a cartesian voxel grid. However, one of the chief merits of the virtual source formalism is that it can easily be applied to complex geometries with many objects of arbitrary

shape. In order to facilitate the use for such complex systems it was necessary to provide the SVS software with a flexible user interface. We therefore implemented an interpreter which executes the commands of a primitive programming language. The commands can be given either in an input file or interactively.

In a simulation three phases can be distinguished: the definition of the problem, then the actual solution of the integral equation, and finally the calculation of the detector signals. We now describe the commands for each phase and also give some brief hints with regard to the implementation. Command names and key words are printed in a `typewriter` font, parameters which have to be replaced by actual values or key words are printed *italic*.

5.7.1.1 The Definition Phase

In the definition phase all information about the situation to be modeled, which influences the light distribution, is specified. This includes the definition of the geometry with the included objects, the optical properties of all regions, and the definition of the light sources. It does not include the specification of the detectors, since they are assumed to have negligible effect on the light field.

The geometry of the scattering medium is set with:

> `Geometry` *type*

where *type* can be `semi_infinite` or `infinite`. An arbitrary number of isotropic light sources can be defined. Each has its own *name* and can have a different *phase* shift and *strength* (in W). All positions are given in cm:

> `Source` *name strength phase x y z*

However, all sources must have the same modulation frequency because the Green's function is determined by the frequency. It is set for the whole simulation with

`Frequency` *value*

where the *value* is given in Hz.

The optical properties for the different media are specified with the command

`Medium` *name mua mus g n*

where *mua* is the absorption coefficient μ_a in cm^{-1}, *mus* is the scattering coefficient μ_s in cm^{-1}, *g* is the scattering anisotropy[2], and *n* is the refractive index of the medium. The *name* of each media can be chosen freely (as long as it contains no blanks), with one exception: there must always be a definition of the background medium, which must have the *name* `background`.

The distribution of the different media, i.e. the definition of the perturbations in the background medium, is accomplished by composing the perturbation of simple geometrical objects, we have restricted ourselves to spheres, cylinders, and rectangular boxes. Spheres are defined with the command

`Sphere` *name x y z r*

where (*x, y, z*) specify the position of the center of the sphere and *r* is the radius. Cylinders are defined with

`Cylinder` *name x1 y1 z1 x2 y2 z2 r*

where (*x1, y1, z1*) and (*x2, y2, z2*) are the end points of the cylinder axes. The axes can have arbitrary orientation. Rectangular objects are defined with

`Box` *name x1 y1 z1 x2 y2 z2*

where (*x1, y1, z1*) and (*x2, y2, z2*) specify opposite corner of the box, whose sides are parallel to the coordinate axes. The objects can overlap, the rule is that a new definition overrides an older one. In this way complex geometries can be modeled, we will show an example in section 5.7.1.4.

Internally, the source, media, and object definitions are stored in linked lists of data structures. Each time one of these commands is called, a new structure

---

[2]Recall from chapter 2 that *g* is defined as the mean cosine of the scattering angle, and that the reduced scattering coefficient μ_s' is defined as $\mu_s' = (1 - g)\mu_s$.

is allocated and appended to the appropriate list. In this way the number of definitions is limited only by the available memory and thus very complex geometries can be defined.

5.7.1.2 The Discretization and Iteration Phase

For the iterative solution of the integral equation the objects have to be discretized, i.e. divided into voxels. If several objects are disjunct it is principally possible to use different voxel sizes for the objects. However, in the current version of SVS we use, for simplicity, a uniform grid to divide the objects into cubic voxels. It is defined with the command

> `Grid` *size*

where *size* is the length of a voxel side in cm.

Now the iterative solution can be started with the command:

> `Run` *type max_iterations accuracy*

The *type* of the iteration can be either `normal` or `optimized`, where the latter selects the optimized iteration scheme according to section 5.4. The last two parameters control when the iteration should stop. The fluence at the voxels of the objects is iterated until either the order of the iteration exceeds the value given with *max_iterations*, or until the maximal relative change of the fluence between two consecutive iterations is below the threshold defined with the parameter *accuracy*.

However, before `Run` starts the actual iteration, it first has to set up a discretized representation of the geometry and to create the appropriate data structures. The object definitions in the object–list are processed and the objects are thereby divided into voxels. The usual way to discretize a volume with a cartesian grid is to set up a three dimensional array of voxels, which covers the whole region of interest, in our case this means: covers all objects.

For typical perturbation–type geometries with several objects this is often inefficient because most of the voxels in the array will not belong to objects and are therefore not needed for the SVS algorithm. For this reason we use a different approach. For each voxel which belongs to an object a data structure for a virtual source is allocated and stored in a double linked list. It contains all information needed at this voxel, like a pointer to the appropriate media structure with the optical properties, the background and perturbation fluence and the virtual source strength. If a virtual source already exists at this voxel from a previously processed object definition, the information of the existing structure is replaced by the properties of the new object. In this way it is possible to model delicate structures with a fine discretization even if the objects cover a large volume.

However, the appearance of gradient terms in the virtual source strength for scattering perturbations (Eq. 4.10) complicates this approach, because the calculation of a gradient with a centered difference quotient requires the knowledge of the quantity at neighboring voxels. But in the virtual source list the neighbor voxel cannot be found by a simple index operation like in a cartesian array. Therefore the virtual sources in the list have to be interconnected by pointers. A second problem arises at the surface of objects, where voxels have no neighbors which belong to the virtual source list. In section 5.1 it is explained that two extra layers of voxels are required around a scattering perturbation in order to calculate $\nabla \mu'_s$ and $\nabla \phi$ numerically, see Fig. 5.1 on page 77. Therefore these extra voxels are added to the virtual source list as dummy virtual sources and are also connected with their neighbors in the list[3]. After the objects are thus discretized the actual iteration is performed according to the algorithm described in section 5.3.

It is useful to have a means of checking the definition of the geometry and the

---

[3]Note that these extra dummies generally have 'free neighbor places', which are *not* filled by adding new voxels to the list.

discretization. For this purpose the command

> `GeometryLog` *filename*

writes lists of graphic primitives representing the discretized objects, which can be directly read and displayed with the program MATHEMATICA. An example will be shown below in Fig. 5.11.

5.7.1.3   The Detection Phase

After the iteration has determined the virtual source strength at the voxels the fluence ϕ can be determined at any detector position by simply summing up the contribution of all real and virtual sources. The commands of the detection phase of a SVS run are used to define the position of the detectors and also to define what quantity is actually used as output and what format is used. The structure of most output commands is

command_name what2print filename xlo ylo zlo xhi yhi zhi nx ny nz

The output is not displayed directly, but always written to a file specified by the *filename* parameter. The *command_name* determines for what graphic program the output should be formatted. Currently available options are

- `Gnuplot2D` for line plots with Gnuplot, a popular public domain graphic program on UNIX workstations

- `Gnuplot3D` for surface plots with Gnuplot

- `Math3D` for surface plots with MATHEMATICA

- `OutputHDF` for writing line, plane, or volume data to HDF files[4].

---

[4]The Hierarchical Data Format, short HDF, is a file format devised at the National Center for Supercomputing Applications NCSA in Urbana Champaign. It can be displayed by a number of programs, e.g. 'Spyglass' from Fortner Reasearch Inc.

The parameters *xlo ylo zlo xhi yhi zhi* specify the coordinates of the line, plane, or volume to be covered with detectors, and *nx ny nz* set the number of detectors in each coordinate. An exception is the command `Gnuplot2D` with only one parameter *n* for the number of detectors along the line.

The parameter *what2print* controls what kind of output is generated and can have the following values:

- `F` : perturbed fluence ϕ

- `B` : background fluence ϕ_0

- `P` : perturbation fluence $\phi^{Pert} = \phi - \phi_0$

- `PJ` : component of ϕ^{Pert} due to integral over S_ϕ^{Virt}

- `PF` : component of ϕ^{Pert} due to integral over $S_{\mathbf{J}}^{Virt}$

Since these quantities have complex values they cannot be displayed by the graphic programs directly. Therefore a prefix selects a real quantity:

- `RE_` : real part

- `IM_` : imaginary part

- `AM_` : amplitude

- `PH_` : phase

Some examples for valid combinations are:

- `RE_B` : real part of the background fluence

- `PH_P` : phase of the perturbation fluence

- `AM_PJ` : amplitude of the part of ϕ^{Pert} that is due to $S_{\mathbf{J}}^{Virt}$.

There are also special keywords for three frequently used quantities:

- `PH_DIF` : phase difference between total and background fluence

- `AM_RAT` : amplitude ratio between total and background fluence

- `AM_DIF` : amplitude difference

5.7.1.4 Examples for Complex Inhomogeneous Systems

Before we consider a complex system it is useful to illustrate the typical use of the commands for a simple case. We choose the scattering sphere from Fig. 4.2 on page 66. The SVS input script for this example is:

```
Geometry  infinite
Frequency  0

#       name        mua  mus   g      n
Medium background   0.1  100  0.9  1.37
Medium tumor        0.1  200  0.9  1.37

#       name  medium  x  y  z    r
Sphere  o1    tumor   0  0  0  0.2

#       name  magn  phase    x  y  z
Source  s1    1       0     -1  0  0

Grid  0.05

#      mode    max_iteration  accuracy
Run   normal       10           0.001

#           type    file      x1 y1 z1  x2 y2 z2   n
Gnuplot2D  RE_P    scat.rp   -1  0  0   1  0  0   100
Gnuplot2D  RE_PF   scat.rpf  -1  0  0   1  0  0   100
Gnuplot2D  RE_PJ   scat.rpj  -1  0  0   1  0  0   100
```

Note that everything after a '#' character is a comment. When this script was run, the sphere was discretized into 251 voxels, the volume mismatch between the sphere of 2 mm radius and the sum of the voxels was 6 %. Four iterations were performed to reach the desired accuracy, this took 1.7 CPU seconds on an Apple PowerBook 5300cs with 100 MHz clock rate.

Now we come to an example with complex inhomogeneities. Figure 5.11 shows the voxel representation of a situation with ramifying blood vessels and a tumor, where one small vessel goes right through the tumor. This structure was composed with `Sphere` and `Cylinder` commands in the SVS script in Tab. 5.1. Figure 5.11 also shows the position of the illuminating amplitude modulated source ($f = 100$ MHz) at $\mathbf{r}_s = (0,0,0)$, and the location of three detector planes, which were defined with the `Math3D` commands.

The graphic primitives for Fig. 5.11 were automatically created with the `GeometryLog` command in the SVS script and then displayed with MATH-EMATICA. Only the lines for the detector planes and the annotation for the source was added manually. The `GeometryLog` command is very useful to verify the correct placement of the objects. It also allows to judge if the discretization is fine enough to give a reasonable representation of the objects.

Figure 5.12 shows the results of the simulation at the three detector planes. In the top graph on can see that the tumor with its increased scattering reflects the light back and thus causes a maximum in the detector plane above the tumor. In the bottom graph the detection plane is located beneath the tumor, which therefore throws a shadow and thus depletes the light field. In the graph in the center the detection plane cuts through the middle of the tumor. The detection plane is thus halfway between the positive virtual sources at the top surface and the negative virtual sources at the bottom surface. Therefore the tumor has little effect on the light field. However, one can clearly see how the small absorbing blood vessel, which leads through the tumor, causes a small
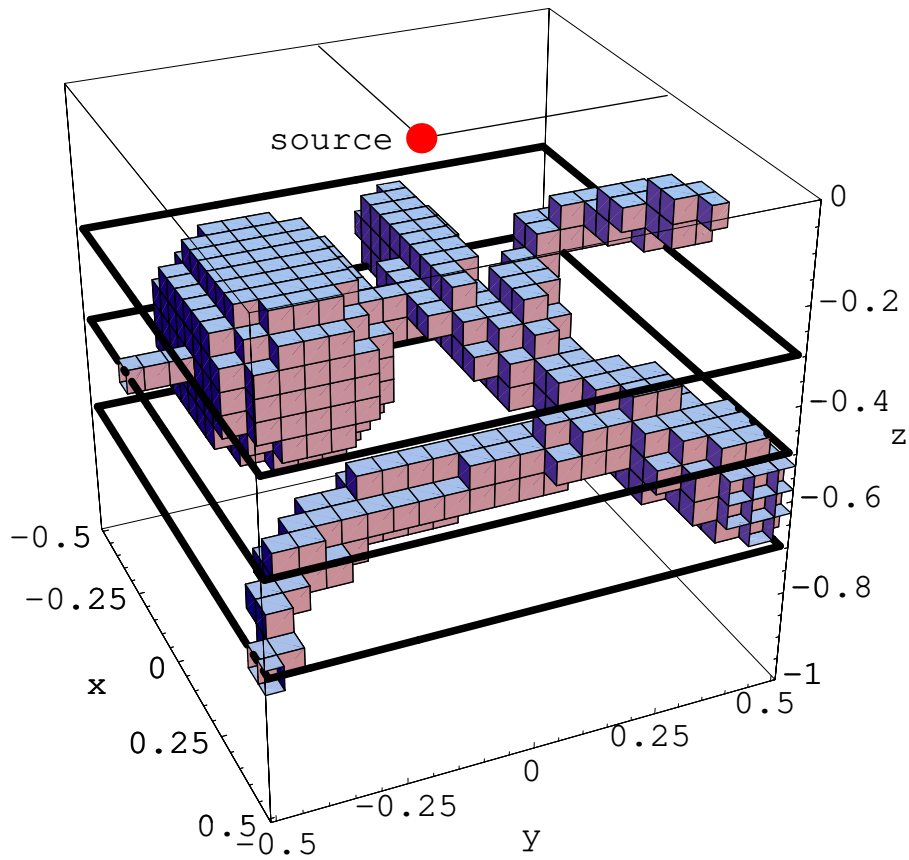
Figure 5.11:   Example for the modeling of a complex inhomogeneous system with the SVS program. Shown is the voxel representation of some blood vessels and a tumor, note that one small vessel goes through the tumor. This scene is illuminated by one amplitude modulated (f = 100 MHz) point source at $\mathbf{r}_s$ = (0,0,0). This graphical representation of the geometry and the discretized objects was created by the SVS script in Fig. 5.1. The three thick rectangles indicate the position of detector planes. The results at the detector planes are shown in Fig. 5.12.

but distinctive valley in the surface plot.

```
Geometry   infinite
Frequency  100e6

### define media ###
#         name        mua   mus    g      n
Medium  background   0.1   100   0.9   1.37
Medium  tumor        0.1   500   0.9   1.37
Medium  blood        3.0   100   0.9   1.37

### define objects ###
#         name   medium  xlo   ylo    zlo     xhi    yhi    zhi     r
Sphere    t1     tumor  -0.35 -0.2   -0.5                          0.19
Sphere    t2     tumor  -0.25 -0.2   -0.5                          0.19
Sphere    t3     tumor  -0.2  -0.2   -0.5                          0.19
Cylinder  v1     blood   0.5   0.5   -0.6    0.2   0.25  -0.5     0.09
Cylinder  v2     blood   0.2   0.25  -0.5   -0.1   0.1   -0.4     0.07
Cylinder  v3     blood  -0.1   0.1   -0.4   -0.5   0.15  -0.4     0.07
Cylinder  v4     blood   0.3   0.35  -0.5    0.2  -0.05  -0.6     0.06
Cylinder  v5     blood   0.2  -0.05  -0.6    0.2  -0.2   -0.6     0.06
Cylinder  v6     blood   0.2  -0.2   -0.6    0.3  -0.4   -0.65    0.05
Cylinder  v7     blood   0.3  -0.4   -0.65   0.5  -0.5   -0.7     0.04
Cylinder  v8     blood   0.1   0.2   -0.4   -0.1   0.25  -0.35    0.04
Cylinder  v9     blood  -0.1   0.25  -0.35  -0.15  0.35  -0.3     0.04
Cylinder  v10    blood  -0.15  0.35  -0.3   -0.05  0.4   -0.25    0.04
Cylinder  v11    blood  -0.05  0.4   -0.25   0.2   0.5   -0.15    0.04
Cylinder  v12    blood  -0.1   0.1   -0.4   -0.25 -0.2   -0.5     0.04
Cylinder  v13    blood  -0.25 -0.2   -0.5   -0.25 -0.5   -0.5     0.04

#      name  magn  phase   x  y  z
Source P     1       0     0  0  0

# define size of grid
Grid  0.05

#      mode      max_iter   accuracy
Run optimized      10         0.01

# write graphical check how the virtual sources are placed.
GeometryLog  voxels.m

#  3D output for Mathematica.
#      what2print  file    xlo  ylo  zlo   xhi  yhi  zhi   nx  ny  nz
Math3D  AM_RAT   ar1.m   -0.5 -0.5 -0.3   0.5  0.5 -0.3   25  25   1
Math3D  AM_RAT   ar2.m   -0.5 -0.5 -0.5   0.5  0.5 -0.5   25  25   1
Math3D  AM_RAT   ar3.m   -0.5 -0.5 -0.7   0.5  0.5 -0.7   25  25   1
```

Table 5.1: SVS input script for modeling the complex geometry shown in Fig. 5.11.
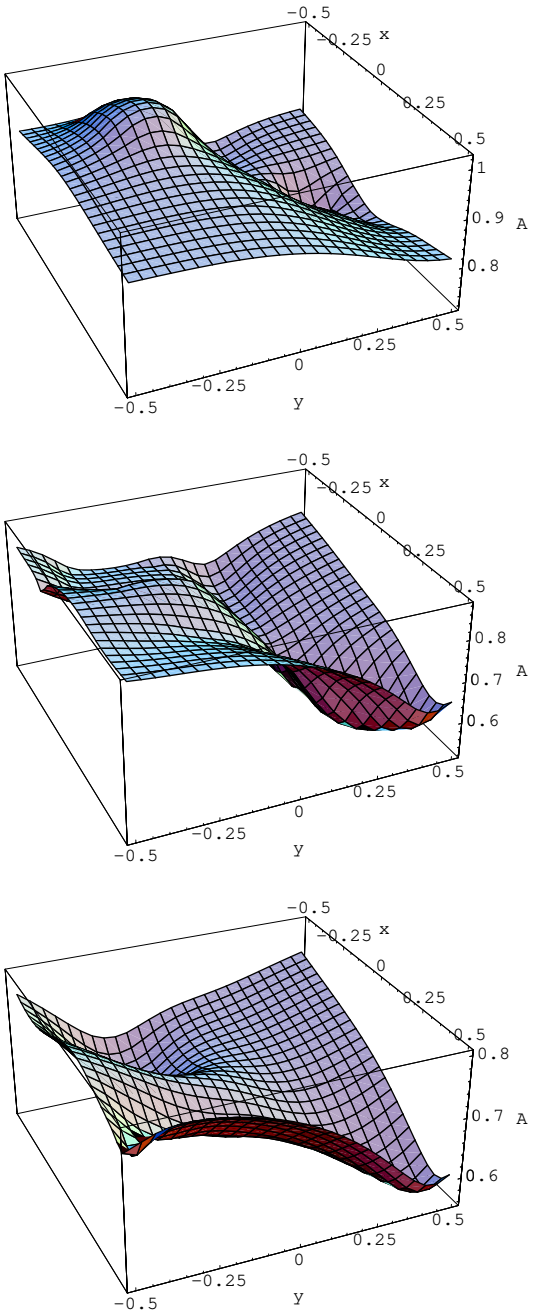
Figure 5.12: The amplitude ratio $A = \phi/\phi_0$ at the three detector planes from Fig. 5.11. From top to bottom the graphs are for the planes at $z = -0.3$ cm, -0.5 cm, and -0.7 cm.

5.7.2   The PMI Software Package

The PMI software started as a collaborative effort between the author, then at the University of Texas in Houston, and Maureen O'Leary [50] and David Boas [18] from the University of Pennsylvania in Philadelphia. 'PMI' stands for 'photon migration imaging'. The basic idea was to merge the different software modules from both groups in one program with a unified user interface and common data structures. The basic structure of the SVS program was used as the backbone of the PMI software because the flexibility of the concept allowed for an efficient addition of other software modules.

The modules are:

- **SVS Module:** Implementation of the SVS algorithm

- **Exact Module:** Implementation of multipole solutions for spheres and infinite cylinders

- **Fluorescence Module:** Analytic solutions for fluorescent diffuse photon density waves

- **Fit Module:** χ^2 algorithm to fit simulated or measured data to a model medium

- **Reconstruction Module:** Algorithms for reconstructing optical properties from measurements of the fluence

- **MIE Module:** Commands for calculation of the scattering coefficient of microsphere suspensions based on Mie theory.

A convenient feature of the fusion of the different modules in one software package is for example that the SVS method and the multipole expansion

solution for spheres (EXACT module) can now be compared in one program run.

A further discussion of the PMI software is beyond the scope of this work. To give an impression of the extensive features of the package a copy of the online help file is provided in appendix B. It describes the general usage and the commands of the different modules.

5.7.3 Comparison With Other Numerical Methods

The virtual source formalism is not the only numerical approach with the ability to model complex geometries. In the following we compare Monte Carlo simulations as well as finite difference and finite element solutions of the diffusion equation with our SVS method. We cannot give a thorough comparison, but will highlight some of the benefits and drawbacks of the different approaches with respect to their practical use for biomedical applications.

Monte Carlo simulations can be easily applied to heterogeneous media [14, 63]. The Monte Carlo simulation is regarded as the gold standard of the numerical methods because it is directly based on radiative transfer theory. Therefore it can model light propagation even in situations where diffusion theory fails. However, for most practically relevant cases Monte Carlo simulations are very time consuming. Especially for the computation of weak perturbations the Monte Carlo method is of little use. As an example, consider Fig. 5.13. It shows the amplitude ratio, i.e. ϕ/ϕ_0, for an absorbing sphere computed with the virtual source formalism SVS and with a Monte Carlo simulation. The setup is similar to the one used in Fig. 4.1 in section 4.4, however, in order to improve the statistics of the Monte Carlo simulation the absorption of the background medium and the sphere were drastically increased and the source
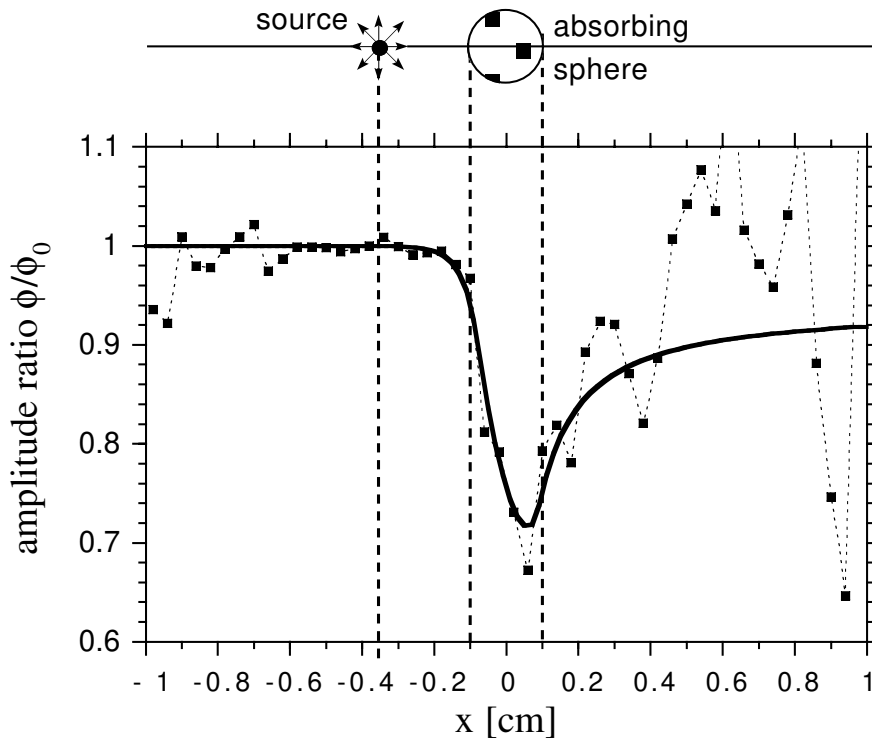
Figure 5.13: Comparison of the SVS method (solid line) with a Monte Carlo simulation (dashed line with symbols). The background optical properties are $\mu_{a0} = 1\ cm^{-1}$ and $\mu_{s0} = 12\ cm^{-1}$, the sphere has the same reduced scattering coefficient and an absorption coefficient $\mu_{a1} = 3\ cm^{-1}$.

was placed nearer to the object. Still, the statistical error of the Monte Carlo simulation is unacceptably high, although the simulation took three days on a SUN SparcStation 10. The iteration with the SVS program took only a few seconds. This example makes clear that even with the rapid progress in computer technology Monte Carlo simulations of typical perturbation situations will remain unpractical for some time.

To avoid the high computational cost of the Monte Carlo simulation one usually resorts to numerical solutions of the diffusion equation. Established numerical techniques to solve differential equations are the finite difference and finite element methods. Both have been used as forward algorithms to compute the

light distribution in complex scattering media.

A two dimensional implementation of the finite element approach has been used by Arridge and Schweiger [43, 64] to simulate light propagation in the human head. A high number of grid elements in a cross section of the two dimensional head model allowed for a fine modeling of the detailed structure of white and grey brain tissue. However, this high resolution is somewhat deceptive, since a two dimensional model is of little practical use, and an extension to three dimensions with the same resolution yields unacceptable computational cost.

In three dimensional geometries standard finite difference algorithms have the same principal problem of a high number of volume elements as finite element methods. To illustrate this issue Fig. 5.14 juxtaposes schematical representations of the three discussed approaches, i.e. Monte Carlo simulation, our solution of the integral formulation of the diffusion equation (SVS algorithm), and finite element and finite difference solutions of the differential diffusion equation. These graphics highlight the differences in the modeling of the objects and – equally important – the space *between* the objects for a typical perturbation geometry.

In Monte Carlo simulations the simulated photons spend most of their path in the background medium and are also concentrated near the source (Fig. 5.14 top left). Only seldom a photon passes through the objects and thus carries information about the perturbation. As a consequence, the simulation of the light propagation in the background medium is the reason for the high computational cost.

In finite element and finite difference methods the situation is similar, because the whole space between the objects has to be discretized (Fig. 5.14 bottom).
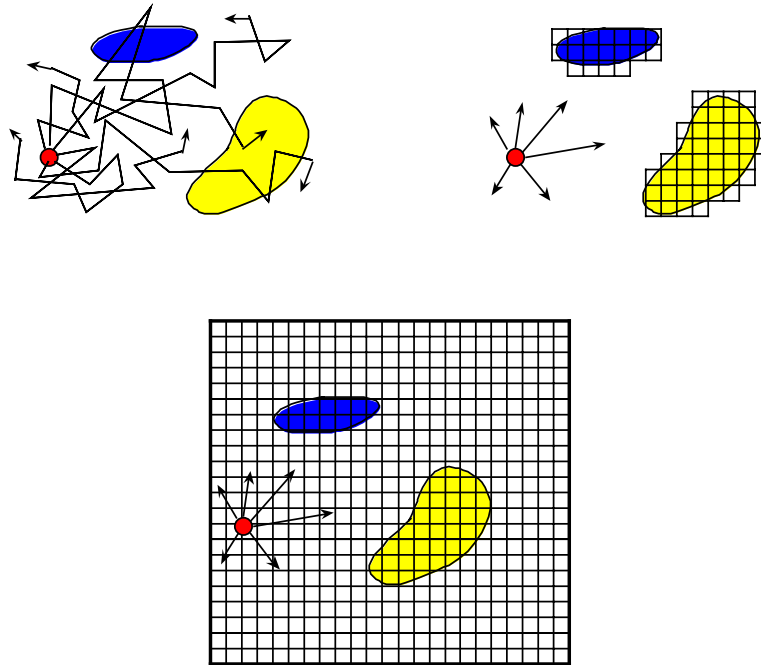
Figure 5.14: Schematics of the different modeling approaches of Monte Carlo simulation (top left), SVS (top right), and finite difference and finite element methods (bottom).

Furthermore, because these approaches are based on the differential formulation of the diffusion equation it is necessary to specify boundary conditions on the bounding surface of the modeled volume. Therefore the modeled volume must be extended either to the real surface of the tissue, where the partial current boundary condition can be applied, or the volume must be extended far enough into the depth of the tissue to approximately use the boundary condition of zero fluence. This means that the modeled volume will usually extend beyond the objects considerably, which further increases the number of volume elements and therefore the computational cost.

Contrary to these methods, the SVS approach (Fig. 5.14 top right) does not need to discretize the volume of the background medium at all, because the integral formulation of the diffusion equation needs to be solved only *inside* the perturbations. This results in a comparably small number of volume elements

even for a fine discretization of the objects and thus leads to short computation times. The accuracy of the solution can be directly controlled during the iteration and can thus be adapted to the needs of the application. A specific advantage of the SVS method for diagnostic applications is that it directly computes the perturbation signal, while the other approaches have to subtract the solution of the background medium from the solution of the perturbed situation, which can lead to numerical problems since both solutions are very similar if the perturbation is weak.

In summary, the SVS approach is favorable for applications which can be naturally described in terms of perturbation theory, i.e. as objects in an otherwise homogeneous background medium. This covers a large number of medically interesting applications, like tumors or localized bleedings. However, the SVS method does not converge in cases where the the perturbation is too severe. In these cases it will generally be appropriate to use finite difference or finite element methods. Monte Carlo simulations are computationally very expensive and should therefore only be used if the other methods cannot be applied because diffusion theory fails to describe the problem.

Chapter 6

Optical Detection of Brain Hematoma

In this chapter we discuss the design and application of an optical probe for the detection of brain hematomas in an early stage of the treatment of trauma patients.

The aim of this project is directed towards a clinical application, it is therefore important to consider the actual needs in the clinical practice very carefully. This inevitably requires a collaborative effort of physicists and physicians. In this case, a close cooperation with Dr. E. Ludwig, Dr. S. Zander, and Prof. Dr. W. Weinrich from the Department of Neurology at the Nordstadt Krankenhaus Hannover was established.

Motivated by the importance of the clinical aspects we begin this chapter with a rather comprehensive introduction with an emphasis on the medical issues.

6.1   Introduction

6.1.1   Overview over Traumatic Head Injury

6.1.1.1   Epidemiology

Traumatic brain injuries are the most common cause of disabilities among young adults. Mostly these injuries are the result of traffic accidents, and conversely about 60–70% of the lethal traffic accidents can be attributed to brain injuries. In Germany, 200000 cases of traumatic brain injuries occur every year, 50000 of them are severe brain injuries, and about 10000 have a lethal outcome [65, 66, 67]. Still the mortality rate is high, although the diagnostic and therapeutic means have improved significantly in the past.

6.1.1.2   Classification

Traumatic brain injuries can be divided into closed and open injuries. Open injuries involve a fracture of the skull and a penetration of the outermost brain membrane, the dura mater. However, they account only for about 3% of the cases [66], we therefore concentrate on the closed injuries. Depending on the nature of the applied forces, i.e. acceleration, deacceleration, rotation, or a combination thereof, the type of injury varies. Diffuse injuries involve a damage of neuronal structure of the brain tissue and obviously affect the brain function directly. They also cause edema, i.e. a swelling of the brain as a secondary effect. A second class of injuries are acute intracranial hematomas, that is bleedings inside the skull. They can be divided in intracerebral hematomas (bleeding inside the brain tissue), and extracerebral hematomas like epidural, subdural, and subarachnoidal hematomas, which are located between the skull and the brain. They will be described in more detail in section 6.2.

The most damaging and acute life–threatening effect of acute hematomas is the resulting increase of the intracranial pressure, that is the pressure inside the skull. The intracranial pressure (ICP) increases because the rigid compartment of the skull does not allow for an expansion of the brain, therefore the additional volume of the bleeding compresses the brain tissue. As a result the intracranial perfusion pressure, that is the difference of the arterial blood pressure and the intracranial pressure, decreases, which can lead to an insufficient oxygen supply to the brain tissue (hypoxia). This causes a swelling of the brain tissue which in turn increases the ICP even more [68]. If this cycle is not stopped, a compression and damage of the brain stem, which controls such vital functions as the breathing, will lead to death.

6.1.1.3 Initial Diagnosis and Treatment

The first task of emergency medicine at the accident site is to stabilize the vital functions of the patient. This involves the stabilization of the cardiac functions, shock treatment, and intubation of the patient, often the patient is also sedated. Then the neurological status of the patient is assessed. The neurological functions are usually rated with the *Glasgow Coma Scale* according to the response of the patient to a standardized set of stimuli, like verbal response, motoric response, and response and appearance of the eyes. Based on the results a first diagnosis for brain injuries is established. Patients with a significant brain injury have to be brought to a specialized clinic with a neurosurgery unit and a computer tomograph, while others can be brought to the nearest clinic with emergency and operating rooms.

For a favorable outcome after severe brain injuries the immediate begin of an appropriate therapy is of utmost importance. Therefore the initial diagnosis at the accident site plays a key role, because an admission to the wrong hospital, that is a hospital without CT or neurosurgery, can cause an unacceptable

delay of a life saving surgery. Unfortunately, the initial diagnosis is not always specific. Since it is based on the response of the patient the diagnosis can be hindered by the intubation and sedation of the patient. Also, an intracranial bleeding may still be too small to show significant neurological symptoms. Neurological symptoms indicate that a damage of the brain is occurring or has already occurred. Any prevention of a neurological symptom, and therefore of the associated damage, is expected to improve the outcome in terms of lethality and morbidity. It is therefore highly desirable to diagnose a hematoma *before* the onset of neurological symptoms. Clearly, the initial diagnosis at the accident site could significantly benefit from an easy to handle optical detection system.

If the initial diagnosis suggested a brain injury, a computer tomography (CT) scan will be performed immediately upon admission to the neurosurgery. Based on the results the further therapy is planned. Intracranial hematomas above a certain size are surgically removed. Acute hematomas can lead to a very quick deterioration of the situation, the patient can die within minutes. Therefore emergency surgery is sometimes performed immediately even without a CT scan. For less acute cases with small hemorrhages surgery might not be needed and the patients can be admitted to the intensive care unit. An increase of the intracranial pressure can then be counteracted with hyperventilation, slight elevation of the head, a drainage for the cerebrospinal fluid, and pharmaceutical means like osmotic therapy.

During intensive care the patients have to be monitored closely with respect to their neurological status. Delayed hematoma can occur some hours or days after an initial CT scan or after a surgical removal of a hematoma. This can lead to a sudden neurological deterioration with an immediate need for a CT scan and surgery. In other cases the delayed bleeding occurs slowly and is difficult to detect with a neurological examination. However, CT scans cannot be used as a means of monitoring due to both the high cost and the high

exposition of the patient to ionizing radiation. Here, we can again identify an opportunity for optical diagnostics, because the low cost and the absence of any radiation hazards allows for frequent examinations over extended periods of time. Indeed, Gopinath *et al* [69] have recently investigated this approach. We describe their work in the next section in the framework of other optical techniques for head diagnostics.

6.1.2   Optical Diagnosis of the Brain

The head, or more precisely the brain, has been a target for optical diagnosis for more than two decades. This work was pioneered by a study on the determination of the cerebral oxygen saturation with near infrared spectroscopy by Jöbsis [70] in 1977. The vast majority of the investigations is still targeted towards the noninvasive determination of metabolic information and especially towards the oxygen supply of the brain. The reason is that the brain has a high metabolic rate and is therefore especially vulnerable to even short periods of hypoxia. Thus the cerebral oxygen supply is a valuable information for a variety of applications, such as monitoring during birth [71] and neonatal intensive care [48]. Other applications are the mapping of brain activity [72, 73] and the diagnosis of Alzheimer's Disease [74]. Time resolved [48, 75, 76] as well as frequency domain [77, 78] and even DC techniques [79] have been employed. An abundance of literature on this topic is available, an extensive collection of references is, for example, given in [80]; reports on more recent developments can be found in [81].

In view of the extensive research on the spectroscopic measurement of the brain oxygenation status it is somewhat surprising that the optical detection of brain hematomas has been investigated only recently. Gopinath *et al* [82, 69, 83] have used near infrared light for the diagnosis of delayed brain hematoma starting in

1993. They employed a two wavelength device originally devised for portable muscle oxygenation measurements but used only one wavelength to perform simple absorption measurements. The anatomic variations from patient to patient, as well as for different locations on the head of the same patient, forced to use a symmetric measurement scheme. Measurements on the same relative position on the right and left side of the head were taken. Thus the resulting attenuation difference allowed to identify a hematoma on one side of the head by comparison with the healthy other side of the head. With repeated optical scans after the initial CT scan in the clinic it was possible to detect the development of delayed hematomas prior to the appearance of neurological symptoms.

6.1.3   A New Application: Optical Detection of Brain Hematomas for Emergency Medicine

The work by Gopinath *et al* has demonstrated that the optical detection of hematomas in a clinical setting *is* possible. On first thought it is therefore tempting to use the same equipment and procedure for the detection of acute brain hematomas in an emergency situation.

However, the application of an optical probe in emergency medicine puts high demands on the design of the probe. Time is extremely precious at the accident site. The decision about the destination of the emergency vehicle must be made as early as possible. Therefore the time slot for an optical examination is short, probably under five minutes. Thus the probe must be easy to handle, even under stress conditions. It must be portable. While in an emergency vehicle a design with a control unit and a separate sensor head might be acceptable, a single, small hand–held device is strongly preferable.

To meet these requirements it is desirable to use simple DC techniques, because a probe based on frequency domain or time domain techniques would be too bulky and also too expensive for this application. In the remainder of this chapter we therefore concentrate on DC measurements. In order to optimize the detection system for our specific application it is necessary to analyze the light propagation in the head. In the next section we will therefore discuss the anatomy of brain hematomas. Based on this information we then define simplified yet realistic model systems and use them to model the light propagation numerically in section 6.3. The results are then utilized in section 6.4 for the design of the probe. First results are presented in section 6.5.

6.2   Brain Hematoma

This section gives an introduction to the pathology of brain hematomas. We first discuss the normal anatomy and then turn to the different types of brain hematoma.

6.2.1   Normal Anatomy

Figure 6.1 shows a simplified schematic of the anatomy of the outer region of the head, including the skull, the brain membranes, and the upper layers of the brain. Special attention was paid to the brain membranes.

Directly below the skull is the outermost brain membrane, the *dura mater*. Dura mater and skull are connected only at the sutures between the different plates of the skull, elsewhere a thin space, the *spatium subdurale*, separates skull and dura mater. Below the dura mater is the second brain membrane,
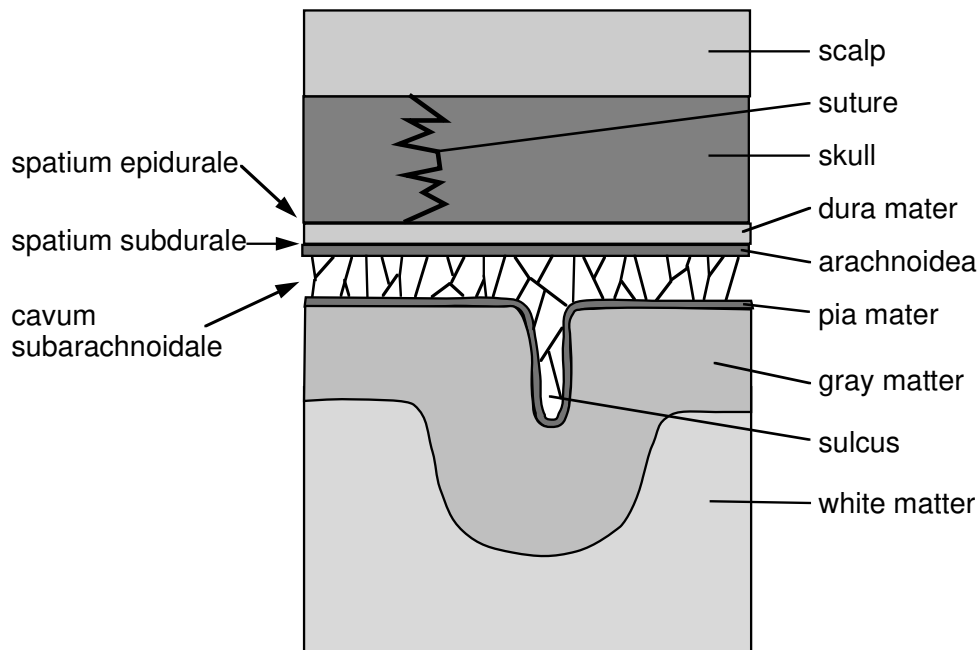
Figure 6.1: Schematic anatomy of the brain membranes.

the *arachnoidea*, it is separated from the dura mater by the *spatium subdurale*. Both spatium subdurale and spatium epidurale are normally very thin capillary gaps. Below the arachnoidea is a relatively wide gap, the *cavum subarachnoidale*, which is filled with cerebrospinal fluid (CSF). The brain floats in this fluid and is held in a central position by fibrous structures, which connect the arachnoidea with the third brain membrane, the *pia mater*. The pia mater directly covers the brain and follows the complex geometry of the *sulci*, which are slit–like indentations in the brain.

The dimensions of the different structures vary from patient to patient. The width of the cavum subarachnoidale is typically on the order of 2 mm. However, the width is age dependent because the volume of the brain decreases with age. The thickness of the skull varies not only individually, but also for different locations on the head. Figure 6.2 on page 117 shows a computer tomography of a normal head. The exposure was chosen to show the details of
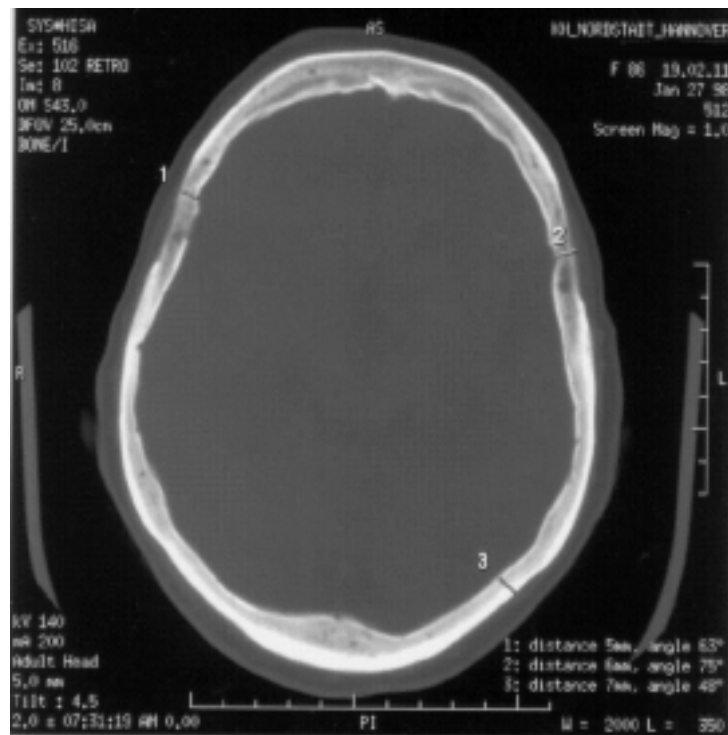
Figure 6.2: Computer tomography of the normal anatomy.

the bone structure, therefore the inner structures of the brain are not visible. It can be seen that the bone thickness varies significantly, the markers show thicknesses between 5 mm and 7 mm, as a typical value we can assume 6 mm. A realistic value for the scalp thickness is about 4 mm, so that we can assume 1 cm as a typical value for the total thickness of the combined scalp and skull layer.

6.2.2   Pathology of Intracranial Hematomas

Four types of intracranial hematomas can be distinguished: epidural, subdural, subarachnoidal, and intracerebral hematomas. Figure 6.3 shows schematic drawings of the anatomy and Fig. 6.4 shows typical CT scans.   Now to a description of the different hematoma types:
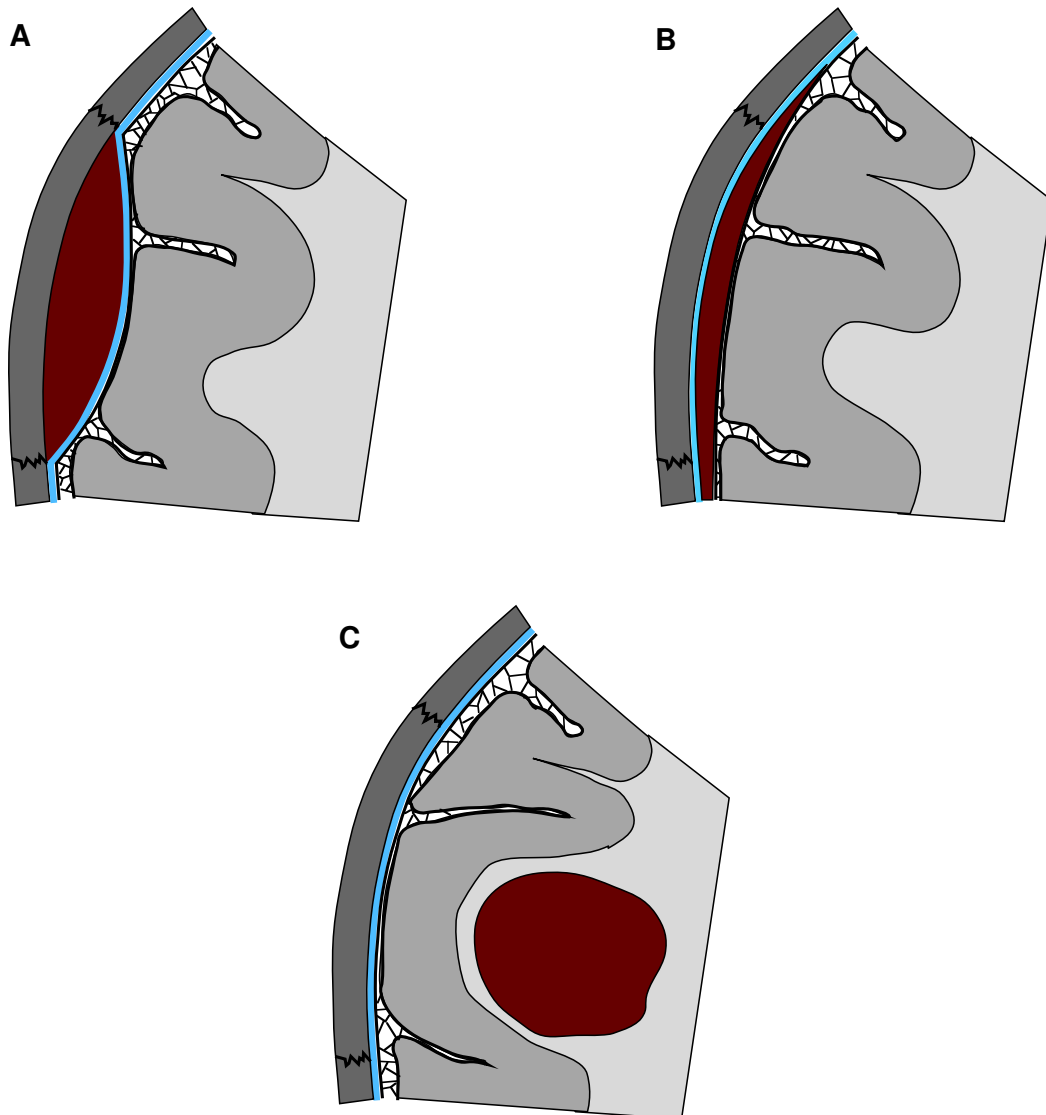
Figure 6.3: Intracranial hematomas: A epidural, B subdural, C intracerebral. For a legend of the structures see Fig. 6.1.

- **Epidural hematomas**

  are located between the skull and the dura mater in the spatium epidurale. They are mostly caused by ruptured arteries. Since the dura mater is connected to the skull at the sutures between the bone plates the blood cannot spread freely. This confinement often causes a typical biconvex shape, as shown in Fig. 6.3 A. This can also be seen in the top left CT
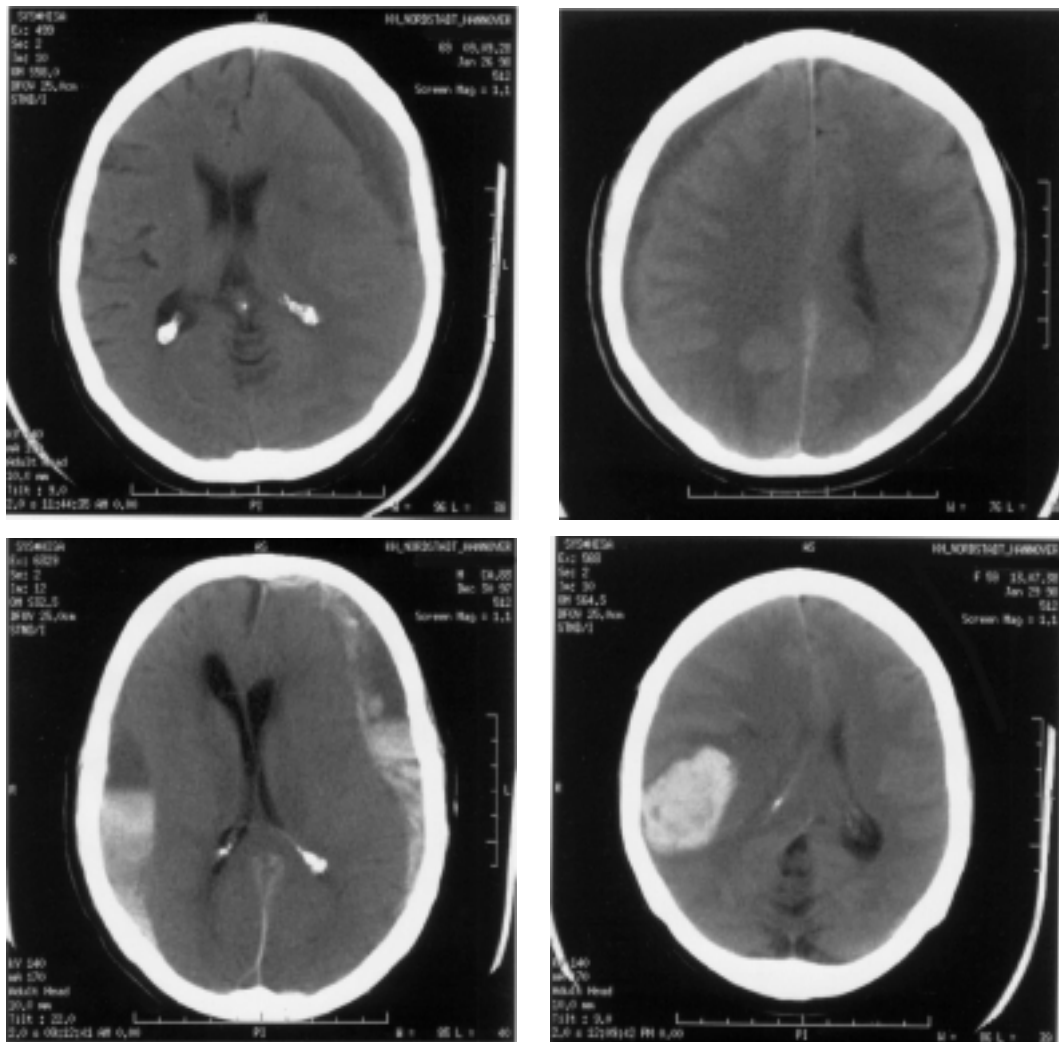
Figure 6.4: Computer tomographies of the three most common types of traumatic brain hematomas. Top left: epidural hematoma; top right and lower left: subdural hematoma; lower right: intracerebral hematoma

scan in Fig. 6.4.

- **Subdural hematoma**

  are located between the dura mater and the arachnoidea in the spatium subdurale. They are mostly caused by ruptured veins. The arachnoidea is not connected to the skull at the sutures, the blood can spread freely in the spatium subdurale. Subdural hematomas are therefore usu-

ally extended but relatively thin. If the blood volume is not too large the hematoma has typically a convex–concave shape, as can be seen in Fig. 6.3 B and in the top right CT scan in Fig. 6.4. For large blood volumes, however, the shape can also be biconvex, as in the CT scan on the lower left. The color separation in these relatively old hematomas is caused by metabolic change and separation of the blood.

- **Subarachnoidal hematomas**

  are located below the arachnoidea in the cavum subarachnoidale where the blood can mix with the cerebrospinal fluid. The majority of traumatic subarachnoidal hematomas occur in conjunction with subdural and epidural hematomas, we therefore do not treat them separately.

- **Intracerebral hematomas**

  are located inside the parenchyma of the brain. A typical CT scan is shown in the lower right image of Fig. 6.4. We expect that intracerebral hematomas can squeeze the cerebrospinal fluid out of the subarachnoidal cavity if the lesion is close enough to the skull and if the blood volume of the hemorrhage is large enough. This situation is depicted in Fig. 6.3 C. Note that this is a (reasonable) hypothesis, since the subarachnoidal space cannot be imaged with CT or magnetic resonance scans.

6.3 Head Optics

Based on the anatomical information from the last section we now model the light propagation in the head. Several approaches have been used to pursue this goal. The use of simple diffusion theory models is only appropriate for basic feasibility studies, like our example for transillumination with photon density waves in section 5.4. For the realistic quantitative modeling of light propagation in the adult head it is essential to take into account the light
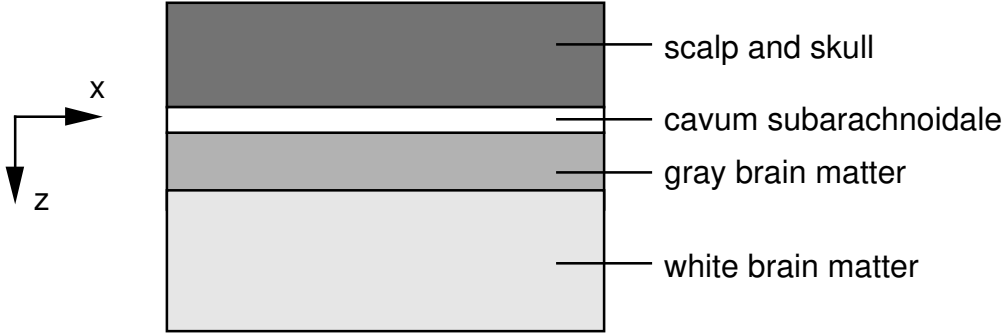
Figure 6.5: Four layer model of the head.

piping effect through the clear cerebrospinal fluid (CSF) in the subarachnoidal space. For this purpose Firbank *et al* have successfully employed Monte Carlo simulations [84] and more recently a hybrid approach which uses diffusion theory for the light propagation in the highly scattering tissues and a radiosity approach for the clear CSF layer[85]. Okada *et al* [63] have used these numerical techniques as well as experiments on phantoms to compare model systems for the head of different sophistication. The most complex geometry even modeled the sulci of the brain. The result was that this sophisticated model as well as the simpler multi layer models gave very similar results as long as a layer of the CSF was taken into account.

For our Monte Carlo simulations we therefore use a four layer model as depicted in Fig. 6.5 and will adapt it to the anatomy of brain hematomas as discussed in section 6.2. As standard values for the thickness of the layers we assume the following: scalp and skull 1 cm, subarachnoidal space 0.2 cm, gray brain matter 0.4 cm, and the white brain matter is, for simplicity, assumed to be infinitely thick. We will also vary these values in section 6.3.2.3.

6.3.1   Optical Properties

For the modeling we obviously have to assign optical properties to the layers. Although many studies have been devoted to the measurement of optical properties of biological tissues, it nevertheless still remains a challenging task to obtain accurate values of these properties in inhomogeneous *in vivo* systems. The difficulties arise from the combination of the attributes '*in vivo*' and 'inhomogeneous'.

Optical properties of inhomogeneous systems can be relatively easy obtained by making measurements, e.g. with the double integrating sphere method [86], on small samples of the different tissue types. However, obviously the excision of the samples automatically leads to *in vitro* measurements. The results of *in vitro* measurements are significantly influenced by the preparation of the samples. It is difficult to assure that the blood content, and with it the absorption coefficient, of the sample is the same as for the corresponding *in vivo* tissue. The scattering coefficient is also altered by the preparation, for example by freezing or fixation of the samples. Moreover, cell death itself alters the microstructure and thus the scattering coefficient. Experiments on rats have shown that the scattering coefficient of brain tissue changes about 15% in the instant of death [87]. This can be explained by the refractive index changes due to the depolarization of the axons. Thus values of *in vitro* measurements can be regarded only as approximate.

On the other hand, *in vivo* experiments are hindered by inhomogeneities as long as the algorithms for the estimation of the optical properties are based on simplified tissue models. If, as usual, a homogeneous medium is assumed, the deduced values can at best represent an average of the different tissue types. Strong deviations from the average, like for the clear cerebrospinal fluid, are expected to cause systematic errors. Another example for this type of

difficulties we have encountered in a study devoted to the *in vivo* measurement of optical properties in human and canine prostates [88, 89, 90], where the optical probe itself disturbed the light field and thus caused deviations.

When reviewing values given in the literature one also has to consider systematic deviations of different measurement types. For example, integrating sphere measurements tend to significantly overestimate the absorption coefficient of tissues with low absorption unless the integrating sphere losses are carefully calculated with iterative inverse Monte Carlo simulations [86].

Above we have only discussed the *uncertainties* of the measured values due to imperfect experimental or theoretical methods. But there are also *variations* of the real optical properties. It is known that the brains of neonates have a much lower scattering coefficient, thus the optical properties are age dependent, at least in the early childhood. How much the optical properties vary from individual to individual is difficult to estimate since differences in the measurements could also be explained by individual variations of the geometry. Beyond that, it is known that the optical properties in a single individuum are not constant. The optical detection of brain activity [72] is based on the fact that thinking alters the oxygen saturation, and thus the absorption coefficient. More relevant for our study is the reduction of the blood volume in the brain of patients who suffer from shock, this reduces the absorption coefficient. The scattering coefficient can also vary as a result of the administration of drugs to counteract brain swelling, because solutes like mannitol induce changes in refractive index and osmolarity [91].

In view of this multitude of difficulties it is not surprising that the values found in the literature have a significant spread. For near infrared light absorption coefficients between $\mu_a = 0.02$ cm^{-1} and $\mu_a = 3$ cm^{-1}, and reduced scattering coefficients between $\mu_s' = 9$ cm^{-1} and $\mu_s' = 60$ cm^{-1} have been reported [85, 39, 75].

Tissue	μ_a [cm^{-1}]	μ'_s [cm^{-1}]
Scalp and skull	0.3	20
Cerebrospinal fluid (CSF)	0.01	0.1
Gray matter	0.25	25
White matter	0.05	40
Whole blood	4	20

Table 6.1: Optical properties of the tissue types of the head.

For this study we use the values given in Tab. 6.1, (similar to those used by Okada *et al* [63]) as standard values. The refractive index of all tissue types as well as for CSF and blood is assumed to be $n = 1.4$. In section 6.3.2.3 we will consider the effects of variations of the optical properties.

6.3.2 Simulation of Light Propagation in the Head

Before we can discuss variations of geometry or optical properties, we first have to understand the basic contrast mechanism for the detection of hematomas. To this end we investigate the light propagation by computing sensitivity maps, or 'photon bananas'.

6.3.2.1 Photon Bananas

We have mentioned before that the clear CSF layer does not allow to use diffusion theory and the three point Green's function derived in chapter 3. We therefore resort to Monte Carlo simulations. To understand how photon bananas can be computed with Monte Carlo simulations it is helpful to first recall (see also section 2.2 on page 11) how a normal fluence distribution is

computed: The simulated photon–packets start with a certain photon weight and are propagated through the medium. At every interaction site the portion of the photon weight the packet has lost due to absorption on the small distance from the last interaction site is dropped in the collection grid. In this way the voxels of the collection grid accumulate photon weight, which is proportional to the absorbed energy density and thus to the light fluence.

For the computation of photon bananas this scheme is modified. The geometrical path of a photon package is intermediately stored in memory. Only the paths of photon packets who actually reach the detector are further processed, all other paths are discarded. When a photon packet reaches the detector its remaining photon weight is proportional to the probability of a single photon to survive this specific path without being absorbed. This probability is now added to all voxels the photon packet has visited on its path. In this way the collection grid accumulates the local visiting probability or photon hitting density of photons who actually do reach the detector. Note that a photon banana calculated in this way is the result of a statistical process. Only the average of many paths of detected photons yields a smooth probability distribution, for few detected photons the photon banana will look cloudy. Since the photon paths are smeared out over the whole volume of the photon banana but finally concentrate at the detector, the statistical error of the detector signal is much lower than the error at a volume element of the photon banana. Therefore, for a satisfying simulation of a photon banana considerably more photon packets are required than for the computation of the detector signal alone.

We had the opportunity to use a parallel Cray T3E supercomputer. Even with this massive computer power at hand the simulation of a measurement at the head is very demanding. To stay within reasonable computation time we used a model of the head with a thickness of the scalp and skull of 7 mm and a source detector separation of 3 cm. While these values are on the lower end of the expected values for the real measurement, the resulting photon bananas
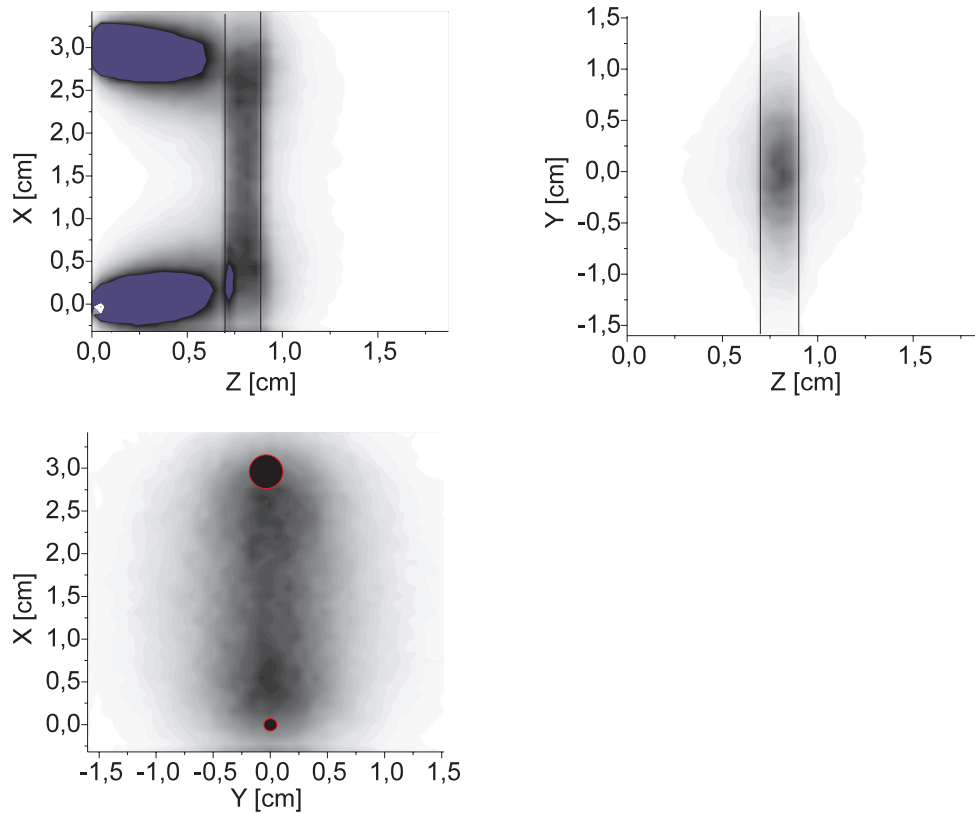
Figure 6.6:   Photon bananas for a model of the normal head with the clear layer of cerebrospinal fluid in the cavum subarachnoidale.

still give an accurate impression of the basic effects of the layered system on the photon propagation. Even for this small model each of the photon bananas we discuss below required the simulation of 60 million photon packets.

In the following we compare photon bananas for three different configurations. Figure 6.6 shows the photon banana for our simplified model of the normal adult head, that is the layered system as depicted in Fig. 6.5, where the cavum subarachnoidale ($z = 0.7$ cm to 0.9 cm) is filled with cerebrospinal fluid. Figure 6.7 shows the photon banana for a subdural or epidural hematoma. For simplicity we use the same layer model as for the normal head, except that the CSF layer has been replaced by a layer of blood. Figure 6.8 shows the photon banana for a head model *without* CSF or blood layer, where the scalp and skull
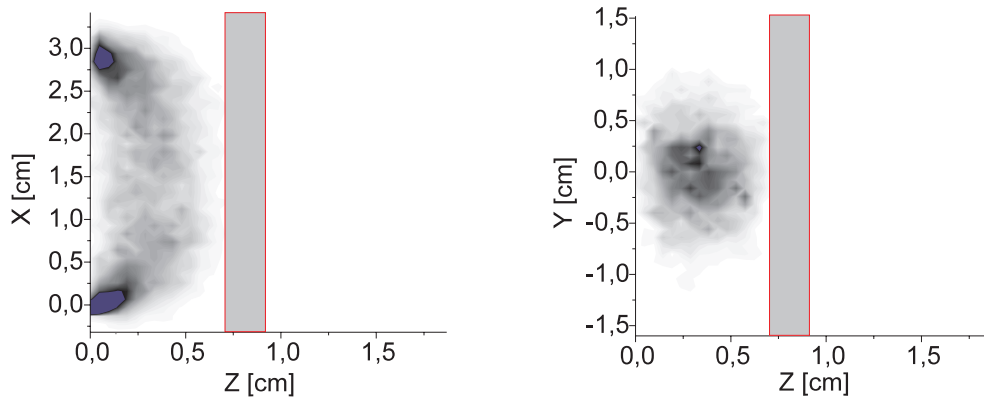
Figure 6.7:   Photon bananas for a model system of a subdural or epidural hematoma with a strongly absorbing layer of blood instead of the CSF layer in Fig. 6.6.

layer is directly on top of the gray brain matter. This models the situation in Fig. 6.3 C, where the pressure induced by an intracerebral hematoma has pressed the cerebrospinal fluid out of the cavum subarachnoidale. We expect that this might also happen for other pressure inducing pathologies, like brain tumors or brain swelling after diffuse brain injury. As optical properties we used the standard values from Tab. 6.1 on page 124 for all configurations.

The images in Figs. 6.8 – 6.7 show cuts through the photon bananas. In the top left image the x–z–plane cuts through the photon banana at $z = 0$ cm and thus contains the source at $x = 0$ cm and the detector at $x = 3$ cm. The y–z–plane in the top right image cuts through the photon banana at $x = 1.5$ cm, which is half way between the source and the detector. The lower left images in Figs. 6.8 and 6.6 show the x–y–plane at a depth of $z = 0.8$ cm, which for Fig. 6.6 is in the center of the CSF layer ($z = 0.7$ cm to 0.9 cm), and for Fig. 6.8 is in the first millimeter of the gray brain matter. In Fig. 6.7 this image is missing since there were no photon paths in the highly absorbing blood layer.

The photon bananas show clearly how the presence of the clear CSF layer
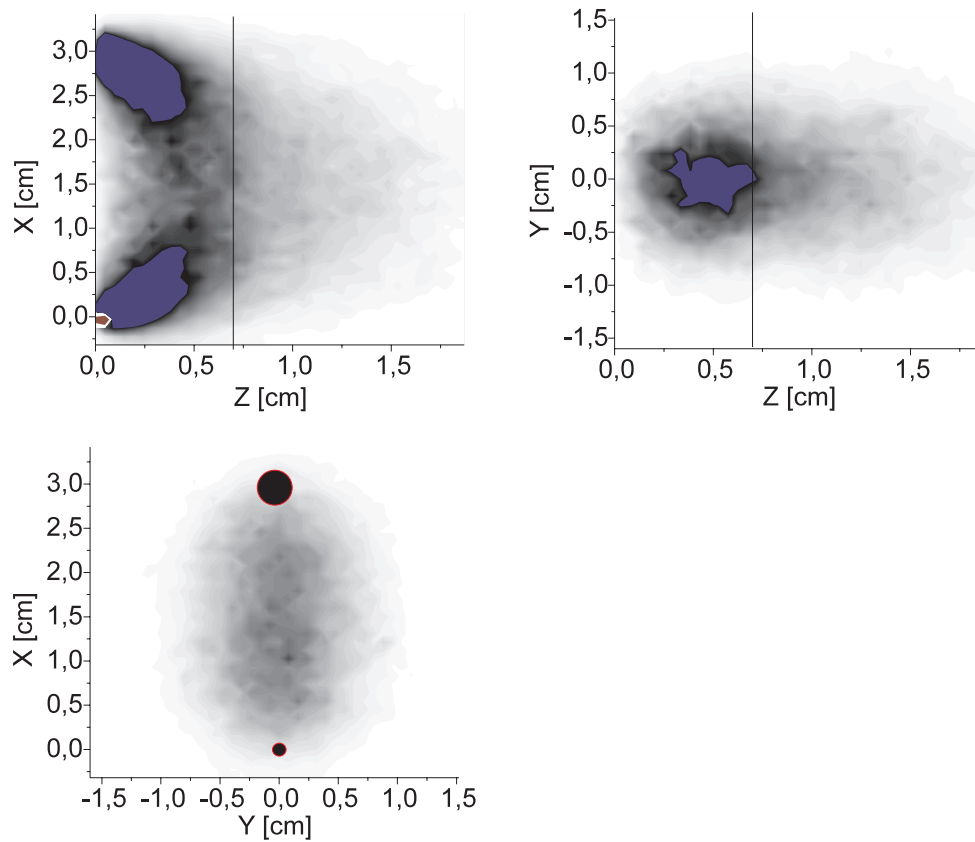
Figure 6.8: Photon bananas for a homogeneous medium. The solid line at a depth of z = 0.7 cm is intended to aid the comparison with the inhomogeneous systems in Figs. 6.6 and 6.7, where the layer of cerebrospinal fluid or blood begins at this depth.

in Fig. 6.6 results in a light piping effect with a high concentration of the photon paths in the clear layer. On the other hand, the blood layer in Fig. 6.7 blocks the deeper penetration of photons and confines the photon banana to the shallow region of the scalp and skull. Next we discuss how these different photon paths affect the detector signal.

Figure 6.9: Simulated detector signals for the normal head model (solid line) and the hematoma model (dashed line).

6.3.2.2 Light Piping

For a quantitative analysis of the light propagation in the three model geometries we have introduced in the last section it is necessary to consider the detectable signal at the surface of the head. Since the computation of the surface fluence is less demanding than the simulation of photon bananas we could afford to use a realistic head model with the typical thickness of 1 cm for the combined scalp and skull layer. The cavum subarachnoidale, either filled with cerebrospinal fluid (CSF) or with blood, is 2 mm thick, and the gray brain matter is 4 mm thick, below the white brain matter extends infinitely.

Figure 6.9 shows the surface fluence, which is proportional to the detector signal, as a function of the source detector distance. The fluence is shown for three situations, using the standard optical properties from Tab. 6.1: the normal head model with CSF layer (solid curve), the hematoma model with a

blood layer (dashed curve), and a setup without CSF or blood layer (dotted
curve). For small source detector distances all curves drop with a slope of two
and a half orders of magnitude per centimeter, i.e. 25 dB/cm. This behaviour
is expected and can be described by the normal diffusion theory solution for
semi–infinite media. Thus for small source detector separations the photon
banana does not reach deep enough into the medium to be influenced by the
presence of the CSF or blood layer. But at about 2 cm the signal for the
normal head model starts to deviate from the initial slope, and at distances
greater than 2.5 cm the light propagation is dominated by the light piping in
the clear CSF layer and the curve thus approaches a much shallower slope of
only 5 dB/cm. Contrary to this behaviour the signals for the hematoma model
as well as for the model without CSF or blood layer

For 3 cm source detector separation the curve for the normal head differs
already by an order of magnitude from the curves for the hematoma model as
well as and the difference increases rapidly with greater distance.

Thus according to our simple model the presence of a hematoma should be
detectable by simple DC absorption measurements provided that our assump-
tions about the geometry and the optical properties were correct. However, in
the last sections we have pointed out that both the geometry as well as the
optical properties are not well known and are expected to vary significantly.
Therefore the effects of these variations are discussed in the next section.

6.3.2.3 Variation of Optical Properties and Model Geometry

To explore the sensitivity of the detector signal to variations of the optical
properties we have repeated the simulations from the last section with different
optical properties of the tissue layers (i.e. scalp and skull, gray, and white
brain matter), while the optical properties of the CSF and blood layer were

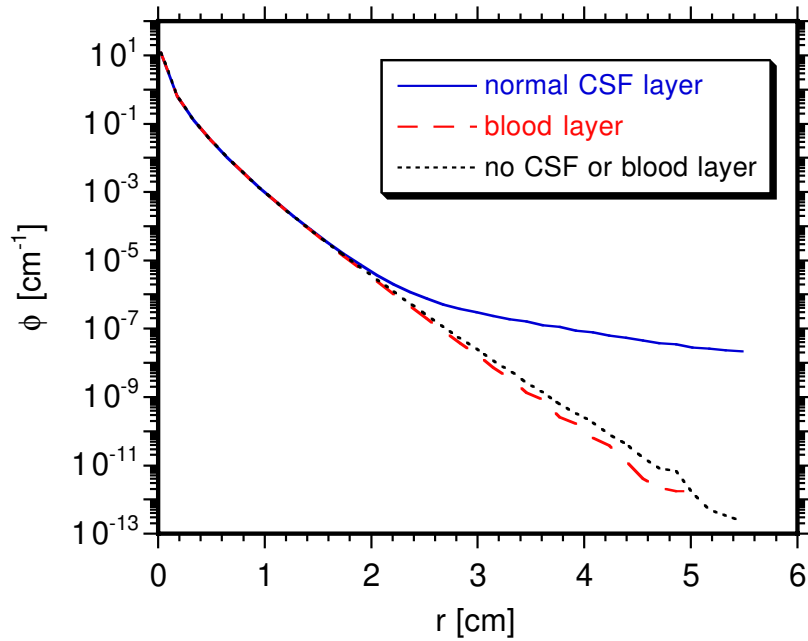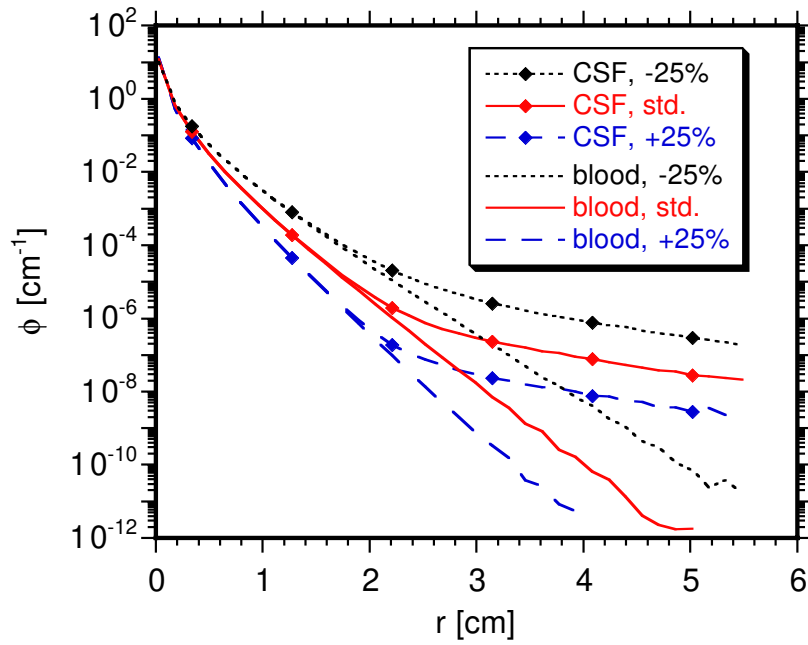*Figure 6.10: Simulated detector signals for the normal head model (solid lines) and the hematoma model (dashed lines). For each model the optical properties were varied by ±25 % around the standard values, for details see text.*

kept constant. One can go to considerable length by changing the absorption coefficient and the reduced scattering coefficient individually for each layer. For simplicity we restricted ourselves to two cases: the strong attenuation scenario where in all tissue layers μ_a and μ'_s were both increased by 25 %, and the low attenuation scenario, where μ_a and μ'_s were both decreased by 25 % with respect to the standard optical properties from Tab. 6.1. These variations are not very realistically in the sense that it is not probable that the measurement uncertainties and dynamic variations of both μ_a and μ'_s go uniformly in the same direction for all tissue types. Nevertheless, these two extreme cases provide a reasonable estimation of the maximum spread in the detector signal we can expect.

In Fig. 6.10 the results for both cases are shown together with the curves for the standard optical properties. The main difference is the slope for small source
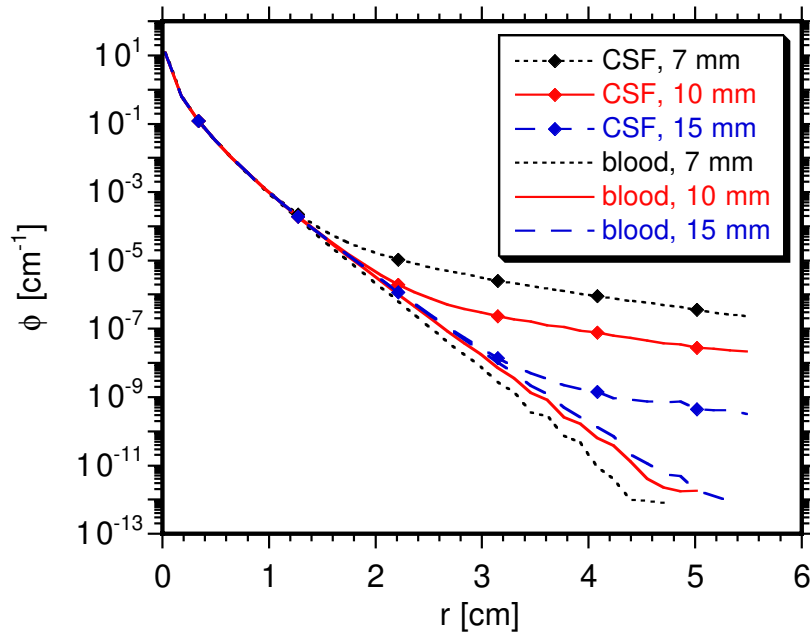
Figure 6.11: Simulated detector signals for a scalp and skull layer of varying thickness. Solid lines indicate the normal head model, dashed lines the hematoma model.

detector separations. This effect is expected since in this regime the photon banana is confined to the scalp and skull layer and thus fully experiences the different attenuation due to the changes in the optical properties. Somewhat surprising, the shallow slope of the signal for large source detector separations as well as the position of the transition is almost the same for all three sets of optical properties, which suggests that the light piping effect is relatively insensitive to variations of the tissue optical properties. Nevertheless, the resulting spread of the signal at large source detector distances is 20 dB for the normal head model and even greater for the hematoma model.

Next, we again use the standard optical properties, but vary the geometry of the layer model. Figure 6.11 shows the results for a variation of the thickness of the scalp and skull layer from 0.7 cm to 1.5 cm, which should cover the natural variations for adult heads. This variation has remarkably little effect
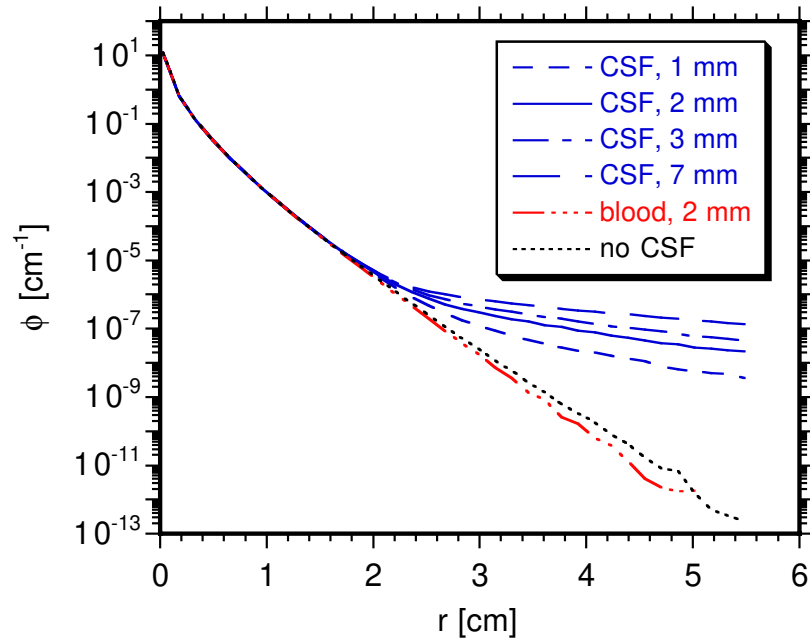
Figure 6.12: Simulated detector signals for varying thickness of the CSF or blood layer.

on the signal for the hematoma model. However, the signal for the normal head model changes significantly. The position of the transition between the steep and the shallow slope, indicating the onset of the light piping effect, is shifted toward larger source detector separations for increasing thickness of the upper scalp and skull layer. Effectively this results in a variation of the signal of about 20 dB for large source detector separations above 3.5 cm.

In Fig. 6.12 the thickness of the scalp and skull layer is set to the standard value of 1 cm and the thickness of the CSF layer is varied from zero to 0.7 cm. The thickness of the CSF layer determines the shallow slope for large source detector separations, while the position of the transition between the steep and the shallow slope does not change. It is remarkable how effective the light piping is, even the thin 1 mm CSF layer yields a 30 dB gain in signal at 5 cm source detector distance. Compared to this dramatic increase the subsequent change for thicker CSF layers is less pronounced.

6.4 Design of a Portable Optical Hematoma Detector

6.4.1 Choosing the Measurement Modality

The discussion of head optics in the last section suggests that spatially resolved measurements can be used to distinguish between the hematoma model and the normal head model, because the 'edge' – that is the suddenly changing slope – in the logarithmic plots is specific for the presence of the clear CSF layer. This is true even for the cases where the optical properties or the thickness of the scalp and skull layer have been changed, see Figs. 6.9 to 6.12. The 'edge' in the logarithmic plots can always be securely identified, regardless of the drastic changes in the magnitude of the signals. This is appealing because on first glance it suggests that the detection of hematomas will be independent from anatomical variations as well as from calibration errors of the device.

In the real head, however, the thickness of the scalp and skull changes over distances on the order of centimeters, see Fig. 6.2 on page 117. The influence of these changes on the detector signal would distort the different slopes and thus hinder the clear identification of the 'edge'. Beside these principal difficulties there are also some major practical drawbacks. The secure identification of a slope requires many measurements and thus many optodes. The head has a non–uniform curvature. Therefore a probe for spatially resolved measurements must provide a firm contact of *all* its optodes with some kind of elastic mounting or spring mechanism. This increases cost and complexity considerably and also makes sterilization cumbersome. Due to these difficulties we decided against a spatially resolved measurement mode.

Instead we employ attenuation measurements with a fixed source detector

distance. Figure 6.9 on page 129 shows that, for sufficiently large source detector separations, the presence of the CSF layer in the normal head model yields a dramatic increase in the detector signal, compared to the hematoma models without clear layer. Under ideal conditions absolute measurements with a source detector separation of, say, 4 cm could therefore easily identify hematomas. However, the simulations in the previous section show that the variations in geometry and optical properties we have to expect in practice make the choice of a decision threshold difficult. Consider Fig. 6.10 on page 131. At 4 cm source detector distance the curve for the normal head model with a 25% increase in optical properties and the curve for the hematoma model with a 25% decrease in optical properties cross each other. A thicker scalp and skull layer would push the intersection to even larger source detector distances. This makes clear that single absolute attenuation measurements cannot be used for a reliable diagnosis of hematomas as long as the variations of optical properties and anatomy cannot be taken into account.

Fortunately, these obstacles can be circumvented by taking *symmetrical* measurements on the same relative position on opposite sides of the head. In this approach we still cannot take the variations into account explicitly. Instead we utilize the fact that the anatomy of the normal head has a high degree of symmetry. This can be seen in the exemplary CT scan in Fig. 6.2 on page 117. Thus the difference of symmetrical measurements on a normal head is usually small because the effects of the natural anatomical variations cancel. We have verified this phenomenon with optical measurements on healthy volunteers, which will be discussed in more detail in section 6.5. A hematoma on one side of the head will break the symmetry and is therefore detectable with symmetrical difference measurements.

The study by Gopinath *et al* has shown that this approach indeed works well in a clinical setting. They used a relatively small source detector distances of 3.5 cm and later 4 cm [83]. For extracerebral hematomas they reported
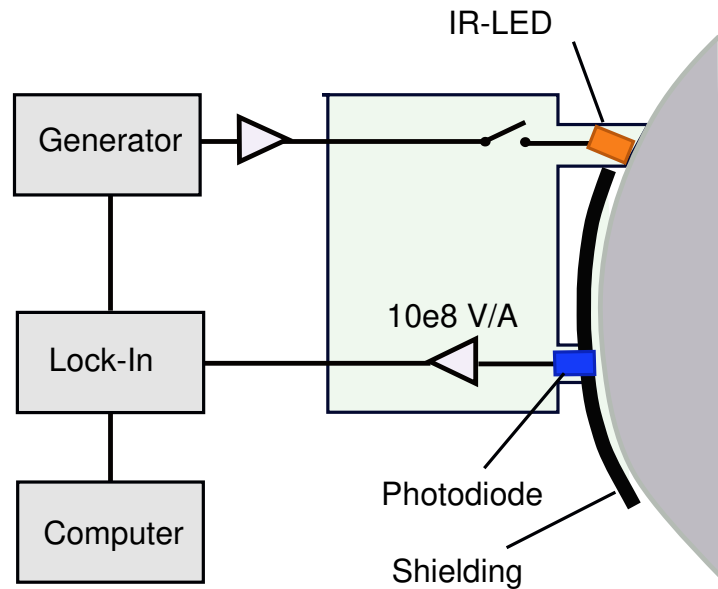
Figure 6.13: Simplified schematics of the optical probe.

signal differences of usually one and at most two orders of magnitude. For measurements under controlled conditions this margin is more than sufficient. However, for our target application in an emergency situation at the accident site we cannot assume controlled conditions. We anticipate that the restricted time slot for the examination and the often difficult conditions will lead to a less precise handling and positioning of the probe. This will cause increased error margins due to non symmetric measurements and imperfect contact of the probe. The design goal for our optical probe is therefore to increase the signal contrast between normal head and hematoma by increasing the source detector distance.

6.4.2   Detection Electronics

For large source detector distances very low light levels have to be detected. To achieve the required sensitivity we used lock-in techniques. Figure 6.13

shows a schematic of our detection system.

As light source we use two high power infrared luminescent diodes (Siemens SFH 485 P), which emit about 20 mW optical power at a wavelength of 880 nm. The diode current and thus the optical power is modulated at a frequency of 25 Hz. Due to the wide angle beam profile of about $\pm 20^o$ the radiation does not exceed the safety limits for skin and eye, the device is therefore safe for the application on humans.

For the detector several options are available. Photomultipliers and avalanche photodiodes are commonly used for low level light detection because their intrinsic low noise amplification allows for lower gain in the subsequent amplifier stages and thus improves the overall signal to noise ratio. However, both photomultipliers and avalanche photodiodes need a high voltage power supply. For our application this has two disadvantages. First, even a small high voltage module adds additional volume to the system, which is undesirable for a battery driven hand held device. Second, high voltage in a device with direct contact to the human body poses a potential risk. We therefore decided to use a conventional silicon photodiode (Hamamatsu S2386-45K), which requires no high voltage biasing. As a consequence of the lacking intrinsic amplification of photodiodes the following preamplifier has to be very sensitive. We have built a transimpedance amplifier with a transimpedance gain of 10^8 Ω. The spectral noise density of the amplifier is 12 fA/$\sqrt{\text{Hz}}$, which is the theoretical limit due to the thermal noise of the feedback resistor. The capacitance of the photodiode causes excess noise which yields an overall noise density of the combined system of photodiode and preamplifier of about 20 fA/$\sqrt{\text{Hz}}$ at 25 Hz.

6.4.2.1 First Prototype

In our initial experiments a conventional lock-in amplifier (EG&G Model 5105) was used. The system was controlled with a notebook computer, which also recorded the results. The simulations have shown that a bleeding causes a dramatic reduction of the signal. This can only be securely identified if the signal to noise ratio is large enough for the smallest signal occurring for a normal head. We therefore conducted measurements on healthy volunteers in order to find the optimal source detector distance. As expected the signal varied significantly depending on the position of the measurement. We found that the smallest signal occurred at the occipital and parietal positions on the rear head. At these positions a sufficiently large signal to noise ratio of about 20 dB was obtained with a time constant of one second and a source detector separation of 5.5 cm. While a larger time constant would allow for an even larger source detector separation, the increased settling time would be very inconvenient. We therefore chose a source detector separation of 5.5 cm and incorporated the infrared LEDs, the photodiode, and the preamplifier in a small sensor head. A black rubber pad was placed around the source and extended to the detector in order to shield the detector from ambient light and also to prevent a light leakage from source to detector. With this system we made a series of measurements to test the handling of the probe and to asses the repeatability of the difference signal, see section 6.5.

6.4.2.2 Second Prototype

Although the first system was already portable it required line power and was also far too bulky for an application in an emergency situation. We therefore built a prototype of a battery powered handheld device, which includes a generator for the modulation of the LEDs, a single phase lock-in amplifier, a
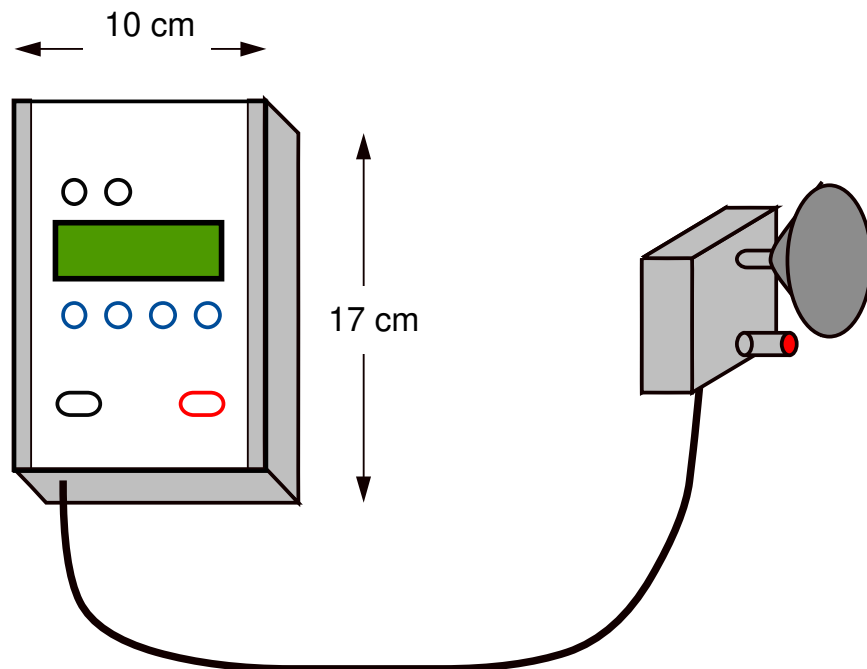
Figure 6.14: The second prototype of the optical hematoma detector.

microcontroller, a small LCD display, and a keyboard. All components are self designed, we employed the usual high precision low noise circuit techniques [92]. The sensitivity is the same as with the commercial lock-in amplifier we used in the first prototype. The measurements are directly displayed in logarithmic units and are thus easy to interpret.

Figure 6.14 gives an impression of the device. The main unit has a size of 10 x 17 x 5 cm, the sensor head measures 6 x 7 x 2.5 cm. The system is easy to handle, truly portable, and rugged. It thus meets all requirements for an application in emergency medicine.
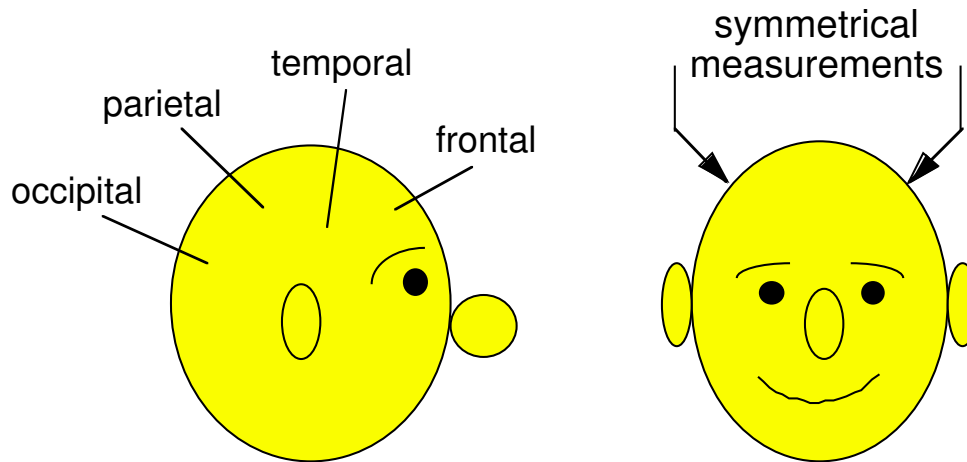
Figure 6.15: Measurement positions on the head.

6.5 First Results

We have used the probe on volunteers from our group in order to evaluate the handling of the device, find the appropriate measurement procedure, and to establish a signal range for measurements on normal heads.

We found that the probe is generally easy to handle and that the examination caused no inconvenience. To achieve reproducible results it is important to ensure a firm contact between optodes and skin. Since hair between either optode and the skin significantly attenuates the signal it is important to carefully part the hair when placing the optodes. From a scientific point of view it would be ideal to shave the measurement area. However, besides the fact that this would prolong the examination, it is clear that the cosmetic implications are not acceptable for patients who turn out to have no hematoma.

Even with firm contact of the probe and no interference from hair the signal still varies significantly for different positions on the head. Figure 6.15 indicates the measurement positions we used. There are also noticeable differences between individuals. The signal range for our group of volunteers (male, caucasian skin
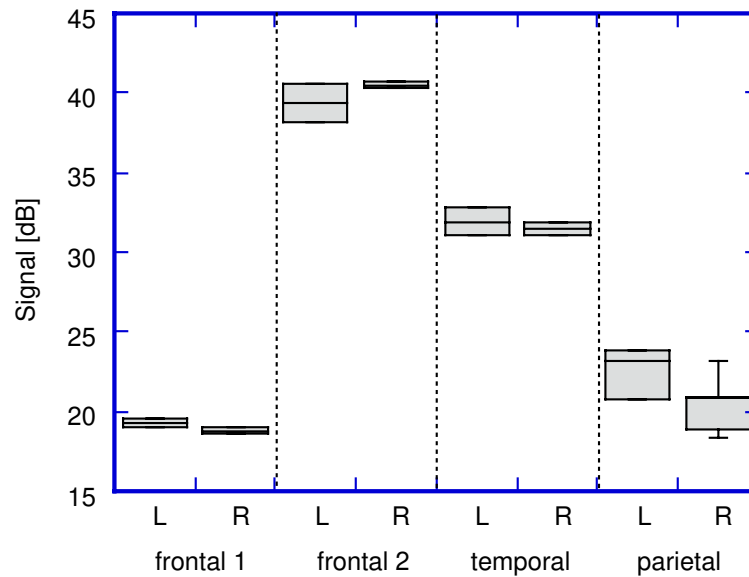
Figure 6.16: Typical symmetrical measurements on a healthy volunteer.

type, age 25–35) was between 15 and 40 dB. The decibel scale is referenced to 10^{-14} A, which marks a signal to noise ratio of one. Occasional tests on older persons yielded even higher signals. This was expected, since the thickness of the CSF layer becomes larger with age.

The large spread of the signal agrees with the results of our Monte Carlo simulations in section 6.3.2.3 and thus supports the validity of our model. As expected, symmetrical measurements can be used to reduce the variations significantly. Figure 6.16 shows a typical measurement on the head of a volunteer. The differences between the measurements on the right and left side at the same relative position do not exceed 5 dB. Such a small difference signal for the normal head should easily allow for a secure detection of asymmetric hematomas, which are expected to cause a decrease of the signal of at least 25 dB (see Fig. 6.11 on page 132).

However, consider the measurements for two different positions on the frontal

lobe of the head in Fig. 6.16. While the difference between the right and left side of the same position is small, the signal for the two positions differs by about 20 dB. The high signal for the 'frontal 2' position is caused by the air filled sinus in the frontal head, which acts as a very effective light piping mechanism. Contrary to that, position 'frontal 1' was higher on the head, where the sinus had no influence. This drastic change in signal for only a moderate variation of the measurement position emphasizes the need for a careful examination with a precise placement of the optodes. Fortunately the signal changes for other positions on the head are far less pronounced since light piping in the sinus is a unique feature of the frontal lobe of the head. Nevertheless we found that attention to the proper position and some practice in the correct placement of the optodes significantly increase the precision of the measurements.

Chapter 7

Conclusion

In the first part of this work we have given a comprehensive account of the theory of diffusive light propagation in inhomogeneous scattering media like biological tissues. It is applicable to frequency domain and steady state systems and properly treats absorbing as well as scattering inhomogeneities.

In chapter 3 we have discussed the solution of the differential photon diffusion equation for a spherical inclusion with a multipole expansion method. For objects smaller than about 4 mm in diameter it is usually appropriate to use the limiting form of this solution for small inhomogeneities. It can efficiently be used to explore the sensitivity of measurements to perturbations. The resulting sensitivity maps, also called 'photon bananas', can be utilized for the design of diagnostic methods. We have extended the concept of the sensitivity maps to scattering perturbations. Since the penetration of light in tissue is limited to about 5 cm, most diagnostic applications are restricted to reflection mode measurements. We have therefore explored sensitivity maps for the reflection mode. We found that despite the distinctive dipole pattern of scattering perturbations the shape of the sensitivity maps for scattering perturbations is on first glance remarkably similar to those for absorbing perturbations. For

absorption perturbations the sensitivity depends strongly on the modulation frequency: the lower the frequency the further the sensitive region penetrates into the tissue. Contrary to that, the maximum of the sensitivity for scattering perturbations only depends on the source detector distance, but not on the modulation frequency.

Unfortunately, neither the exact solution for a spherical object nor the approximation for small objects are an adequate description for many biological systems, because the encountered inhomogeneities are often extended but not of spherical geometry. In chapter 4 we have therefore developed a perturbation theory that overcomes the limitations of the multipole approach by using the integral formulation of the photon diffusion equation. It can conveniently be described in terms of a virtual source formalism. Absorbing perturbations are described by a volume distribution of virtual sources which causes a perturbation with a dominant monopole pattern. Scattering perturbations have an additional contribution that for sharply bounded objects is reduced to a surface distribution of virtual sources. This causes a dipole-like virtual source pattern, whose orientation is determined by the direction of the illuminating light.

For weak perturbations the distribution of the virtual sources can be directly computed form the distribution of the absorption and scattering perturbations, and from the incoming unperturbed light field (Born approximation). For small perturbations, the virtual source formalism is then equivalent to the limiting form of the multipole expansion solution from chapter 3. For stronger and extended perturbations, however, the problem becomes nonlinear. The reason is that for strong perturbations it is no longer appropriate to use the unperturbed light field to calculate the virtual sources. An iterative scheme is then used to improve in turn the perturbed light field and the virtual source distribution. Effectively, this takes the self shadowing of the objects into account.

An important property of the virtual source formalism is the fact that, although the actual solution is an iterative procedure, the formal solution nevertheless provides a deep insight into the nature of diffusive light transport. This enabled us to address some issues of relevance for inverse problems. We have found that for low modulation frequencies and a fixed source position, the virtual source distributions for weak scattering and absorption perturbations can be exactly the same. This result emphasizes the importance of different source positions in measurements for tomographic reconstructions or, if that is not possible, high modulation frequencies. Another result is that the detector placement in measurements influences the detectability of object surfaces. Towards the light source the perturbation due to the surface is most pronounced. As a consequence, reflection measurements are especially sensitive to the surface of scattering objects.

In chapter 5 we have discussed the numerical implementation of the virtual source formalism. The resulting 'SVS' algorithm (Superposition of Virtual Sources) is a flexible tool for the fast simulation of light transport in systems with complex and extended inhomogeneities. It is thus well suited for dosimetry calculations in therapeutic applications. Besides this direct application of the method as a forward algorithm our analysis also yielded interesting consequences for the inverse problem, i.e. for tomographic reconstruction techniques. We showed that the proper discretization of the integral equation yields a self interaction term which accounts for the influence of a perturbation on its own illumination. Currently this term is neglected in inversion algorithms. Our analysis has shown, however, that for the often used coarse discretization grids this term can yield an important contribution that should not be neglected. Coarse discretization grids also cause special problems for the modeling and reconstruction of scattering perturbations. In chapter 5 we had found that the virtual sources on the surface of a scattering perturbation can principally lead to a high edge contrast in reconstruction algorithms. But the same feature

also poses a problem for the numerical accuracy, because the discretization of the volume has to be fine enough to avoid large discretization errors. This phenomenon is not unique to our forward algorithm, but applies as well to all tomographic reconstruction algorithms for diffusive light transport.

For future work, three avenues seem promising: (i) The numerical efficiency of the SVS algorithm can be improved by using a variable grid size, which adapts to the geometry of the problem. Another possibility is to use several grid sizes simultaneously, similar to the multigrid methods for finite difference algorithms. The coarse grid is used for the long distance interaction, while the fine grid mediates the short distance interaction and can model the details of the light field in complex geometries. (ii) The SVS algorithm can be used as the forward model in an iterative inversion algorithm for optical tomography. The SVS algorithm is not restricted to the linear range of weak perturbations, but can model the nonlinear interaction between stronger perturbations. Used as part of an inversion algorithm this feature is expected to improve the accuracy of tomographic reconstructions. (iii) Another interesting challenge for further research will be to adapt the virtual source formalism to the time domain.

The second part of this work was devoted to the detection of traumatic brain hematomas with optical reflection mode measurements. Diffusion theory cannot be used to model the light propagation in the head because the presence of the clear layer of cerebrospinal fluid (CSF) between skull and brain leads to a light piping effect. We therefore could not use the virtual source formalism, but had to resort to Monte Carlo simulations. Somewhat surprisingly, this showed that the detector signal is not very sensitive to the presence of a hematoma by itself. Instead the blockage of the light piping in the clear CSF layer is the dominant contrast mechanism. This can be caused either by epidural and subdural hematomas, which directly replace the CSF layer, or by intracranial hematomas, which squeeze the CSF out of the cavum subarachnoidale due to the locally increased intracranial pressure. The quantitative results of simula-

tions for variations of the geometry and the optical properties showed that it is important to use symmetric measurements on both sides of the head. Furthermore, for a secure identification of hematomas it is desirable to use the source detector separation as large as possible. However, this requires a very sensitive detection system with a wide dynamic range.

Based on these criteria we have built a prototype of an optical hematoma detector. It incorporates a modulated infrared luminescence diode, a silicon photodiode, a lock–in amplifier, and a microprocessor in a rugged, portable, battery driven device. The device is easy to handle, which is important for an application in emergency vehicles and at accident sites.

To validate the technique we plan to test our device in a clinical study at the Department of Neurology at the Nordstadt Krankenhaus Hannover. In the first phase of the study it is planned to use the probe in conjunction with CT scans. In this controlled clinical environment the handling and reliability of the probe can be tested and valuable information for further improvements can be gathered. At this stage patients with a variety of conditions will be included in the trial, i.e. patients with hematomas, diffuse brain injury, stroke, and tumors. In this way the specificity of our approach can be assessed. We expect that parallel to the first phase of the study the practical experience will lead to further improvements of the device. In the second phase it is planned to use the improved probe in emergency vehicles and directly at accident sites.

A proposal for the clinical trial has been submitted to the ethics committee of the state of Lower Saxony, the approval is currently pending.

Bibliography

[1] G. M. Hale and M. R. Querry. Optical constants of water in the 200-nm to 200-μm wavelength region. *Applied Optics*, 12:555, 1973. 2

[2] S. Wray, M. Cope, D.T. Delpy, J.S. Wyatt, and E. Reynolds. Characterization of the near infrared absorption spectra of cytochrome aa3 and haemoglobin for the non-invasive monitoring of cerebral oxygenation. *Biochemica et Biophysica Acta*, 933:184, 1988. 2

[3] A. Ishimaru. *Wave Propagation and Scattering in Random Media*. Academic Press, New York, 1978. Reissued by IEEE Press and Oxford University Press 1997. 7, 10, 11, 78

[4] M. Ostermeyer, D. V. Stephens, L. Wang, and S. L. Jacques. Nearfield polarization effects on light propagation in random media. In E. Sevick-Muraca and D. Benaron, editors, *OSA TOPS on Biomedical Optical Spectroscopie and Diagnostics*, volume 3, pages 20–25, 1996. 7

[5] S. L. Jacques, D. Stephens, M. Ostermeyer, and L. Wang. Polarized light transmission through skin using video reflectometry: toward optical tomography of superficial tissue layers. volume SPIE 2671, 1996. 7

[6] S. Bartel. Polarisationsabhängige Lichtausbreitung in stark streuenden Medien. Diplomarbeit, Universität Hannover, Germany, 1998. 7

[7] H. C. van de Hulst. *Light Scattering by Small Particles*. Dover Publications, Inc., New York, 1981. 8, 10

[8] J. Beuthan, O. Minet, J. Helfmann, M. Herring, and G. Müller. The spatial variation of the refractive index in biological cells. *Phys. Med. Biol.*, 41:369–382, 1996. 8

[9] J. M. Schmitt and G. Kumar. Turbulent nature of refractive-index variations in biological tissue. *Opt. Lett.*, 21:1310–1312, 1996. 8

[10] S. Chandrasekhar. *Radiative Transfer*. Oxford University Press, London, New York and Dover, 1960. 10

[11] S. L. Jacques, C. A. Alter, and S. A. Prahl. Angular dependence of hene laser light scattering by human dermis. *Lasers Life Sci.*, 1:309, 1987. 10

[12] L. G. Henyey and J. L. Greenstein. Diffuse radiation in the galaxy. *Astrophys. J.*, 93:70, 1941. 11

[13] K. M. Case and P. F. Zweifel. *Linear Transport Theory*. Addison-Wesley, Reading, Mass., 1967. 11, 11, 13

[14] L. Wang, S. L. Jacques, and L. Zheng. Mcml – monte carlo modeling of light transport in multi–layered tissues. *Computer Methods and Programs in Biomedicine*, 47:131, 1995. 12, 103

[15] S. L. Jacques and L. Wang. Monte carlo modeling of light transport in tissues. In *Optical–Thermal Response of Laser–Irradiated Tissue*, chapter four. Plenum Press, New York, 1995. 12

[16] I. Lux and L. Koblinger. *Monte Carlo Particle Transport Methods: Neutron and Photon Calculations*. CRC Press, 1991. 12

[17] M. Keijzer. *Light Transport for Medical Laser Treatments*. PhD thesis, Technical University Delft, The Netherlands, 1993. 13

[18] D. A. Boas. *Diffuse Photon Probes of Structural and Dynamical Properties of Turbid Media: Theory and Biomedical Applications*. PhD thesis, University of Pennsylvania, USA, 1996. 13, 31, 57, 58, 102, 163

[19] K. Furutsu and Y. Yamada. Diffusion approximation for a dissipative random medium and the applications. *Physical Review E*, 50(5):3634–3640, 1994. 16

[20] Y. Yamada. Diffusion coefficient in the photon diffusion equation. In *Proc. SPIE*, volume 2389, pages 87–97, 1995. 16

[21] D. Contini, F. Martelli, and G. Zaccanti. Photon migration through a turbid slab described by a model based on diffusion approximation. 1. theory. *Applied Optics*, 36(19):4587–4599, 1997. 16, 19, 21, 24

[22] M. Bassani, F. Martelli, and G. Zaccanti. Independence of the diffusion coefficient from absorption: experimental and numerical evidence. *Optics Letters*, 22(12):853, 1997. 16

[23] B. J. Tromberg, L. O. Svaasand, T. T. Tsay, and R. C. Haskell. Properties of photon density waves in multiple–scattering media. *Appl. Opt.*, 32:607, 1993. 18

[24] H. Li and S. Xie. Measurement of the refractive index of biotissue by total internal reflection. *Applied Optics*, 35:1793, 1996. 19

[25] R. A. Groenhuis, H. A. Ferwerda, and J. J. ten Bosch. Scattering and absorption of turbid materials determined from reflection measurements. 1. theory. *Applied Optics*, 22:2456, 1983. 19, 21, 22

[26] M. Keijzer, W. M. Star, and P. R. M. Storchi. Optical diffusion in layered media. *Applied Optics*, 27:1820, 1988. 19, 21, 22

[27] M. S. Patterson, B. Chance, and B. C. Wilson. Time resolved reflectance and transmittance for the noninvasive measurement of tissue optical properties. *Appl. Opt.*, 28:2331, 1989. 19, 24, 87

[28] T. J. Farrell, M. S. Patterson, and B. Wilson. A diffusion theory model of spatially resolved, steady-state diffuse reflectance for the noninvasive

determination of tissue optical properties in vivo. *Med. Phys.*, 19:879, 1992. 19, 21, 22, 24

[29] R. C. Haskell, L. O. Svaasand, T.-T. Tsay, T.-C. Feng, M. S. McAdams, and B. J. Tromberg. Boundary conditions for the diffusion equation in radiative transfer. *J. Opt. Soc. Am. A*, 11:2727, 1994. 19, 19, 20, 21, 21, 24

[30] R. Aronson. Boundary conditions for diffusion of light. *J. Opt. Soc. Am. A*, 12:2532, 1995. 19

[31] S. R. Arridge, M. Cope, and D. T. Delpy. The theoretical basis for the determination of optical pathlengths in tissue: temporal and frequency analysis. *Phys. Med. Biol.*, 37:1531, 1992. 19, 24, 87

[32] S. R. Arridge. Photon–measurement density functions. part 1: Analytical forms. *Appl. Opt.*, 34:7359, 1995. 24, 41

[33] M. S. Patterson, S. Anderson-Engels, B. C. Wilson, and E. K. Osei. Absorption spectroscopy in tissue–simulating materials: a theoretical and experimental study of photon paths. *Appl. Opt.*, 34:22, 1995. 24, 40

[34] J. D. Jackson. *Classical Electrodynamics*. Wiley and Sons, Inc., New York, 1975. 29

[35] D. A. Boas, M. A. O'Leary, B. Chance, and A. G. Yodh. Scattering of diffuse photon density waves by spherical inhomogeneities within turbid media: Analytic solution and applications. *Proc. Natl. Acad. Sci. USA*, 91:4887–4891, 1994. 29, 31, 163

[36] A. H. Hielscher, F. K. Tittel, and S. L. Jacques. Photon density wave diffraction tomography. In R.R. Alfano, editor, *OSA proceedings on Advances in Optical Imaging and Photon Migration*, volume 21, pages 78–82, 1994. 29

[37] G. Arfken. *Mathematical Methods for Physicists.* Academic Press, San Diego, Ca., fourth edition, 1995. 29, 61, 62, 62, 81

[38] A. H. Hielscher. *Noninvasive Determination of Blood Oxigenation in the Brain by Near–Infrared Reflectance Spectroscopy.* PhD thesis, Rice University, USA, 1995. 31

[39] W.-F. Cheong. Appendix to chapter 8: Summary of optical properties. In A. J. Welsh and M. J. C. van Gemert, editors, *Optical-Thermal Response of Laser-Irradiated Tissue.* Plenum Press, New York, 1995. 37, 123

[40] J. C. Schotland, J. C. Haselgrove, and J. S. Leigh. Photon hitting density. *Appl. Opt.*, 32:448, 1993. 40

[41] E. M. Sevick, C. L. Burch, J. K. Frisoli, and J. R. Lakovicz. Locilization of absorbers in scattering media by use of frequency–domain measurements of time–dependent photon migration. *Appl. Opt.*, 33:3562, 1994. 40

[42] H. L. Graber, J. Chang, R. Aronson, and R. L. Barbour. A perturbation model for imaging in dense scattering media: Derivation and evaluation of imaging operators. In G. Müller, editor, *Medical Optical Tomography*, volume IS11, pages 121–143. SPIE Institutes, 1993. 40, 57

[43] S. R. Arridge and M. Schweiger. Photon–measurement density functions. part 2: Finite–element–method calculations. *Appl. Opt.*, 34:8026, 1995. 41, 105

[44] S. B. Colak, D. G. Papaioannou, G. W. 't Hooft, M. B. van der Mark, H. Schomberg, J. C. J. Paasschens, J. B. M. Melissen, and N. A. A. J. van Asten. Tomographic image reconstruction from optical projections in light–diffusing media. *Appl. Opt.*, 36:180–213, 1997. 42, 42

[45] S. Zhao, M. A. O'Leary, S. Nioka, and B. Chance. Breast tumor detection using continuous wave light sources. In B. Chance and R. Alfano, editors, *Optical Tomography, Photon Migration, and Spectroscopy of Tissue and*

Model Media: Theory, Human Studies, and Instrumentation, pages 809–817, 1995.   42, 71

[46] M. Kaschke, H. Jess, G. Gaida, J.-M. Kaltenbach, and W. Wrobel. Transillumination imaging of tissue by phase modulation techniques. In R.R. Alfano, editor, *OSA proceedings on Advances in Optical Imaging and Photon Migration*, volume 21, pages 88–92, 1994.   42, 58

[47] H. Heusmann, J. Kölzer, R. Puls, J. Otto, S. Heywang-Köbrunner, and W. Zinth. Spectral transillumination of human breast tissue. In B. Chance and R. Alfano, editors, *Optical Tomography, Photon Migration, and Spectroscopy of Tissue and Model Media: Theory, Human Studies, and Instrumentation*, volume 2389, pages 798–808, 1995.   42

[48] D.A. Benaron, J. P. Van Houten, W. F. Cheong, E. L. Kermit, and R. A. King. Early clinical results of time-of-flight optical tomography in a neonatal intensive care unit. In B. Chance and R. Alfano, editors, *Optical Tomography, Photon Migration, and Spectroscopy of Tissue and Model Media: Theory, Human Studies, and Instrumentation*, volume 2389, pages 582–596. SPIE, 1995.   42, 83, 113, 113

[49] D. A. Boas, M. A. O'Leary, B. Chance, and A. G. Yodh. Detection and charactization of optical inhomogeneities with diffuse photon density waves: a signal–to–noise analysis. *Appl. Opt.*, 36:75, 1997.   47

[50] Maureen A. Oleary. *Imaging with Diffuse Photon Density Waves*. PhD thesis, University of Pennsylvania, USA, 1996.   55, 68, 102, 163

[51] S. Feng, F. A. Zeng, and B. Chance. Photon migration in the presence of a single defect: a perturbation analysis. *Appl. Opt.*, 34:3826, 1995.   57, 67

[52] R. L. Barbour, H. L. Graber, R. Aronson, and J. Lubovsky. Imaging of subsurface regions of random media by remote sensing. In *SPIE*, volume 1431, pages 192–203, 1991.   57

[53] B. W. Pogue and M. S. Patterson. Perturbation calculations of photon density waves in an inhomogeneous tissue-simulating medium. In R.R. Alfano, editor, *OSA proceedings on Advances in Optical Imaging and Photon Migration*, volume 21, pages 74–77, 1994. 58

[54] S. R. Arridge, M. Schweiger, M. Hiraoka, and D. T. Delpy. Performance of an iterative reconstruction algorithm for near infrared absorption and scatter imaging. In *SPIE*, volume 1888, pages 360–371, 1993. 58, 58

[55] M. A. O'Leary, D. A. Boas, B. Chance, and A. G. Yodh. Experimental images of heterogeneous turbid media by frequency-domain diffusing-photon tomography. *Opt. Lett.*, 20:426–428, 1995. 58, 58, 59, 62, 69, 88, 163

[56] M. R. Ostermeyer and S. L. Jacques. Perturbation theory for diffuse light transport in complex biological tissues. *J. Opt. Soc. Am. A*, 14:255–261, 1997. 58, 67, 75

[57] M. R. Ostermeyer and S. L. Jacques. Perturbation theory for optical diffusion theory: a general approach for absorbing and scattering objects in tissue. In B. Chance and R.R. Alfano, editors, *Optical Tomography, Photon Migration, and Spectroscopy of Tissue and Model Media: Theory, Human Studies, and Instrumentation*, volume SPIE 2389, pages 98–102, 1995. 58

[58] M. R. Ostermeyer, A. H. Hielscher, L. Wang, and S. L. Jacques. Accelerated modeling of light transport in heterogenous tissues using superposition of virtual sources. In S. Avrillier, B. Chance, and G.J. Müller, editors, *Theoretical Study, Mathematical, Experimental Model for Photon Transport in Scattering Tissue*, volume SPIE 2326, pages 56–64, 1994. 58, 75

[59] S. L. Jacques, M. R. Ostermeyer, L. Wang, and A. H. Hielscher. Light dosimetry in pdt using optical fiber delivery. In *Optical Methods for Tumor*

Treatment and detection: Mechanisms and Techniques in Photo-dynamic Therapy III, volume SPIE 2133, pages 155–164, 1994. 58, 75

[60] S. L. Jacques, M. R. Ostermeyer, L. Wang, and A. H. Hielscher. Effects of sources, boundaries, and heterogeneities on photon migration. In R.R. Alfano, editor, *OSA proceedings on Advances in Optical Imaging and Photon Migration*, volume 21, pages 83–87, 1994. 58, 75

[61] M. A. O'Leary, D. A. Boas, B. Chance, and A. G. Yodh. Images of inhomogeneous turbid media using diffuse photon density waves. In R.R. Alfano, editor, *OSA proceedings on Advances in Optical Imaging and Photon Migration*, volume 21, pages 106–115, 1994. 62

[62] B. Chance, K. Kang, L. He, J. Weng, and E. Sevick. Highly sensitive object location in tissue models with linear in-phase and anti-phase multi-element optical arrays in one and two dimensions. *Proc. Natl. Acad. Sci. USA*, 90:3423–3427, 1993. 71

[63] E. Okada, M. Firbank, M. Schweiger, S. R. Arridge, M. Cope, and D. T. Delpy. Theoretical and exoerimental investigation of near–infrared light propagation in a model of the adult head. *Applied Optics*, 36:21–31, 1997. 103, 121, 124

[64] M. Schweiger and S. R. Arridge. Near–infrared imaging: Photon measurement density functions. In *Proc. SPIE*, volume 2389, pages 366–377, 1995. 105

[65] W. Pöll. Traumen. In W. Fröscher, editor, *Lehrbuch der Neurologie mit Repetitorium*, chapter 12. Walter de Gruyter, Berlin, New York, 1991. 110

[66] K. F. Masuhr and M. Neumann. *Neurologie.* Hippokrates Verlag, Stuttgart, 1989. 110, 110

[67] K. Kunze and H.-P. Neunzig. Neurotraumatologie. In K. Kunze, editor, *Lehrbuch der Neurologie*. Georg Thieme Verlag, Stuttgart, New York, 1992. 110

[68] M. Poremba. Schädelhirntrauma. In T. Brandt, J. Dichgans, and H. C. Diener, editors, *Therapie und Verlauf neurologischer Erkrankungen*. Verlag W. Kohlhammer, Stuttgart, Berlin, Köln, 1993. 111

[69] S. P. Gopinath, C. S. Robertson, C. F. Contant, R. K. Narayan, R. G. Grossman, and B. Chance. Early detection of delayed traumatic intracranial hematomas using near–infrared spectroscopy. *Journal of Neurosurgery*, 83:438–444, 1995. 113, 113

[70] F. F. Jöbsis. Noninvasive, infrared monitoring of cerebral and myocardial oxygen sufficiency and circulatory parameters. *Science*, 19:1264–1267, 1977. 113

[71] C. J. Aldrich, J. S. Wyatt, J. A. Spencer, E. O. R. Reynolds, and D. T. Delpy. The effect of maternal oxygen administration on human fetal cerebral oxygenation measured during labour by near infrared spectroscopy. *Br. J. Obstet. Gynaecol.*, 101:509–513, 1994. 113

[72] M. Fabiani, G. Gratton, and P. M. Corballis. Noninvasive near infrared optical imaging of human brain function with subsecond temporal resolution. *Journal of Biomedical Optics*, 1:387–398, 1996. 113, 123

[73] C Hirth, H. Obrig, K. Villringer, A. Thiel, J. Bernarding, W. Mühlnickel, H. Flor, U. Dirnagel, and A. Villringer. Non–invasive functional mapping of the human motor cortex using near–infrared spectroscopy. *NeuroReport*, 7:1977–1981, 1996. 113

[74] C Hock, K. Villringer, F. Müller–Spahn, M. Hofmann, S. Schuh–Hofer, H. Heekeren, R. Wenzel, U. Dirnagel, and A. Villringer. Near infrared spectroscopy in the diagnosis of alzheimer's desease. *Annals of the New York Academy of Sciences*, 777:22–29, 1996. 113

[75] E. M. Sevick, B. Chance, J. Leigh, S. Nioka, and M. Maris. Quantitation of time- and frequency-resolved optical spectra for the determination of tissue oxygenation. *Analytical Biochemistry*, 195:330–351, 1991. 113, 123

[76] M. Miwa, Y. Ueda, and B. Chance. Development of time resolved spectroscopy system for quantitative noninvasive tissue measurement. In B. Chance and R. Alfano, editors, *Optical Tomography, Photon Migration, and Spectroscopy of Tissue and Model Media: Theory, Human Studies, and Instrumentation*, pages 142–149, 1995. 113

[77] M. Kohl, R. Watson, and M. Cope. Optical properties of highly scattering media determined from changes in attenuation, phase, and modulation depth. *Appl. Opt.*, 36:105–115, 1997. 113

[78] S. Fantini, M. A. Franceschini–Fantini, J. S. Maier, S. A. Walker, B. Barbieri, and E. Gratton. Frequency–domain multichannel optical detector for noninvasive tissue spectroscopy and oxymetry. *Opt. Eng.*, 34:32–42, 1995. 113

[79] H. Lui, D. A. Boas, Y. Zhang, A. Yodh, and B. Chance. Determination of of optical properties and blood oxygenation in tissue using continuous nir light. *Phys. Med. Biol.*, 40:1983–1993, 1995. 113

[80] M. Cope. *The Development of a Near Infrared Spectroscopy System and its Application for Non Invasive Monitoring of Cerebral Blood and Tissue Oxygenation in the Newborn Infant.* PhD thesis, University College London, 1991. 113

[81] *Journal of Biomedical Optics*, volume 1, Oct. 1996. 113

[82] S. P. Gopinath, C. S. Robertson, R. G. Grossman, and B. Chance. Near–infrared spectroscopic localization of intracranial hematomas. *Journal of Neurosurgery*, 79:43–47, 1993. 113

[83] C. S. Robertson, S. P. Gopinath, and B. Chance. Use of near–infrared spectroscopy to identify traumatic intracranial hematomas. *Journal of Biomedical Optics*, 2:31–41, 1997. 113, 135

[84] M. Firbank, M. Schweiger, and D. T. Delpy. Investigation of 'light piping' through clear regions of scattering objects. In *Proc. SPIE*, volume 2389, pages 167–173, 1995. 121

[85] M. Firbank, S. R. Arridge, M. Schweiger, and D. T. Delpy. An investigation of light transport through scattering bodies with non–scattering regions. *Phys. Med. Biol.*, 41:767–783, 1996. 121, 123

[86] S. Spaniol. *Gewebeoptische Untersuchungen zur Photodynamischen Therapie von Tumoren.* PhD thesis, Rheinische Friedrich–Wilhelms–Universität Bonn, 1996. 122, 123

[87] M. Kohl. Scattering change at the instant of brain death in rats. Private communication, Nov. 1997. 122

[88] B.-M. Kim, M. Ostermeyer, S. L. Jacques, D. A. Levy, P. Chakrabarti, J. H. Torres, A. C. von Eschenbach, S. Rastegar, and M. Motamedi. In vivo optical property measurement using intraluminal fiber reflectometry: Optical properties of canine and human prostates. In E. Sevick-Muraca and D. Benaron, editors, *OSA TOPS on Biomedical Optical Spectroscopie and Diagnostics*, volume 3, pages 55–58, 1996. 123

[89] B.-M. Kim, M. Ostermeyer, S. L. Jacques, D. A. Levy, P. Chakrabarti, J. H. Torres, A. C. von Eschenbach, S. Rastegar, and M. Motamedi. Transurethral fiber optics for in vivo optical property determination: Human and animal trials. In S. L. Jacques, editor, *Laser-Tissue Interaction VII*, volume SPIE 2681, 1996. 123

[90] D. A. Levy, J. Schwartz, M. Ostermeyer, S. L. Jacques, and A. C. von Eschenbach. Transurethral in vivo optical porperties of the human prostate gland. volume SPIE 2671, 1996. 123

[91] H. Liu, B. Beauvoit, M. Kimura, and B. Chance. Dependence of tissue optical properties on solute–induced changes in refractive index and osmolarity. *Journal of Biomedical Optics*, 1:200–211, 1996.   123

[92] P. Horowitz and W. Hill. *The Art of Electronics*. Cambridge University Press, Cambridge, 2nd edition, 1989.   139

Appendix A

List of Symbols

Symbol	Comment	Page
L	radiance [$\mathrm{W\,cm^{-2}sr^{-1}}$]	10
p	scattering phase function [-]	10
g	scattering anisotropy [-]	11, 14
μ_a	absorption coefficient [$\mathrm{cm^{-1}}$]	8
μ_s	scattering coefficient [$\mathrm{cm^{-1}}$]	8
μ_s'	reduced scattering coeff. $\mu_s' = (1-g)\mu_s$ [$\mathrm{cm^{-1}}$]	15
$\Delta\mu_a$	absorption difference $\Delta\mu_a = \mu_{a1} - \mu_{a0}$ [$\mathrm{cm^{-1}}$]	29
$\Delta\mu_s'$	scattering difference $\Delta\mu_s' = \mu_{s1}' - \mu_{s0}'$ [$\mathrm{cm^{-1}}$]	29
D	diffusion coefficient $D = 1/(3\mu_s')$ [$\mathrm{cm^{-1}}$]	16
δ	penetration depth $\delta = 1/\sqrt{3\mu_a\mu_s'}$ [cm]	18
k	wave vektor of photon density wave [$\mathrm{cm^{-1}}$]	17
$\phi,\ \phi_0$	total and background fluence [$\mathrm{W\,cm^{-2}}$]	28
ϕ^{Pert}	perturbation fluence $\phi^{Pert} = \phi - \phi_0$ [$\mathrm{W\,cm^{-2}}$]	30, 61
ϕ^{Ins}	fluence inside sphere [$\mathrm{W\,cm^{-2}}$]	30
G	Green's function of diffusion equation [-]	17
$\hat{G}$	Impulse response $\hat{G} = G/D$ [$\mathrm{cm^{-1}}$]	17
S	source strength [W]	10
S^{Virt}	virtual source strength [W]	60

Symbol	Comment	Page
f, ω	modulation frequency, $\omega = 2\pi f$ [Hz]	15
$\mathbf{J}$	net flux [W cm^{-2}]	14
$J_{\mathbf{n}+}$, $J_{\mathbf{n}-}$	hemispherical fluxes [W cm^{-2}]	20
A	extrapolation factor [-]	21
l_e	extrapolation distance $l_e = 2AD$ [cm]	22
A_l, B_l	expansion coefficient for ϕ^{Pert}, ϕ^{Ins} [W cm^{-2}]	30
f_l	expansion coefficient for ϕ^{Pert} [-]	32
P_l	Legendre polynominals [-]	30
j_l, $h_l^{(1)}$	spherical Bessel, Hankel function [-]	30
a	radius [cm]	31
γ, ζ	contrast ratio [-]	36, 64

Appendix B

The PMI Online Help File

The Photon Migration Imaging software package (PMI) is an extensive collection of software modules for calculations related to the light propagation in scattering media. In the version discussed here (V. 2.1), the package is the result of a collaborative effort between Martin Ostermeyer, then at the University of Texas in Houston, and Maureen O'Leary and David Boas from the University of Pennsylvania in Philadelphia.

A thorough description of the software is beyond the scope of this work. The theory for the SVS module is discussed in chapter 4. Some hints about the implementation of a stand–alone version of the SVS software are given in section 5.7.1, the extension of the SVS to the PMI software is mentioned in 5.7.2. Information about the modules concerned with inverse algorithms and fluorescence can be found in [50, 55]. For the solution of the diffusion equation with the multipole expansion method (EXACT module) see [18, 35] and chapter 3.

To give an impression of the scope of the software this appendix lists a short description of the commands of the different modules. The following sections

were converted directly from the help file of the PMI package (Version 2.1), which is provided as a HTML file for convenient online use.

Format of the Input

The input is line oriented. Everything after a '#' is a comment. A line that is not empty and does not begin with a '#' is a command line. A command line starts with a keyword (leading blanks allowed), the rest of the line (up to an eventual '#') are parameters of the command. This implies that there is only one command per line and that a command can not continue on the next line. Parameters are separated by one or more blanks or tabs.

The input can come either from an input file or from the standard input (keyboard). Normally the input file is specified in the command line when the program is started:

unixprompt> pmi *[inputfilename]*

The program will execute the commands in the input file and return to the Unix prompt. If no input file is specified, the program switches to the interactive mode and waits at its prompt for input. Now command after command can be typed in, or an inputfile can be specified with the Include command:

|PMI> Include *[inputfilename]*

After the commands in the inputfile are executed, the program will return to its prompt and wait for more commands.

PMI Command Summary

- **General:** General commands related to...

  - Include, Prompt, Interactive, System, Bell, Echo, Exit, Quit, Help, SetHTMLhelp, SetPMIdir, Pipes

- **Programming:** Script programming commands...

  - For...Next Loops, Variables, Operations, While Blocks, If Blocks, Functions, SetVariableVormat, Input, PassedArguments, String-Compare

- **Objects:** Commands for defining inhomogeneities

  - ObjectSphere, ObjectCylinder, ObjectBox, ObjectGauss, Apply-Objects, ShowObject

- **Medium:** Commands for defining the properties of different turbid media.

  - Medium, DefineMedium, DefineMediumDynamics, DefineMedium-Flourescence, Background, ShowMedium, FreeMedium, Region-Sphere, RegionCylinder, RegionBox

- **Sources, Detectors, and Data:** Commands for manipulating sets of sources, detectors, and data.

  - For automatic creation of whole SDLists: CreateSDList, SaveS-DList, SaveDataListLoadSDDSet, LoadSDSet, FreeSourceList, AddNoise

  - For manual creation of SDDSets: OpenNewSDDSet, CloseNewS-DDSet, AddSingleSource, AddDetectorLine, AddDetectorPlane, AddDetectorVolume, PrintDetector

- **Images:** Commands for manipulating Images of the optical properties and the fluence.

    - InitImage, SaveImage, SaveDynamicImageLoadImage

- **Boundaries:** Commands for defining the boundaries of a system and the boundary condition.

    - Plane, BoxPlane, BoundaryCondition, Geometry

- **Exact Module:** Commands related to the EXACT module.

    - Exact, Moments

- **Fluorescence Module:** Commands related to the Fluorescence module.

    - FLR_Exact

- **Fit Module:** Commands related to running the FIT module.

    - Fit, SetFitParam, FitToller, SetFitMaxIter

- **Reconstruction Module:** Commands for reconstructing optical properties from measurements of the fluence. Refer to the sample script *image1.pmi* for an example.

    - SetReconParams, NoSirtConstraints, PertData RytovData , BornData, CreateWeights, SaveWeights, RunSirt, SirtConstraints, NoSirtConstraints

- **SVS Module:** Commands related to the **S**uperposition of **V**irtual **S**ources module.

    - SVSonSDDS, ContinueSVSonSDDS, SVSonImage, ContinueSVSonImage

- **MIE Module:** Commands for calculation of l* (random walk step) of Polystyrene Spheres (microspheres) based on **Mie** Theory.

    – Lambda, Mie, MiePoly

Examples can be found in the **sample scripts**. Check also the **PMI homepage**.

General Commands

Following is a list of miscellaneous commands for PMI:

- **Quit** or **Exit** - to exit PMI.

- **Include** *[filename]* - Used to execute the commands in the script given by *[filename]*. Included files may in turn use the **Include** command. If *[filename]* could not be found it is searched for in the **PMI directory**.

- **Interactive** - switches the program to the interactive mode. This makes only sense as a command in an input file. A single point in a line or ˆd (Control d) terminates the interactive mode, the control of the program returns to the superior file from which the **Interactive** command was invoked. If the interactive mode was already the top control level, the program terminates.

- **System** *[unix command]* or: **!** *[unix command]* - launches a unix shell command.

- **Help** *[command]* or **?** *[command]*- gives help for the specified *[command]* or general help if *[command]* is missing. Gives HTML-help if a browser and the help file have been specified properly with the command **SetHTMLhelp**, or plain text help at the PMI-prompt otherwise.

- **SetPMIdir** *[pmi_dir]* - Sets *[pmi_dir]* as the PMI directory. It is convenient to use this command in the initialization file ".pmi_init" that is executed at startup.

- **SetHTMLhelp** *[browser]* *[file]* - Sets the paths for a HTML-browser (i.e. Mosaic or Netscape) which is used to display the HTML-help-file (normally "*[pmi_dir]*/Help/PMI_HELP.html"). It is convenient to use this command in the initialization file ".pmi_init" that is executed at startup.

- **Bell** - Rings a bell.

- **Echo** *[text]* - writes *text* on the screen and to the log file

- **Prompt** - The program waits for a "RETURN". If one types "i" "RETURN", the program executes the **Interactive** command.

- **Pipes** - Pipes are used to control command driven external programs i.e. plot programs like *gnuplot*.

  - **OpenPipe** *[id]* *[prog_name]* - Start
    * *[id]* - Identifies the pipe
    * *[prog_name]* - Name (with path) of the program to be executed
  - **ToPipe** *[id]* *[command]* - Sends *[command]* to pipe *[id]*
  - **ClosePipe** *[id]* - Closes pipe *[id]*
  - **CloseAllPipes** - Closes all pipes. Normally obsolete since all pipes are closed automatically when the program terminates.

Programming Commands

Following is a list of programming commands for use in scripts:

- **For... Next** Loops - For Next loops can be employed in scripts to repeat a block of commands with an incrementing variable. Up to 9 nested loops can be used.

    - **For** *[Variable Name]* = *[min]* **to** *[max]* **step** *[step]* - Start of the For Next loop

        * *[Variable Name]* - Float variable to increment.
        * *[min]* - Start the loop with a value of *[min]*
        * *[max]* - End the loop with the value of *[max]*
        * *[step]* - increment the value by *[step]*

    - **Next** - marks the end of the For Next loop

- **Variables** There are two types of variables: float variables and string variables. The name of a float variable is preceded by an **&** and the name of a string variable is preceded by an **$**. Following are examples of assignments:

    - **&musp = 10** Which gives the float variable **&musp** the value of **10**.

    - **&$filename = foobar** Which gives the string variable **$filename** the value of **foobar**.

    The values of these variables are used in other commands as follows

    - **Medium tumor 0.1 &&musp 0 1.333**

    - **SaveDataList Normal Normal $$filename NoAppend**

    The format used for printing the values of these variables is set using the **SetVariableFormat** command.

- **Operations** Simple mathematical operations are available. They are addition(+), subtraction(-), multiplication(*), and division(/). These operations are used in assignments. For example:

- **&musp = &&musp + 5**

- **&D = 2.25e10 / 3 / &&mutr**

- **$filename = data_ + &&omega + .dat**

NOTE that operations are performed from left to right. For string variables, only the addition operation is available.

- **While Blocks** - While blocks are used as conditional loops in scripts. There can be 9 nested while blocks.

  - **While** *[value1] [condition] [value2]* - Start of the While Block.

    * *[value1]* and *[value2]* are the values being compared.

    * *[condition]* - Six conditions are supported: less than ($<$), less than or equal to ($<=$), greater than ($>$), greater than or equal to ($>=$), equal to ($=$), and not equal to ($!=$).

  - **Wend** - End the While Block.

- **IF Blocks** - If blocks are used to execute a set of commands depending on the result of a condition. There is no limit to the number of nested If Blocks.

  - **If** *[value1] [condition] [value2]* - Start of the If Block.

    * *[value1]* and *[value2]* are the values being compared.

    * *[condition]* - Five conditions are supported: less than ($<$), less than or equal to ($<=$), greater than ($>$), greater than or equal to ($>=$), equal to ($=$), and not equal to ($!=$).

  - **IfEnd** - End the If Block.

- **Functions** - Certain commands are capable of returning values to variables in the script, e.g. FIT. The usage is:

  - **COMMAND** *[parameters] -> &1 &2...*

The -> indicates that the **COMMAND** will return values to the variables *&1 &2...*. The number of values returned depends on the **COMMAND**.

- **SetVariableFormat** *[name] [format]* - Used to set the format for printing string and float variables.

  - *[name]* is the name of a string or float variable. Remember to precede the string (float) variable with a $ (&).

  - *[format]* is the format string. Standard-C format strings are used. Therefore, string variables must have a string format and float variables must have a float format. %s and %f are the default formats for string and float variables respectively.

- **Input** *[variable_name] [text string]* - Used to get input from the user and place the result in a variable. For example,

  - Input &musp What is the reduced scattering coef.?

- **PassedArguments** *[var1] [var2]...* - Used if arguments are passed to an included file. There are two ways to pass arguments to an include file: from the unix prompt you follow the format

  - unixprompt> pmi [include_file] [var1] [var2] ...

  or from the PMI interactive mode

  - —PMI> Include [include_file] [var1] [var2] ...

  The arguments are then passed to variables in the include file by using this command in the include file. **PassArguments** can be used anywhere in the include file and can be used any number of times. For example, if you have an include file that expects musp and mua to be passed as arguments, then include the following line at the top of the include file:

– PassedArguments &musp &mua

The float variable &argc is set equal to the number of passed arguments
when a new script is included.

- **StringCompare** *[var1] = [var2]* - This FUNCTION does a string compare. It returns 0 if the strings are equal and 1 if they are not equal.
  The compare is not case sensitive. Example:

  – **StringCompare \$\$FitWhat = MUSP -> &result**

Object Commands

The following commands are used for defining different inhomogeneities:

- **ObjectSphere** *[name] [medium] [x] [y] [z] [r]* - Used to define a spherical inhomogeneity.

  – *[name]* - is the name of the sphere. The name may be exploited in future versions of PMI.

  – *[medium]* - is the name of the medium which fills the sphere, e.g. tumor or hematoma. The medium must be defined prior to execution of **ObjectSphere** using the command **Medium**

  – *[x] [y] [z]* - define the position of the center of the sphere.

  – *[r]* - is the radius of the sphere.

- **ObjectCylinder** *[name] [medium] [x1] [y1] [z1] [x2] [y2] [z2] [r]* - Used to define a cylindrical inhomogeneity.

  – *[name]* - is the name of the cylinder. The name may be exploited in future versions of PMI.

- *[medium]* - is the name of the medium, see in **ObjectSphere**.

- *[x1] [y1] [z1]* - defines the position of the center of the bottom of the cylinder.

- *[x2] [y2] [z2]* - defines the position of the center of the top of the cylinder. Note that EXACT can only work with infinite cylinders and thus only uses these positions to define the axis of the cylinder. Presently, EXACT can only work with cylinders which have an axis parallel to the z-axis. SVS, however, can use cylinders of finite length and arbitrary orientation.

- *[r]* - is the radius of the cylinder.

- **ObjectBox** *[name] [medium] [xlo] [ylo] [zlo] [xhi] [yhi] [zhi]* - Used to define a rectangular inhomogeneity with sides parallel to the coordinate axes.

  - *[name]* - is the name of the box. The name may be exploited in future versions of PMI.

  - *[medium]* - is the name of the medium, see in **ObjectSphere**.

  - *[xlo] [ylo] [zlo]* - define the lower x, y, z values.

  - *[xhi] [yhi] [zhi]* - define the upper x, y, z values.

  Note that no EXACT solution is available for boxes, but SVS works with it.

Medium Commands

The following commands are used to define the properties of different media:

- **Medium** *[name] [mua] [mus] [g] [n] [LOTS OF STUFF]* - Used to define the properties of a new medium.

– *[name]* - is the name of the medium which is used by other parts of
   the program to reference a particular medium.

– *[mua]* - is the absorption coefficient of the medium.

– *[mus]* - is the scattering coefficient of the medium.

– *[g]* - is the average cosine of the scattering angle.

– *[n]* - is the index of refraction.

- **DefineMedium** *[name] [mua] [mus] [g] [n]* - Used to define or change
  the properties of a medium.

   – *[name]* - is the name of the medium which is used by other parts of
      the program to reference a particular medium.

   – *[mua]* - is the absorption coefficient of the medium.

   – *[mus]* - is the scattering coefficient of the medium.

   – *[g]* - is the average cosine of the scattering angle.

   – *[n]* - is the index of refraction.

- **DefineMediumDynamics** *[name] [Brownian] [Shear]* - Used to define
  or change the DYNAMICAL properties of a medium.

   – *[name]* - is the name of the medium which is used by other parts of
      the program to reference a particular medium.

   – *[Brownian]* - is the Brownian diffusion coefficient of the scattering
      particles.

   – *[Shear]* - is the rate of shear for the scattering particles.

- **DefineMediumFluorescence** *[name] [tau] [mua_f] [musp_f] [fmua]*
  [fmusp] [fmua_f] [fmusp_f] - Used to define or change the FLUORES-
  CENT properties of a medium.

   – *[name]* - is the name of the medium which is used by other parts of
      the program to reference a particular medium.

- – *[tau]* - is the fluorescence lifetime.

- – *[mua_f]* - is the absorption coefficient of the chromophore at the fluorescence wavelength.

- – *[musp_f]* - is the reduced scattering coefficient of the chromophore at the fluorescence wavelength.

- – *[fmua]* - is the absorption coefficient of the fluorophore at the excitation wavelength.

- – *[fmusp]* - is the reduced scattering coefficient of the fluorophore at the excitation wavelength.

- – *[fmua_f]* - is the absorption coefficient of the fluorophore at the fluorescence wavelength.

- – *[fmusp_f]* - is the reduced scattering coefficient of the fluorophore at the fluorescence wavelength.

- **Background** *[medium_name]* - Used to set the background medium.

  - – *[medium_name]* - is the name of the medium defined using the **Medium** command.

Sources and Detectors

Several sources, each with its own amplitude and phase, and several detectors, also with amplitude and phase, are organized in a Source-Detector-Data-Set (SDDS). The modulation frequency and the correlation time are the same for a SDDSet and all sources are 'on' at the same time. The forward algorithms (Exact, SVS, PertData) can operate on one SDDSet at a time. If one wants to calculate situations with several modulation frequencies or correlation times or with changed source or detector positions, one has to create several SDDSets. All the SDDSets are stored in a list, the SDList.

Because inverse algorithms work with the SDList there is a group of commands for creating, saving, and loading a whole SDList as well as saving and loading the corresponding data in one step. For pure forward calculations it can be more convenient to set a SDDSet 'by hand', which is done by the second group of commands.

Commands for SDLists

- **CreateSDList** *[format] [parameters...]* - Used to create a source-detector set.

  - *[format]*=GRID This format is used to create a set of detectors for a spatially fixed source group. The modulation frequency and correlation time of the source can be scanned as well as the X, Y, and Z coordinates of the detector.

    * *[parameters...] =*
    * *[number of Sources in Source Group]*
    * *[Xs] [Ys] [Zs] [Amp] [Ph] ...* Position and initial amplitude and phase of each source in the source group.
    * *[Omega Min] [Omega Max] [Omega Step]* Frequency given in MHz
    * *[Tau Min] [Tau Max] [Tau Step]* Correlation time in seconds
    * *[X Min] [X Max] [X Step]* X coordinates of the detector
    * *[Y Min] [Y Max] [Y Step]* Y coordinates of the detector
    * *[Z Min] [Z Max] [Z Step]* Z coordinates of the detector

  - *[format]*=TANDEM This format is used to scan a source group and detector in tandem. A grid is defined and the position of the source group and detector are given relative to the grid points.

    * *[parameters...] =*

∗ *[number of Sources in Source Group]*

∗ *[Xs] [Ys] [Zs] [Amp] [Ph] ...* Position and initial amplitude and phase of each source in the source group. The position is given relative to the grid points defined below.

∗ *[Omega Min] [Omega Max] [Omega Step]* Frequency given in Mhz

∗ *[X Min] [X Max] [X Step]* X coordinates of the grid points

∗ *[Y Min] [Y Max] [Y Step]* Y coordinates of the grid points

∗ *[Z Min] [Z Max] [Z Step]* Z coordinates of the grid points

∗ *[X det] [Y det] [Z det]* Position of the detector relative to the grid points

– *[format]*=CYLINDER2 This format is used to scan a source and scan a detector around a cylinder. A grid is defined and the position of the source group is given relative to the grid points. Next a detector grid is defined relative to the source grid points. Thus, for each source there are a grid of detectors.

∗ *[parameters...]* =

∗ *[Zmin] [Zmax] [Zstep]* The z positions for the source grid.

∗ *[Phis_Min] [Phis_Max] [Phis_Step]* The phi positions for the source grid.

∗ *[rho]* This is the radius of the cylindrical scan.

∗ *[omega]* Modulation frequency

∗ *[tau]* Correlation time

∗ *[Num_Srcs]* number of sources in the source group

∗ *[Zsrc] [Phi_src] [Amp] [Ph] ...* Position and initial amplitude and phase of each source in the source group. The position is given relative to the source grid points.

∗ *[Z_det] [Phi_Min_Det] [Phi_Max_Det] [Phi_Step_Det]* Definition of the detector grid relative to the source grid.

- **SaveSDList** *[filename]* - Used to save a list of source-detector sets

  - *[filename]* - is the filename for the output file. Note that .sd is appended to the filename

- **SaveDataList** *[FormatType] [DataType] [filename] [append]* - Used to save a list of data.

  - *[FormatType]* One of the following:

    * **Normal** - creates a data file with the standard PMI code format. *[DataType]* can have the following values:

      · **Normal** - saves the incident and total amplitude and phase.

      · **Total/Incident** - saves the ratio of the total to the incident.

    * **WWWstandard** - uses the format designed for sharing data over the WWW. *[DataType]* can have the following values:

      · **Normal** - saves the incident and total amplitude and phase.

  - *[DataType]* - determines what type of data is saved, e.g. save the total amplitude and phase or relative to the incident amplitude and phase. The value of this parameter depends on the chosen *[FormatType]*.

  - *[filename]* - is the filename for the output file. Note that .dat is appended to the filename

  - *[append]* - if this equals APPEND then the output is appended to *[filename]*

- **AddNoise** *[shot noise] [position uncertainty]* - Used to add noise to a set of data.

  - *[shot noise]* - When this is not equal to zero then shot noise is added to the data, The noise is determined by taking the square-root of the fluence multiplied by *[shot noise]*. *[shot noise]* is thus the product

of the source amplitude in units of photons per second, the signal integration time in units of seconds, the detector area in units of cmˆ2, and the quantum efficiency of the detector.

– *[position uncertainty]* - When this is not equal to zero then random noise is added to the data as given by the uncertainty of the position of the source and/or detector relative to each other and/or relative to the sample. *[position uncertainty]* is given in units of cm.

Commands for individual SDDSets

- **OpenNewSDDSet** *[name] [f] [tau]* - Used to create a new SDDSet with the identification *[name]*, the modulation frequency *[f]* in Hz, and the correlation time *[tau]* in ??. After this command sources and detectors can be added until the SDDSet is closed with CloseSDDSet. Try also the sample script svs_demo1.pmi.

- **CloseSDDSet** *[name]* - Used to close the SDDSet with the name *[name]*.

- **AddSingleSource** *[amplitude] [phase] [x] [y] [z]* - Adds a source to the currently open SDDSet.

    – *[amplitude]* in W

    – *[phase]* in degree

    – *[x] [y] [z]* position in cm

- **AddDetectorLine** *[name] [amp] [ph] [x] [y] [z] [e1x] [e1y] [e1z] [lo1] [hi1] [step1]* - Adds a line of detectors with arbitrary orientation to the currently open SDDSet.

    – *[amp] [ph]* amplitude and phase for the whole line.

    – *[x] [y] [z]* position

- – *[e1x] [e1y] [e1z]* vector that specifies the direction of the line, starting from (x,y,z).

- – *[lo1] [hi1] [step1]* specifies distribution of detectors along the line. The zero of the coordinate system is at (x,y,z), the direction is specified by the vector **e1**.

- **AddDetectorPlane** *[name] [amp] [ph] [x] [y] [z] [e1x] [e1y] [e1z] [lo1] [hi1] [step1] [e2x] [e2y] [e2z] [lo2] [hi2] [step2]* - Adds a plane of detectors with arbitrary orientation to the currently open SDDSet.

  - – *[amp] [ph]* amplitude and phase for the whole plane.

  - – *[x] [y] [z]* position of the origin of the new coordinate system.

  - – *[e1x] [e1y] [e1z]* and *[e2x] [e2y] [e2z]* are two vectors **e1** and **e2** that specify the axes of the new coordinate system. The zero of the new coordinate system is at (x,y,z).

  - – *[lo1] [hi1] [step1]* and *[lo2] [hi2] [step2]* specify the sampling along the axes of the coordinate system. The zero of the coordinate system .

- **AddDetectorVolume** *[name] [amp] [ph] [x] [y] [z] [e1x] [e1y] [e1z] [lo1] [hi1] [step1] [e2x] [e2y] [e2z] [lo2] [hi2] [step2] [e3x] [e3y] [e3z] [lo3] [hi3] [step3]* - Adds a rectangular volume of detectors with arbitrary orientation to the currently open SDDSet. Syntax similar to AddDetectorPlane but with an additional vector **e3**.

- **PrintDetector** *[name] [printwhat] [style] [filename]* - Writes values at detectors.

  - – *[name]* name of a detector that was defined with AddDetectorLine or AddDetectorPlane.

  - – *[printwhat]* ... sorry, no complete description yet, some of many choices are:

    ∗ *AM_P* - amplitude of perturbation fluence

    ∗ *PH_P* - phase of perturbation fluence

    ∗ *AM_F* - amplitude of total fluence

    ∗ *PH_F* - phase of total fluence

    ∗ *AM_B* - amplitude of background fluence

    ∗ *PH_B* - phase of background fluence

    ∗ *PH_DIF* - phase difference between total and background fluence

    ∗ *AM_RAT* - amplitude ratio between total and background fluence

  – *[style]* can be one of the following:

    ∗ *GNU* - file can be plotted directly with gnuplot.

    ∗ *MATH* - file can be plotted directly with Mathematica. In Mathematica type: *<<filename*

  – *[filename]* specifies the file. If no *filename* is given, PrintDetector writes on the screen.

IMAGE Module Commands

The following commands are used for defining the image matrix of a finite system. Each voxel in the image contains the optical properties defined by the user by setting the background medium and the object list.

- **InitImage** *[X min] [X max] [X step] [Y min] [Y max] [Y step] [Z min] [Z max] [Z step]* - sets area to be considered. The area to be reconstructed should be a subset of this large cube. The corners on the cube and the step define the region. When InitImage is called, then optical properties

of any objects which have been defined are inserted (voxel by voxel) into the image.

- **SaveImage** *[filename] [parameters]* - save an image to the file filename. The format of the image file is as follows:

    - [number of x] [number of y] [number of z]

    - [xmin] [xmax] [xstep]

    - [ymin] [ymax] [ystep]

    - [zmin] [zmax] [zstep]

    - a list of the quantities that have been saved

    - the background parameters for each or these quantities

    Next, the columns of data are listed. The valid *parameters* are scattering (MUSP), absorption (MUA), index of refraction (N), browninan diffusion (DB), and shear (SHEAR). If NOHEADER is included in the parameter list, then the first 6 rows are omitted. Note: You cannot use LoadImage to read in a saved image if it is saved with the NOHEADER option.

- **LoadImage** *[filename]* - read a previously saved image into memory. The image CANNOT have been saved with the headers disabled.

BOUNDARY Module Commands

The following commands are used for defining the boundaries of a finite system and the boundary condition to be used in the calculations.

- **Plane** *[a] [b] [c] [d] [n out]* - Used to define a planar boundary.

- *[a] [b] [c] [d]* - The plane is defined by the equation [a] X + [b] Y + [c] Z + [d] = 0. Note that *[a] [b] [c]* is the normal vector to the plane and must point towards the turbid medium.

  - *[n out]* - is the index of refraction on the free-space side of the planar boundary.

- **BoxPlane** *[x1] [y1] [x2] [y2]* - Used to define a BOX geometry. The sides of the box are assumed parallel to the XZ and YZ planes. Opposite corners of the box in the XY plane are given by *[x1] [y1]* and *[x2] [y2]*. Note that *[x1] [y1]* must be less than *[x2] [y2]*. The geometry type is automatically set to BOX.

- **BoundaryCondition** *[parameter]* - Used to define the boundary condition. *[parameter]* is one of the following:

  - *Zero* - uses the zero boundary condition in calculations.

  - *Extrapolated* - uses the extrapolated boundary condition in calculations.

- **Geometry** *[parameter]* - Used to set the geometry type as given by *[parameter]*. *[parameter]* is one of the following:

  - *Infinite* - Calculations are performed for an INFINITE medium.

  - *Planar* - for a medium with PLANAR boundaries.

EXACT Module Commands

These commands will calculate the incident, scattered, and total fluence for the system defined using object, medium, and boundary commands.

- **Exact** - Used to calculate the analytic solution of the diffusion equation for the defined system.

- **Moments** *[file name] [number of moments]* - Used to tell EXACT how many moments to save to file name *[file name]* during the calculation of the scattered wave. If *[number of moments]* is negative then the moments are appended to the file.

FLUORESCENCE Module Commands

These commands will calculate the incident, scattered, and total FLUORES-CENT fluence for the system defined using object, medium, and boundary commands.

- **FLR_Exact** - Used to calculate the analytic solution of the diffusion equation for the defined FLUORESCENT system.

FIT Module Commands

Commands for fitting analytic solutions to experimental or simulated data follow:

- **Fit** *[FitWhat]* - Used to initiate the fit. The source-detector list and data must already be defined as well as all parameters which are known. Refer to the sample script script *fit1.pmi* for an example.

  - *[FitWhat]* - determines whether to fit the amplitude data (AMP), the phase data (PHASE), or both amplitude and phase (BOTH). For Example, **Fit AMP** or **Fit PHASE** or **Fit BOTH**

- **SaveFitResult** *[filename] [DataFlag] [ParamFlag] [AppendFlag]* - Saves the results from the **Fit** command. Typically, the results of the fit are written as the first line of the output file followed by a comparison of the "experimental" and simulated data. Each line of the data corresponds to a single source-detector pair.

  - *[filename]* is the filename. An extension is added to *[filename]* indicating what parameters where fitted.

  - *[DataFlag]* determines what type of data is saved if any. *[DataFlag]* can have the following parameters:

    * **NODATA** - no data is saved.

    * **FREQ** - each line of the data begins with the modulation freq. in MHz of the source for that measurement.

  - *[ParamFlag]* determines if the fitted parameters are saved to the file. If *[ParamFlag]*=**NOPARAM** then no parameters are saved.

  - *[AppendFlag]* determines if the new data starts a new file or is appended to the end of an existing file. If *[AppendFlag]*=**APPEND** then the data is appended to the existing file.

- **SetFitParam** *[parameter] [value] [uncertainty]* - Used to set the initial guess and uncertainty of an unknown parameter. If you wish to make an unknown parameter known then set the *[uncertainty]* equal to zero.

  - *[parameter]* - is one of the following

    * mua_back - absorption coefficient of the background

    * musp_back - scattering coefficient of the background

    * db_back - brownian diffusion coefficient of the background

    * Xo - x position of the object center

    * Yo - y position of the object center

    * Zo - z position of the object center

* a - radius of the object

* mua_obj - absorption coefficient of the object

* musp_obj - scattering coefficient of the object

* db_obj - brownian diffusion coefficient of the object

* tau_f_back - lifetime of fluorophore

* fmua_back - absorption coefficient at excitation wavelength due to fluorophore

* fmusp_back - scattering coefficient at excitation wavelength due to fluorophore

* mua_f_back- absorption coefficient at emission wavelength due to chromophore

* musp_f_back- scattering coefficient at emission wavelength due to chromophore

* fmua_f_back- absorption coefficient at emission wavelength due to fluorophore

* fmusp_f_back- scattering coefficient at emission wavelength due to fluorophore

– *[value]* - is the initial guess for the unknown parameter

– *[uncertainty]* - is an estimate of the uncertainty in the initial guess

- **SetFitTolerance** *[tolerance]* - Used to set the tolerance that must be met when using the FIT module to determine unknown parameters.

- **SetFitMaxIter** *[max]* - Used to set the maximum number of iterations for the AMOEBA fit.

RECONSTRUCTION Module Commands

The reconstruction module inverts the first order solution to the integral equation using either the Born or Rytov Expansion (see Kak and Slaney for descriptions of the Bron and Rytov expansions for diffracting sources). The user must define the quantities to be inverted (i.e. absorption, scattering), the grid to reconstruct on, and the measurement geometry. The only inversion available here is the SIRT algorithm. Refer to the sample script *image1.pmi* for an example.

- **SetReconParams** *[Quantity] [Data Type] [Inverse Method] [Iterations] [Foreward Method]* - sets up the reconstruction.

  - *[Quantity]* - can be **Absorption** or **Scattering** or **Both** or **Brownian** or **Shear**.

  - *[Data Type]* - can be **Amplitude** or **Phase** or **Both**.

  - *[Inverse Method]* - can be **Born** or **Rytov**.

  - *[Iterations]* - the number of SIRT iterations.

  - *[Foreward Method]* - can be **DPDW** to calculate the green's function for a homogeneous medium, **exact** to use the exact calculation for a sphere or cylinder, or **SVS** to use a virtual source calculation to calculate the green's function. Note: exact uses the current object list to determine what homogeneities are present, SVS uses the current image matrix.

- **RytovData** *[shot noise] [positional error]* - divides the total measured wave by the incident and takes the log of the results. This is for the Rytov-type inversion. Shot noise and positional error are added to the measurement before the division.

- **BornData** *[shot noise] [positional error]* - subtracts the incident wave from the total measured wave. This is for the Born-type inversion. Shot noise and positional error are added to the measurement before the subtraction.

- **CreateWeights** - uses either the Born or the Rytov approximation to calculate the weights (also called photon hitting densities, or three point green's functions) to necessary for the inversion routines. WARNING: You must have a source-detector list and an image matrix to create the weights.

- **SaveWeights** *[filename]* - saves the weights to a file. This routine is only recommended for debugging purposes as the weight matrix is generally quite large.

- **PertData** *[filename]* - Multiplies the weights by the image to calculate first order forward data. The data is written to filename.pert.dat. If filename = none, then the data is saved in the internal source-detector-data list for further use. WARNING: the weights and the image matrix have to have been created before PertData is called.

- **RunSirt** *[flag]* - starts the iterative reconstruction routine. See Kak and Slaney for details on SIRT. If the flag is set to be CALC_WEIGHTS, then the weights are created before SIRT is started.

- **SirtConstraints** *[abs. min] [abs. max] [scat min] [scat. max] [lifetime min] [lifetime max] [brownian min] [brownian max] [shearmin] [shear max]* - constrains the SIRT solutions for each voxel to be between some minimum and maximum values. The reconstruction quantities that may be constrained are absorption, scattering, fluorescence lifetime, brownian diffusion, and shear flow.

- **NoSirtConstraints** - removes any/all constraints on reconstruction quantities.

SVS Module Commands

SVS (**S**uperposition of **V**irtual **S**ources) is a numerical method for the forward problem. It solves the integral equation that is equivalent to the diffusion equation in a two step process: (i) the integral equation is solved iteratively only on the voxels of the **Image** which have different optical properties than the background medium and are in the Region-of-interest. Each of these voxels is treated as a **virtual source**, where the strength of the virtual source depends on the difference in the optical properties and on the fluence at each voxel. Because the fluence at a voxel is a sum of the contributions from the real sources and the virtual sources, the problem is iterated. (ii) As the strength of the virtual sources is now known, the fluence at any other points is calculated directly as a superposition of the fluence from the normal sources and the virtual sources. Step (i) is the same for both SVS commands, thus the parameters are the same. The difference (in step (ii)) is where the fluence is calculated.

- **SVSonSDDS** *[mode] [max_order] [precision]* - calculates the fluence at all the detectors of the SDDSet. Try the sample script svs_demo1.pmi.

- **SVSonImage** *[mode] [max_order] [precision]* - calculates the fluence at all the voxels in the region of interest of the active **Image**.

    - *[mode]* - can be **normal** or **optimized**. In **normal**-mode the Born-series is computed straightforward. In **optimized**-mode, oscillation around the correct solution is damped by taking the mean of the fluence from the last two iterations as starting values for the next iteration. Usually the **optimized**-mode converges faster than the **normal**-mode and even for large and/or strong perturbations where the **normal**-mode diverges.

- *[max_order]* - at most *max_order* orders are computed. If the desired *precision* is reached earlier, the iteration stops.

- *[precision]* - the desired *precision* of the iteration. After each iteration the change of the fluence at each voxel is normalized to the background fluence. If this relative change is smaller than *precision* at all voxels, the iteration stops.

Note that both commands require that an image has been created earlier with the command InitImage.

MIE Module Commands

This command will calculate the l* (random walk step), which is in another word the reciprocal of the scattering coefficient mus' for polystyrene spheres based on Mie Theory. It requires to get the wavelength **Lambda** first in the units of **cm**. Then either one of the following commands can be chosen depending upon the situation. A sample script can be found script *mie.pmi*.

- **Mie** *[param]* - Used to calculate the l* (**cm**) given the indices of refraction of the polystyrene spheres and the solvent, the diameter of the polystyrene sphere (**um**), and the volume fraction of polystyrene spheres in the solvent.

- **MiePoly** *[param]* -Used to calculate the l* (**cm**) if the solvent is water, given the temperature (**K**), the diameter of the polystyrene sphere (**um**), and the volume fraction of polystyrene spheres in the solvent.

Incorporating with other PMI commands, you can use the **returned** value (l*) and take advantage of the **For...Next** command. For details, please see Functions for the usage of returned values and For...Next for the loops.

Appendix C

List of Publications

- M. R. Ostermeyer and S. L. Jacques, Perturbation theory for diffuse light transport in complex biological tissues, *J. Opt. Soc. Am. A* 14, pp. 255–261, 1997

- M. Ostermeyer, D. V. Stephens, L. Wang, and S. L. Jacques, Nearfield polarization effects on light propagation in random media, in OSA TOPS on Biomedical Optical Spectroscopie and Diagnostics, editors E. Sevick-Muraca and D. Benaron, 3, pp. 20–25, 1996

- S. L. Jacques, D. Stephens, M. Ostermeyer, and L. Wang, Polarized light transmission through skin using video reflectometry: toward optical tomography of superficial tissue layer, SPIE 2671, 1996

- B.-M. Kim, M. Ostermeyer, S. L. Jacques, D. A. Levy, P. Chakrabarti, J. H. Torres, A. C. von Eschenbach, S. Rastegar, and M. Motamedi, In vivo optical property measurement using intraluminal fiber reflectometry: Optical properties of canine and human prostates, in OSA TOPS on Biomedical Optical Spectroscopie and Diagnostics, editors E. Sevick-Muraca and D. Benaron, 3, pp. 55–58, 1996

- B.-M. Kim, M. Ostermeyer, S. L. Jacques, D. A. Levy, P. Chakrabarti, J. H. Torres, A. C. von Eschenbach, S. Rastegar, and M. Motamedi, Transurethral fiber optics for in vivo optical property determination: Human and animal trials, in Laser-Tissue Interaction VII, editor S. L. Jacques, SPIE 2681, 1996

- D. A. Levy, J. Schwartz, M. Ostermeyer, S. L. Jacques, and A. C. von Eschenbach, Transurethral In Vivo Optical Porperties of the Human Prostate Gland, SPIE 2671, 1996

- M. R. Ostermeyer and S. L. Jacques, Perturbation Theory for Optical Diffusion Theory: a general approach for absorbing and scattering objects in tissue, in Optical Tomography, Photon Migration, and Spectroscopy of Tissue and Model Media: Theory, Human Studies, and Instrumentation, Editors B. Chance and R. R. Alfano, SPIE 2389, pp. 98–102,1995

- M. R. Ostermeyer, A. H. Hielscher, L. Wang, and S. L. Jacques, Accelerated modeling of light transport in heterogenous tissues using superposition of virtual sources, in Theoretical Study, Mathematical, Experimental Model for Photon Transport in Scattering Tissue, Editors S. Avrillier, B. Chance, and G. J. Müller, SPIE 2326, pp. 56–64, 1994

- S. L. Jacques, M. R. Ostermeyer, L. Wang, and A. H. Hielscher, Light dosimetry in PDT using optical fiber delivery, in Optical Methods for Tumor Treatment and detection: Mechanisms and Techniques in Photodynamic Therapy III, SPIE 2133, pp. 155-164, 1994

- S. L. Jacques, M. R. Ostermeyer, L. Wang, and A. H. Hielscher, Effects of Sources, Boundaries, and Heterogeneities on Photon Migration, in OSA proceedings on Advances in Optical Imaging and Photon Migration, editor R. R. Alfano, Optical Society of America, Washington, DC, 21, pp. 83–87, 1994

- F. Mitschke, G. Steinmeyer, and M. Ostermeyer, Subpicosecond 1.9mm Pulses from APM-pumped Color Center Laser, Quantum Electronics and Laser Science Conference (QELS), paper QThH41, 1993

- F. Mitschke, G. Steinmeyer, M. Ostermeyer, C. Fallnich, and H. Welling, Additive Pulse Mode-Locked Nd:YAG Laser: An Experimental Account, Applied Physics B 56, p. 335, 1993

- G. Steinmeyer, U. Morgner, M. Ostermeyer, F. Mitschke, and H. Welling, Subpicosecond pulses near 1.9mm from a synchronously pumped color-center laser, Optics Letters 18, p. 1544, 1993

- G. Steinmeyer, U. Morgner, M. Ostermeyer, and F. Mitschke, Subpicosecond Pulse Generation around 1.9mm by Synchronous Pumping of a KCl:Na+:O2- Color Center Laser, Lietuvos Fizikos Zurnalas (Lithuanian Journal of Physics) 33, p. 260, 1993

Appendix D

Resumé

Name:	Martin Ostermeyer
March 15, 1965	born in Hannover, Germany
	parents: Erich Ostermeyer and Hannaliese Ostermeyer
	married
1971 - 1975	Grundschule Grimsehlweg
1975 - 1984	Gymnasium Großburgwedel
1984 - 1993	University of Hannover
August 1993	Diplom (M.S) in Physics
1994 - 1996	Predoctoral Fellow at the University of Texas
	M. D. Anderson Cancer Center
1996 - 1998	Graduate Student at the University of Hannover
since 4/1998	Research & Development at CeramOptec GmbH, Bonn